

AD-A258 922

①



AFIT/GAE/ENY/92D-03

DTIC
ELECTE
JAN 8 1993
S C D

INVESTIGATION OF FATIGUE BEHAVIOR IN
NOTCHED CROSS-PLY TITANIUM METAL MATRIX
COMPOSITE AT ELEVATED TEMPERATURE

THESIS

Robert P. Baker, Captain, USAF

AFIT/GAE/ENY/92D-03

Approved for public release; distribution unlimited

93-00025



93 1 04 044

AFIT/GAE/ENY/92D-03

Available For	
Microfilm	<input checked="" type="checkbox"/>
microfiche	<input type="checkbox"/>
Unlimited	<input type="checkbox"/>
Distribution	
Available For	
Dist	Special
A-1	

INVESTIGATION OF FATIGUE BEHAVIOR IN
NOTCHED CROSS-PLY TITANIUM METAL MATRIX
COMPOSITE AT ELEVATED TEMPERATURE

THESIS

DTIC QUALITY INSPECTED 8

Presented to the Faculty of the School of Engineering
of the Air Force Institute of Technology
Air University
In Partial Fulfillment for the
Requirements for the Degree of
Master of Science in Aeronautical Engineering

Robert P. Baker, B.S.

Captain, USAF

December 1992

Approved for public release; distribution unlimited

Preface

As the science of flight grows and matures, we seek to go higher and faster than ever before. To accomplish this goal, new materials are developed, tested, and eventually employed. Before any person risks life and limb piloting a vehicle fabricated of advanced materials, we must characterize all aspects of the material's behavior.

The material examined in this study is a metal matrix composite called SCS-6/Ti-15-3. The purpose of this investigation is twofold. First, to establish the number of cycles at which cracks initiate and the location of the first crack(s) from a hole when subjected to fatigue loading. Second, to characterize the nature of the crack growth and progression.

As with all major endeavors in life, I owe a debt of gratitude to many outstanding people who have helped me along this educational odyssey. Without the valuable help and vast knowledge of Mr Mark Derriso and Capt Brian Sanders, this work would not have started or finished. I also wish to thank the people at the AFIT model shop as well as the Materials Lab for their patience, expertise, and guidance. Additionally, I want to thank AFOSR for funding my research. I especially would like to thank my advisor Dr Shankar Mall, whose guidance and keen insight have kept me on track (despite my numerous attempts to get side tracked). Above all others, however, I

am most grateful for the love, devotion, and unhesitating support of my best friend -- my wife, Barb. Thank you for being both parents to Andy and Holly during my absence.

Table of Contents

Preface	i
List of Figures	vi
List of Tables	x
List of Symbols	xi
Abstract	1
I. Introduction	3
II. Previous Works	8
Introduction	8
Room Temperature Testing	11
High Temperature Testing	14
III. Experimental Set-up and Procedures	17
Material	17
Material Preparation	18
Specimen Preparation	18
Test Apparatus	22
Acetate Replicas	23

Test Procedures	26
Post-Failure Analysis	29
IV. Results and Discussion	34
Terminology	35
Cyclic Life	37
Tensile Test	44
Strain Curves	44
Modulus Curves	49
Crack Initiation and Growth	52
Quantitative Analysis	85
Crack Initiation and Growth Synopsis	98
V. Conclusions and Recommendations	100
Appendix 1	103
Appendix 2	118
Appendix 3	133
Appendix 4	140
Appendix 5	143

Bibliography 151

Vita 155

List of Figures

Figure 1: Load-Time Relationship	6
Figure 2: Typical Fiber Cross-section	19
Figure 3: Specimen cutting details	21
Figure 4: Test Apparatus	24
Figure 5: Thermocouple welding diagram	25
Figure 6: Strain Measurement Equipment	31
Figure 7: Specimen sectioning diagram	32
Figure 8: Cross-sectional area definitions	36
Figure 9: Crack Initiation S-N Curve	39
Figure 10: Failure S-N Curve	40
Figure 11: Initiation and Failure S-N Curves	41
Figure 12: Comparison of Cyclic Failure	42
Figure 13: Monotonic Tension Test	45
Figure 14: Strain vs. Cycles to Failure	46
Figure 15: Effect of Extensometer Placement	48
Figure 16: High Stress Stiffness vs Cycles to Failure .	50
Figure 17: Low Stress Stiffness vs. Cycles to Failure .	51
Figure 18: Strain Range	53
Figure 19: Debonding of 90° fibers (300 MPa Edge Replica)	54
Figure 20: Crack Initiation Sites	56
Figure 21: Crack Bifurcation on High Stress Specimen Face (100x)	57

Figure 22: Typical Fracture Surface Coloration	60
Figure 23: Specimens 1 through 4 (left to right) . . .	61
Figure 24: Monotonically Loaded Specimen Fracture Surface	62
Figure 25: Fatigue Loaded Specimen Fracture Surface . .	63
Figure 26: Fracture Surface of a Fatigued Specimen (at the hole)	64
Figure 27: Fracture Surface of a Fatigued Specimen (at the edge)	65
Figure 28: Ductile to Brittle Transition	66
Figure 29: Minor Cracks Progressing into the Specimen .	68
Figure 30: Fatigue Crack Shape Prior to Failure	69
Figure 31: 90° Fiber Debonding Below the Fracture Surface, Inside the Specimen	70
Figure 32: Transverse Crack Propagation Past a 0° Fiber	71
Figure 33: Transverse Cracking within the Specimen . .	72
Figure 34: Transgranular Cleavage of Initial Crack . .	73
Figure 35: Longitudinal and Transverse Cracking of the Outer Carbon Coating of 0° Fibers.	74
Figure 36: Bright Field Illumination of Fiber Bridging	75
Figure 37: Fiber Bridging Minor Matrix Crack	76
Figure 38: Fiber Bridging of Major and Minor Cracks . .	77
Figure 39: Magnified View of Fiber Bridging of Major Crack (top left crack)	78

Figure 40: Magnified View of Fiber Bridging of Minor Crack (bottom left crack)	79
Figure 41: Matrix Yielding Between 0° Fibers Near the Hole	80
Figure 42: Low Stress Level Crack Length vs. Cycles .	81
Figure 43: High Stress Level Crack Length vs. Cycles .	82
Figure 44: Strain, Modulus, and Crack Growth Comparison	84
Figure 45: Total Crack Length Comparison	86
Figure 46: Critical Crack Length vs. Stress Level . . .	88
Figure 47: Stress-Strain Hysteresis Loop	90
Figure 48: Crack Initiation Prediction	96
Figure 49: Specimen 2 (240 MPa) Strain vs. Cycles . . .	104
Figure 50: Specimen 2 (240 MPa) Strain vs. Log Cycles	105
Figure 51: Specimen 3 (400 MPa) Strain vs. Cycles . . .	106
Figure 52: Specimen 3 (400 MPa) Strain vs. Log Cycles	107
Figure 53: Specimen 4 (300 MPa) Strain vs. Cycles . . .	108
Figure 54: Specimen 4 (300 MPa) Strain vs. Log Cycles .	109
Figure 55: Specimen 5 (170 MPa) Strain vs. Cycles . . .	110
Figure 56: Specimen 5 (170 MPa) Strain vs. Log Cycles .	111
Figure 57: Specimen 6 (225 MPa) Strain vs. Cycles . . .	112
Figure 58: Specimen 6 (225 MPa) Strain vs. Log Cycles .	113
Figure 59: Specimen 7 (425 MPa) Strain vs. Cycles . . .	114
Figure 60: Specimen 7 (425 MPa) Strain vs. Log Cycles .	115
Figure 61: Specimen 8 (300 MPa) Strain vs. Cycles . . .	116

Figure 62: Specimen 8 (300 MPa) Strain vs. Log Cycles .	117
Figure 63: Specimen 2 (240 MPa) Modulus vs. Cycles . .	119
Figure 64: Specimen 2 (240 MPa) Modulus vs. Log Cycles	120
Figure 65: Specimen 3 (400 MPa) Modulus vs. Cycles . .	121
Figure 66: Specimen 3 (400 MPa) Modulus vs. Log Cycles	122
Figure 67: Specimen 4 (300 MPa) Modulus vs. Cycles . .	123
Figure 68: Specimen 4 (300 MPa) Modulus vs. Log Cycles	124
Figure 69: Specimen 5 (170 MPa) Modulus vs. Cycles . .	125
Figure 70: Specimen 5 (170 MPa) Modulus vs. Log Cycles	126
Figure 71: Specimen 6 (225 MPa) Modulus vs. Cycles . .	127
Figure 72: Specimen 6 (225 MPa) Modulus vs. Log Cycles	128
Figure 73: Specimen 7 (425 MPa) Modulus vs. Cycles . .	129
Figure 74: Specimen 7 (425 MPa) Modulus vs. Log Cycles	130
Figure 75: Specimen 8 (300 MPa) Modulus vs. Cycles . .	131
Figure 76: Specimen 8 (300 MPa) Modulus vs. Log Cycles	132
Figure 77: Specimen 2 (240 MPa) Stress vs. Strain . .	144
Figure 78: Specimen 3 (400 MPa) Stress vs. Strain . .	145
Figure 79: Specimen 4 (300 MPa) Stress vs. Strain . . .	146
Figure 80: Specimen 5 (170 MPa) Stress vs. Strain . .	147
Figure 81: Specimen 6 (225 MPa) Stress vs. Strain . . .	148
Figure 82: Specimen 7 (425 MPa) Stress vs. Strain . .	149
Figure 83: Specimen 8 (300 MPa) Stress vs. Strain . . .	150

List of Tables

Table I: Matrix Composition	17
Table II: Test Matrix and Post-Processing	28
Table III: Test Matrix	30
Table IV: Test Results	38
Table V: Ti-15-3 Material Properties (23:14-15)	93
Table VI: SCS-6 Fiber Material Properties (23:14-15)	93
Table VII: Laminate Properties from METCAN at 427°C	95
Table VIII: Stress Level and Cyclic Life	95

List of Symbols

Al	Aluminum
C	Carbon
Cr	Chromium
d	Hole Diameter
E_L	Longitudinal Young's Modulus of the Composite
E_m	Matrix Material Young's Modulus
E_T	Transverse Young's Modulus of the Composite
F	Fluorine
G_{LT}	Shear Modulus of the Composite
H	Hydrogen
K_t	Stress Concentration Factor for a Finite Plate
K_t°	Stress Concentration Factor for an Infinite Plate
L_c	Critical Crack Length
Mo	Molybdenum
N	Nitrogen, Number of Cycles
R	Stress Ratio
S	Stress
Si	Silicon
S_{max}	Maximum Stress
S_{min}	Minimum Stress
Sn	Tin
Ti	Titanium
Va	Vanadium

V_f	Fiber Volume Fraction
w	Specimen Width
a	Finite Width Correction Factor
β	Percentage of Fiber's Bridging a Crack
$\Delta\epsilon$	Change in Strain
$\Delta\sigma$	Change in Stress
ϵ	Strain
ϵ_{max}	Maximum Strain
ϵ_{min}	Minimum Strain
ν_{lf}	Poisson's Ratio
σ	Stress
σ_r	Residual Stress of the Matrix Material
σ_{test}	Stress Level of a Given Test
σ_{ult}	Ultimate Strength of the Material

Abstract

Requirements for higher and faster travel are pushing conventional aircraft materials to the limit. To extend the operating envelope of modern aircraft, new materials must be examined for use in engines and airframe structures. One such promising material is SCS-6/Ti-15-3 a metastable β phase titanium alloy. It possesses good strength characteristics at high temperatures.

The objective of this research was to investigate the initiation and progression of cracks which develop in notched $[0/90]_{28}$ SCS-6/Ti-15-3 at elevated temperature. Testing consisted of a monotonic tensile test at 427°C followed by fatigue testing performed under load control with a stress ratio of 0.1 at a frequency of 10 Hz. A crack was defined to have initiated when it had attained a length greater than or equal to 0.124 mm. Crack initiation and progression was monitored by strain and modulus observations and visual inspection via telemicroscope. The cracks were recorded with edge and face replicas. Metallographic and fractographic analysis was performed after specimen failure.

Fatigue cracks initiated in the matrix at four locations on the front and back faces of each specimen. Two of these cracks became through-cracks and eventually developed into major cracks which caused the fracture. The applied stress

(S) and fatigue lives (N) curves for both initiation and fatigue life were established. Also, crack growth curves as the function of fatigue cycles were established. A detailed metallographic analysis was performed to understand the damage mechanisms and its implication on the observed notched fatigue behavior.

INVESTIGATION OF FATIGUE BEHAVIOR IN
NOTCHED CROSS-PLY TITANIUM METAL MATRIX
COMPOSITE AT ELEVATED TEMPERATURE

I. Introduction

In mankind's quest for greater speeds and higher altitudes, aircraft engines and structures must operate in a most hostile environment. The extreme temperatures and stresses involved demand that special materials be used in manufacturing engine components and other high temperature structural members. With the advent of the space shuttle, the National Aerospace Plane (NASP), the B-2 bomber, the Advanced Tactical Fighter, and the F-117 stealth fighter, composite materials have become an integral part of modern aircraft design.

Composite materials provide the required strength at a fraction of the weight of traditional aircraft materials. Three basic categories of composite materials are: ceramic matrix, polymeric matrix, and metal matrix. Ceramic matrix composites are usually ceramic fibers embedded in a ceramic matrix. For example: Silicon Carbide fibers in a Silicon-Nitrogen matrix ($\text{SiC}/\text{Si}_3\text{N}_4$) or Carbon fibers in a Carbon matrix. Ceramic matrix composites are excellent for high temperature use because of their thermal characteristics. The

major draw back, however, is its poor strength characteristics. On the other hand, polymeric composites have good strength characteristics, but poor thermal properties. Polymeric composites are generally composed of ceramic fibers embedded in a polymer matrix. For example: Graphite/Epoxy composites or Kevlar 49/Epoxy. Metal matrix composites (MMCs) blend the best of both. They have good high temperature characteristics as well as excellent mechanical properties.

Before aircraft manufacturers incorporate a new material in their designs, a complete assessment of the material behavior must be made. This means that mechanical properties and failure modes at a variety of temperatures and load conditions must be understood.

The material investigated in this report is SCS-6/Ti 15-3 which is the commercial designation for Silicon Carbide fibers embedded in a Titanium alloy matrix. The alloy designated as Ti-15-3 is 76% (by weight) Titanium, 15% Vanadium, 3% Tin, 3% Chromium, and 3% Aluminum. This study employed the laminate of this metal matrix composite with a cross-ply lay-up, $[0/90]_{25}$. This material's properties and failure characteristics at room temperature are well documented. Bakuckas et al (3:1-29) employed an effective strain parameter to predict crack initiation around a hole for given stress levels at room temperature in cross-ply SCS-6/Ti-15-3.

Hillberry and Johnson investigated the development of cracks in cross-ply notched SCS-6/Ti-15-3 in which they used a shear-lag cylinder model to predict crack spacing and debond length. Naik and Johnson investigated fatigue crack initiation and growth in notched SCS-6/Ti-15-3 for a variety of ply orientations. They found that both matrix cracking and fiber/matrix debonding contribute greatly in reducing the stress concentration at holes or edge notches.

Researchers have also investigated the material characteristics at elevated temperature. Mirdamadi, Johnson, Bahei-El-Din, and Castelli investigated the thermo-mechanical fatigue (TMF) characteristics of unnotched unidirectional SCS-6/Ti-15-3 and found that the zero degree fiber stress is a controlling factor in fatigue life of the material. Pollock and Johnson examined the behavior of the unnotched material at 650°C. Mall and Portner investigated the fatigue characteristics of unnotched SCS-6/Ti-15-3 at 427°C. Mall and Schubbe investigated TMF behavior of unnotched cross-ply material. One key aspect to be investigated, however, is the failure mechanisms associated with stress concentrations at elevated temperature.

The research conducted in this thesis will deal with the most common stress concentration: a center hole. In aerospace applications, holes may take the form of fastener attachment points, cutouts for cable routing, battle damage, and windows.

Damage tolerance engineers are concerned with holes because holes tend to be damage initiation sites. This research will help designers establish safe operating limits for aircraft constructed with SCS-6/Ti 15-3.

This investigation, therefore, studied crack initiation and progression of damage mechanisms in a $[0/90]_{28}$ laminate of SCS-6/Ti-15-3 with a 3.175 mm diameter hole subjected to fatigue loading at 427° C. Eight specimens were used in the study. One specimen was subjected to static tensile testing at 427° C and the remaining specimens were subjected to

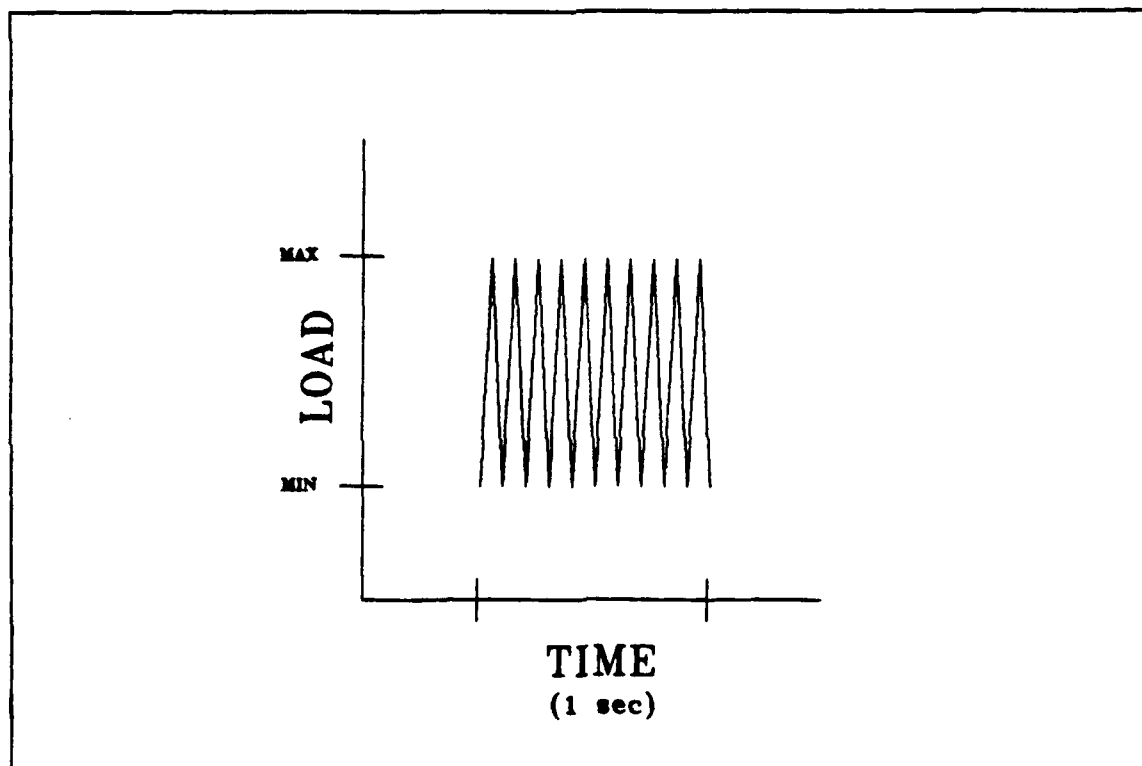


Figure 1: Load-Time Relationship

fatigue loading at different load levels. All of the fatigued specimens were tested at 10 Hz with a load ratio (R) of 0.1 under load control. The load-time relationship is displayed in figure 1.

During testing, damage progression was monitored in two ways. First, a telemicroscope was used to visually observe of the crack. Secondly, edge and face replicas were taken to provide a physical record of the damage for later examination. Additional information about damage progression was obtained by monitoring changes in both modulus and strain.

Following testing, fractographic analysis of the fracture surface provided insight to the nature and character of the failure. Examination of the face replicas provided information on crack development and growth. When coupled with strain and modulus change information, the complete picture of the failure becomes clear. The applied stress (S) and fatigue life (N) curves for both initiation and fatigue lives were established. Also, crack growth curves as the function of fatigue cycles were established. A detailed metallographic analysis was performed to understand the damage mechanisms and its implication on the observed notched fatigue behavior.

II. Previous Works

Introduction

When a material fails at loads below the material's ultimate strength the cause is usually fatigue. Fatigue failures result from repeated loading and unloading of a given structure. At higher loads, a given material will have a much shorter life. At lower load levels, the life is significantly longer. Fatigue cracking has three phases: crack initiation, crack growth, and component failure (5:4.80). The first phase, crack initiation, takes place at regions of local stress concentrations. In an unnotched specimen, this could be any kind of scratch on the surface or some internal material flaw caused by manufacturing. On notched specimens, the stress concentration region is around holes or edge notches. A specimen cycled at high stress tends to spend the majority of its life in initiating a crack whereas those cycled under low loads tend to spend a smaller percentage in the initiation phase.

Crack growth is also dependent upon loading levels. At high loads, cracks propagate much faster than those at low load levels. Initially, for monolithic materials, the cracks start to grow along crystallographic planes and consequently may change direction when the crack crosses grain boundaries

(6:552). This is termed brittle cleavage fracture. Once a crack is detected in a monolithic material, failure soon follows. For composite materials, however, the presence of the fibers will have an effect on both crack initiation and growth. Fibers oriented in the direction of loading will tend to slow the crack growth because the fibers are taking a higher portion of the load. Thus, for a brittle fiber in a ductile matrix there are two possible ways for the crack to progress. If the interface region is strong, then the fiber will fracture before the crack arrives. If it is a weak interface region, the crack will arrive at the fiber, crack the interface along a short length of the fiber, then proceed to the next fiber (1:293). Fibers oriented parallel to the crack will do little to impede crack propagation.

The final phase of fatigue life, component failure, occurs with little if any warning. Most monolithic materials fail soon after fatigue cracks initiate. Fiber reinforced composites, however, do not fail immediately. Johnson has found that the load carrying capability of the 0° fibers is the dominant factor in the Silicon Carbide/Titanium family of composite materials (15:209). This means that the fatigue crack length prior to component failure will be much longer for a composite than for a monolithic and thus leads to a longer life.

The key advantage of composites is that the specific strength and modulus are much better than those of monolithics (1:10). For example, the fourth stage of the Allison Gas Turbine's XTC 16/1 A IHPTET (Integrated High Performance Turbine Engine Technology) is one fifth the weight of a similar component made of a nickel superalloy (25:66). Composites are ideally suited for the aviation industry.

Early research into Metal Matrix Composites (MMCs) dealt with fiber reinforced aluminum composites (25:67) which were seen as an inexpensive way to attain higher strength materials which yields a longer life. During the quest to find materials for the NASP's skin, a fiber reinforced alpha 2 Titanium Aluminide was examined because of its ability to withstand temperatures in excess of 900°C, but was found to be unable to withstand repeated thermal cycling (25:66). This led Textron (a NASP subcontractor) to investigate other Titanium Matrix Composites (TMCs) such as SCS-6/Ti-15-3. One drawback in using the Ti-15-3 matrix system is that its oxidation resistance is lower than some other more preferable materials. SCS-6/Ti-15-3 may not be ideally suited to the NASPs requirements, but it is still ideally suited for other applications such as engine components or structures around the engines.

Room Temperature Testing

Hillberry and Johnson investigated crack initiation of notched SCS-6/Ti-15-3 at room temperature (11:1-14). Their approach was to predict crack initiation using a modified strain parameter. The specimens tested were [0/90]₂₃ with a fiber volume fraction of 0.325 and were in the as fabricated (ASF) condition. Some of the specimens had center holes (CH) while the others had double edge notches (DEN). These fatigue tests were run under load control with a 0.1 stress ratio at a frequency of 10 Hz. In addition to the composite tests, they conducted strain controlled tests on the matrix material. The matrix fatigue tests were run with a strain ratio of 0.1 at a frequency of 10 Hz. Each specimen was observed with a telemicroscope and preserved by face and edge replicas. Crack initiation was defined as development of at least one crack 0.2-0.4 mm long.

Hillberry and Johnson adapted an effective strain parameter first developed by Smith, Watson, and Topper (34:767-778) to account for residual stresses during composite cool down (11:5-7) and local stress concentrations at the notch tip. Because the fiber's modulus is much larger than that of the matrix, the assumption is made that the matrix is essentially under strain control. This means that the strain is proportional to the applied stress. Consequently, the strain concentration factor is approximately the same as the

stress concentration factor. The predictions were in close agreement with the experimental results.

Newaz and Majumdar (27:1-22) investigated crack initiation in unidirectional SCS-6/Ti-15-3 with center holes. Their purpose was to characterize the nature of crack initiation and growth from center holes. Additionally, they wanted to determine crack initiation sites and whether the cracks were through-cracks. The experiment consisted of fatigue loading specimens at a stress ratio of 0.1 and a frequency of 2 Hz under load control. Some of the specimens were subjected to monotonic tensile testing. The fatigue tests were stopped prior to specimen failure at which time the specimen was sectioned and polished for metallographic examination. They found that a circumferential stress expression by Greszczuk (9:366-367) could be used to express the stress at any point around the circumference of the hole. They used the Hencky-Von Mises distortion energy theory (9:373) to predict the point around the hole where yielding would occur.

During the course of their research, they found that the fatigue loaded specimens developed four major cracks around the periphery of the hole. The cracks are through-cracks and are bridged by the SCS-6 fibers. These major cracks form between 65° and 72° from the loading axis. The Hencky-Von Mises yield criterion predicts accurately the location of the

cracking. Newaz and Majumdar believe that initiation is controlled by the local inelastic strain of the matrix (27:11). In contrast, the monotonically loaded specimens developed cracks 90° from the loading axis. It is interesting to note that yielding occurs at 65° - 72° from the loading axis, but does not cause failure. They determined that the monotonic specimens failed due to fiber fracture whereas in fatigue loading, failure is caused by matrix failure.

Naik and Johnson (24:1-35) performed an investigation similar to Hillberry and Johnson's. In this study, Naik and Johnson attempted to characterize room temperature damage initiation in notched SCS-6/Ti-15-3 $[0]_8$, $[0_2/\pm 45]_2$, $[0/\pm 45/90]_2$, and $[0/90]_{2g}$ laminates. They had some specimens with center holes (CH) and others with double edge notches (DEN). The testing consisted of load controlled constant amplitude fatigue at a stress ratio of 0.1 with a 10 Hz frequency. Two types of loading were used in this study. First, some specimens were subjected to constant amplitude loading for the entire specimen life. Second, other specimens were subjected to an incremental loading approach. In this method, the specimen is fatigued for 50,000 cycles at one load level then 50,000 more cycles at the next higher load level.

Their analysis incorporated a local strain criterion to predict fatigue crack initiation. This approach was successful. One conclusion which they reached was that

debonding and matrix cracking served to reduce the effect of the stress concentration. They observed only matrix cracking and no fiber cracks. Their work also indicated that heat treated and as fabricated materials behave in a similar manner.

High Temperature Testing

Mall and Portner (21:1-38) investigated the fatigue characteristics of unnotched cross-ply SCS-6/Ti-15-3 at 427°C. This study was to examine the initiation and progression of damage in this material at high temperature. The specimens used were $[0/90]_{2s}$ with a fiber volume fraction of 0.38. The fatigue tests were run at a load ratio of 0.1 under load control. Testing was performed at 2 Hz and 0.02 Hz with a triangular ramp. Heat was provided by two quartz lamps radiant strip heaters. Damage was monitored by acetate edge replication and was quantified in terms of the initial modulus and the current modulus. They found that their work in conjunction with previous works yielded a good descriptive comparison of four test environments: 10 Hz at room temperature and at 650°C, 2 Hz at 427°C, and 0.02 Hz at 427°C. All data from the comparison confirms the existence of a fatigue strength limit of 370 MPa. They found that the two frequency groups had different strains at failure which led them to conclude two different modes of failure. Brittle

cleavage fracture of the matrix was the dominant influence on specimen failure. Cleavage fracture occurs when the crack follows preferred crystallographic planes within the material grains. The matrix tended to strain harden at high frequency. Low frequency tests were exposed to high temperature for a longer period of time. In these tests, the fibers failed prior to matrix failure. The matrix was noticed to age harden significantly. Mall and Portner observed that cracks initiated out of the interface primarily at the lower load levels. Higher load levels involved matrix cracks initiating from fractured fibers. In no test were they able to find evidence of delamination. They are satisfied with the performance of their instantaneous modulus damage parameter and believe that much work is needed to fully realize it's potential.

Pollock and Johnson (29:1-14) examined the behavior of unnotched SCS-6/Ti-15-3 at 650°C. Their goals were to gain an understanding of the material behavior at high temperature, compare their results with previous work, and to evaluate a constituent property relationship for predicting the material behavior. The specimens used for testing were $[0]_1$, $[0/90]_{23}$, $[0_2/\pm 45]_3$, and $[0/\pm 45/90]_4$. All fatigue testing was done with a 0.1 stress ratio and a frequency of 10 Hz. Monotonic tests were done at a loading rate of 0.273 KN/s.

Many conclusions were drawn, of which only the most pertinent ones are repeated here. They found that at high temperature, the fibers contribute more to tensile strength and fatigue endurance than the matrix. This is due to the softening of the matrix at high temperature. Multiple fiber breaks with no matrix cracking resulted from high strains and low life fatiguing. Conversely, matrix cracking with little fiber breakage was due to low strains and long life fatiguing. They also determined that the cyclic stress in the 0° fibers determined the composite's cyclic life.

Much work has been done in examining and characterizing the behavior of SCS-6/Ti-15-3 with and without holes at room temperature. A substantial number of investigations have also been performed on this material at elevated temperature, but in the unnotched configuration. This current study is thus needed to fully characterize the material's behavior.

III. Experimental Set-up and Procedures

Material

The material examined in this study is SCS-6/Ti-15-3 in a cross-ply laminate. Silicon Carbide fibers are embedded in a Titanium alloy matrix with a fiber volume fraction of 0.37. Mean fiber diameter is 142 microns. A typical fiber cross-section is shown in figure 2. A 48.4 micron thick region of bulk Silicon Carbide encases the inner Carbon core (38.4 microns in diameter). The outer coating is composed of alternating layers of Silicon and Carbon, and is 3.5 microns thick.

The matrix is an alloy composed primarily of Titanium (75% by weight) and Vanadium (15%) with 3% by weight of each of: Aluminum, Chromium, and Tin. EDAX (Electro-Dispersive Analytical X-Ray) analysis of the matrix reveals that the

Table I: Matrix Composition

	MANUFACTURERS DESCRIPTION	EDAX ANALYSIS
TITANIUM	75%	75.53%
VANADIUM	15%	15.41%
ALUMINIUM	3%	3.02%
CHROMIUM	3%	3.32%
TIN	3%	2.72%

material is close to the composition advertised by the manufacturer as shown in Table 1.

Material Preparation

The material used in this investigation was fabricated by Textron Specialty Materials Inc. They made the .3048 m x .3048 m composite panel by using the Hot Isostatic Press (HIP) process. HIPing involves alternating layers of fibers and matrix material then placing this packet of material into a high temperature pressure vessel where it is subjected to temperatures and pressures in excess of 1000°C and 35 MPa. During this process, the matrix material liquefies and flows into and around the fiber layers. In the cool down phase of processing, the matrix material solidifies and binds up the fibers. In general, HIPing results in better consolidation of the fibers and matrix than does other methods like cold isostatic pressing, vacuum hot processing, pultrusion, or compression molding. This better consolidation yields fewer voids and, consequently, a stronger material.

Specimen Preparation

The AFIT model fabrication shop cut ten specimens from the panel with diamond encrusted blades (see figure 3). Each specimen was 15.5 cm long, 19.05 mm wide, and 1.77 mm thick. Silicon Carbide fibers are very hard and can be cut only with

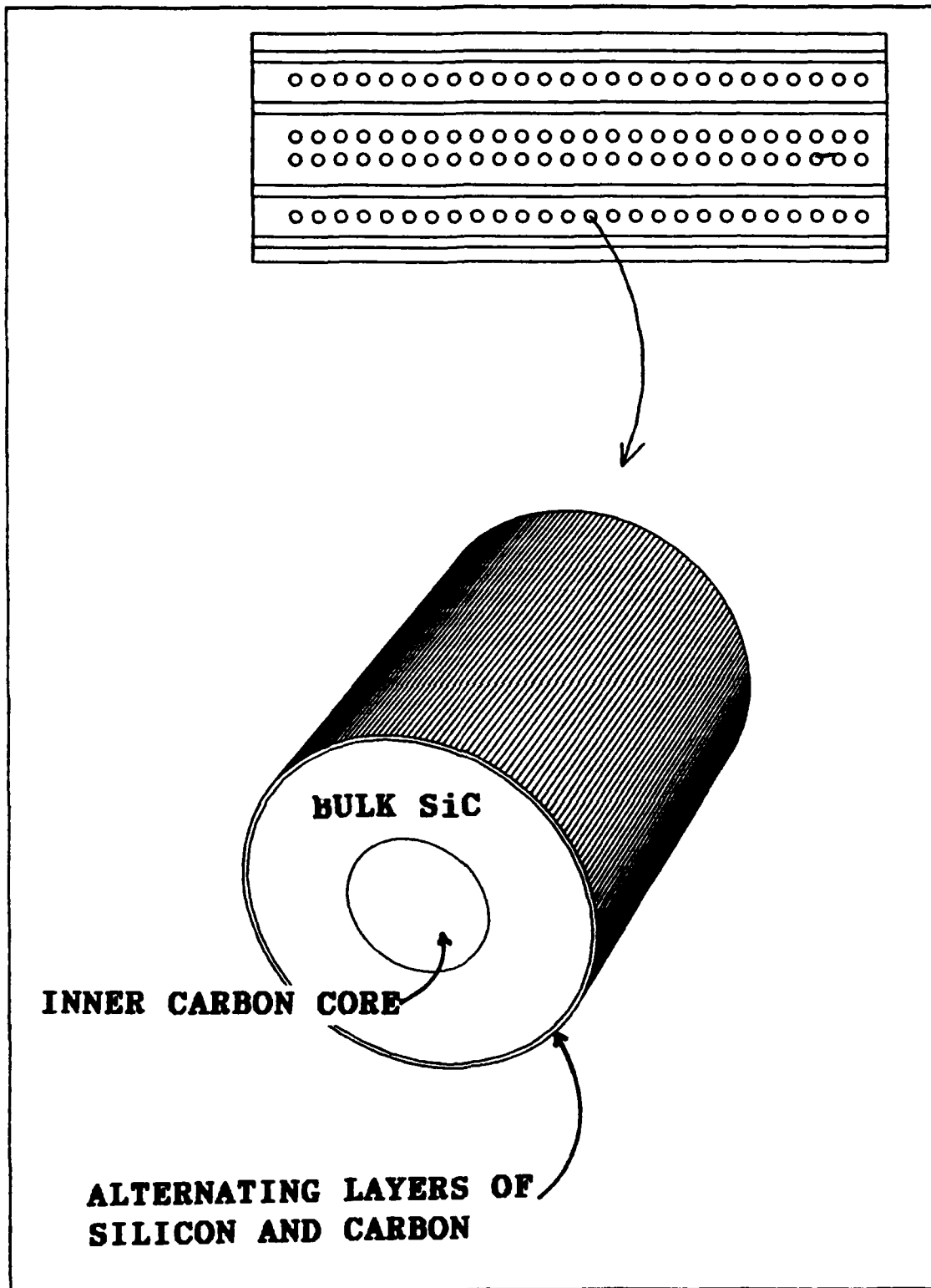


Figure 2: Typical Fiber Cross-section

diamond impregnated saw blades, providing a smooth cut with minimal waste due to the kerf.

Following cutting, the specimens were taken to the Aeronautical Systems Division (ASD) machine shop where a 3.175 mm diameter hole was drilled in the center of each specimen. To minimize damage, the holes were drilled ultrasonically. All of the holes were within 7.36% of the desired diameter.

Specimens were then subjected to heat treatment. Wright Laboratory (WL) technicians wrapped the specimens in Tantalum foil to act as a gettering surface for impurities ejected from the specimens during heat treatment. These specimens were then placed in a vacuum oven and subjected to 700°C and 1×10^{-6} Torr for 24 hours. This heat treatment was chosen because it stabilizes the alpha phase in the matrix and does not significantly alter the material properties from the as fabricated (ASF) condition.

Following heat treatment, the specimen's edges were processed to facilitate edge replication. Edge preparation progressed in two stages. The first stage was to grind the specimen edge on a Buehler Maximet automatic polisher with a number eight Metlap platen using a 45 micron diamond slurry followed by a 15 micron then a 9 micron slurries. The second stage of edge preparation was fine polishing. For this stage the Automet polisher was used in conjunction with a Buehler

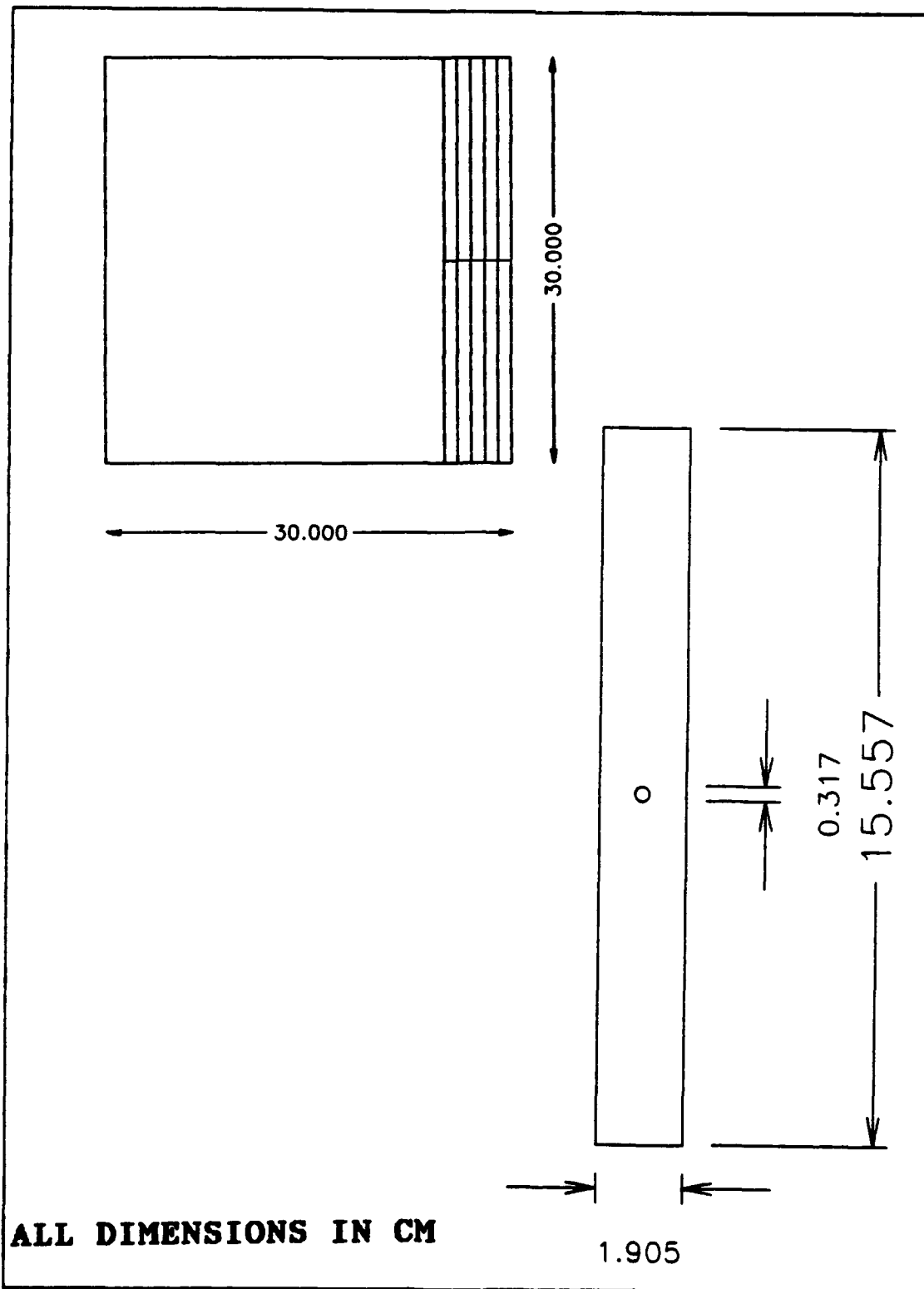


Figure 3: Specimen cutting details

Perfmat and 9 micron slurry followed by 3 micron then 1 micron slurries. The final product had no scratches larger than 1 micron (in theory). Following grinding and polishing, the edge to be used for replication was inspected microscopically at 50x and 100x magnifications for damage induced by cutting, grinding, and polishing. Finally, a photographic record of the region near the hole was made for future reference.

Test Apparatus

All tests were run on a Material Test System (MTS) 808 test stand with 22 KIP load cell. To provide the heating, the test stand was equipped with two parabolic lamps. Chilled water was circulated through the upper and lower grips as well as through copper tubing wrapped around the load cell in order to protect the load transducer from the high temperatures. Strain was measured with an MTS model 632.50b-04 12.7 mm gage length extensometer which was cooled by chilled air. A Zenith Z-248 computer was used for program control and data acquisition (see figure 4). Specimen temperature was maintained at $427' \pm 3' \text{ C}$ over a 38.1 mm gage length by a Micricon 825 microprocessor. The Micricon 825 provided feedback signal processing and output control of the heat lamps. Two type k chromel-alumel thermocouples were tack welded to the specimen to provide temperature information to

the Micricon 825. To permit both even temperature distribution and enough room to take replicas, the thermocouples were placed 19.05 mm apart. A third thermocouple was tack welded 2.5 mm away from the hole on the center line (see figure 5). This thermocouple was used to monitor temperature distribution. Radiant Energy Research Inc manufactured these lamps which incorporate 1,000 watt tungsten filaments.

The Zenith Z-248 ran a program called MTEST which was developed by Capt Brian Sanders, an AFIT doctoral candidate. This program provided the 10 Hz input signal to the MTS micro-profilier which drove the load actuator. MTEST recorded maximum and minimum stress and strain, temperature, and modulus. Strain data was sampled every 100 cycles and the modulus was sampled every 1000 cycles.

Acetate Replicas

It is almost impossible to observe crack growth and damage directly during testing. If the specimen is removed from the test stand, small cracks will close, leading to inaccurate assessment of crack initiation and measured crack length. One good way to monitor crack initiation and growth with the specimen under load is via acetate replication.

In this method, the test is placed on hold, temperature is reduced to ambient levels, and the load is adjusted to 50%

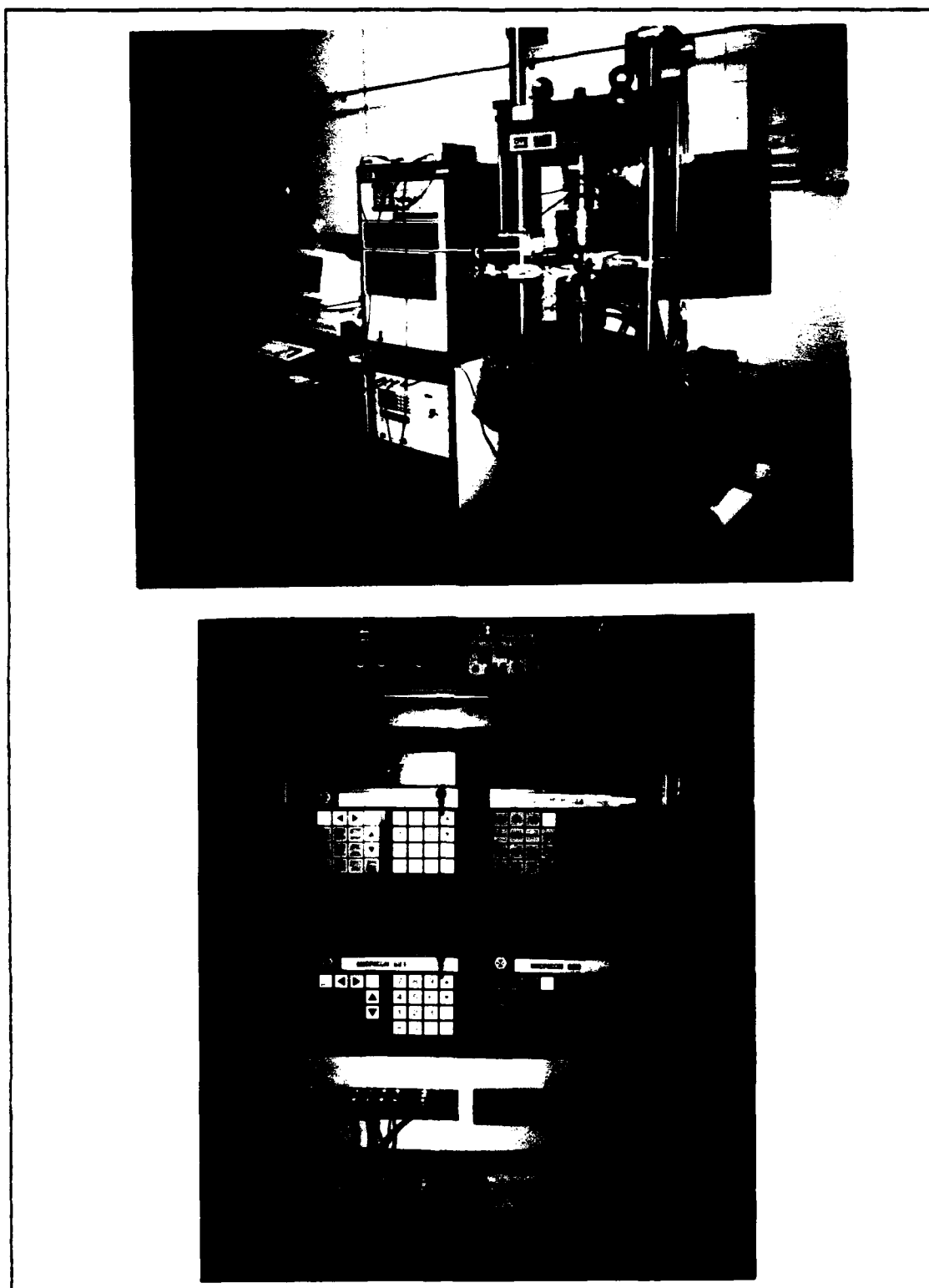


Figure 4: Test Apparatus

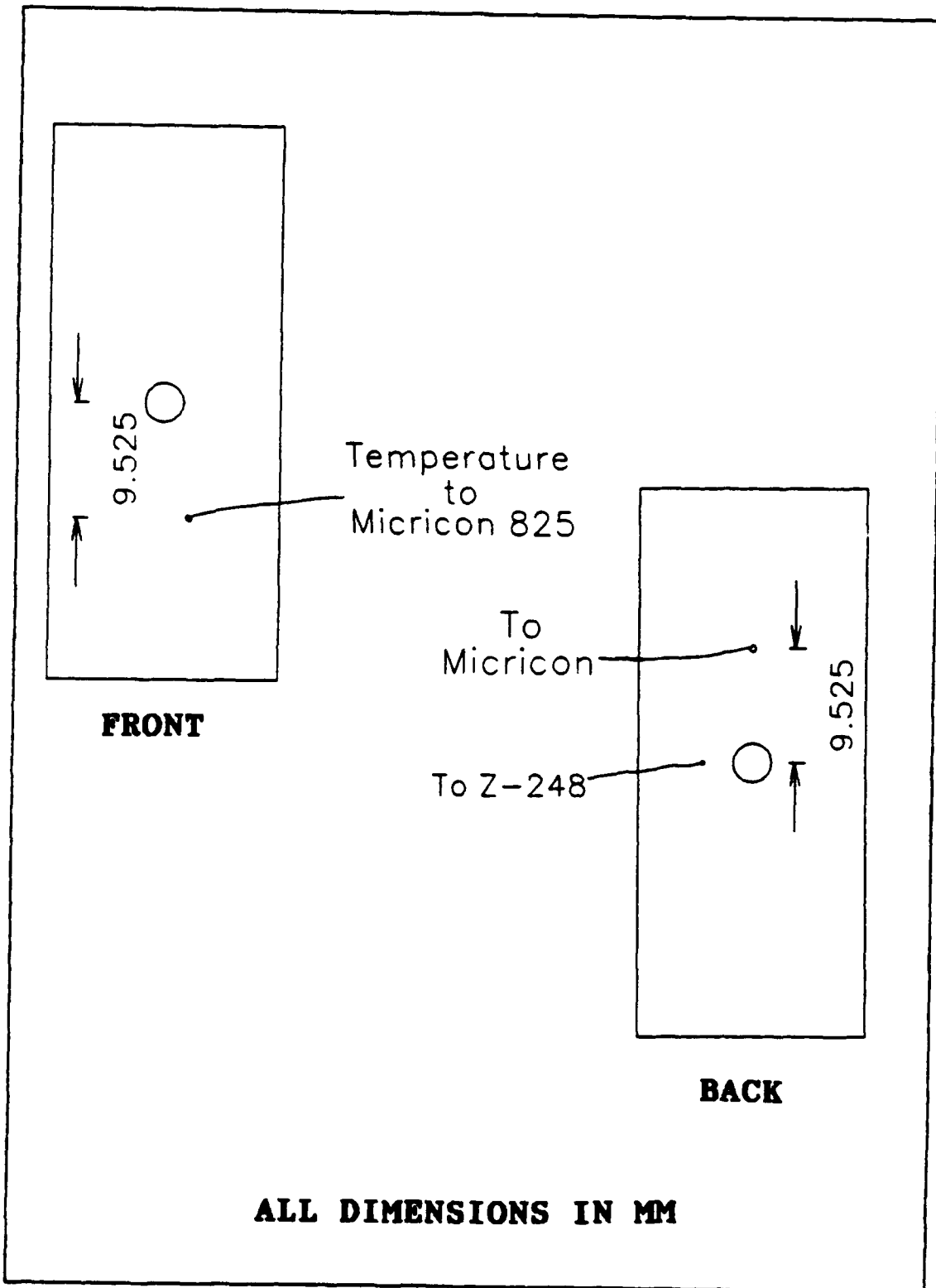


Figure 5: Thermocouple welding diagram

of the maximum load. A piece of acetylcellulose is cut to the desired size and taped to the portion of the specimen to be replicated. To make the replica, the specimen surface is wetted with acetone, then the acetate is pressed on to the surface. The acetate melts partially and flows into cracks, crevices, and the like. After the acetate resolidifies, the replica is removed from the specimen and can be examined under the microscope.

The Scanning Electron Microscope (SEM) provides an excellent means for examining face replicas. The particle measurement system of the SEM is ideally suited to measuring the length of cracks recorded by the face replicas. To ensure uniform measurement, all crack length readings were performed at 30x magnification.

Test Procedures

Each specimen was placed in the test fixture such that the 0° fibers are aligned with the loading direction. The ends of the specimens were clamped with a pressure of 6.9 MPa by the hydraulic grips. The specimen orientation was checked by a spirit level. The 12.7 mm gage length extensometer was placed on the right edge of the specimen. Following initial specimen placement, the temperature was brought up to 427°C so that the thermal strain of the material could be recorded. The modulus was then checked by loading the specimen with

1,112 N (corresponding to 34.5 MPa). After the modulus test, load controlled fatigue was initiated at a frequency of 10 Hz with a load ratio of 0.1 and a triangular wave form.

Every 2,000 - 10,000 cycles (depending on stress level) the test was placed on hold to take replicas. Prior to cooling the specimen for replicating, the load, temperature, and hot strain values were recorded. As the specimen cools, the region around the hole on the specimen face is examined for cracks using a telemicroscope. Replicas were then made of the edge, front face, and back face. These replicas were then examined by an optical microscope to ensure good images were obtained. Once good replicas were acquired, the specimen was reheated to 427°C and the strain was permitted to reach the hot strain value recorded prior to cool down. Next the test was restarted from hold.

Crack initiation was defined to have occurred when a crack reached a length of at least 0.124 mm. Once cracks initiated, the holds for replication were changed to every 10,000 to 100,000 cycles (depending on stress level). At high stress levels the specimens had shorter lives and thus the stops for replication needed to be more frequent. Low stress level tests had much longer specimen lives and consequently needed less frequent stops for replicas.

Eight tests were run. The first was an elevated temperature static test. As a measure of the damage far from

Table II: Test Matrix and Post-Processing

SPECIMEN NUMBER	STRESS LEVEL (MPa)	POST PROCESSING
1	STATIC	SECTION, POLISH
2	240	SECTION, POLISH
3	400	SECTION, POLISH
4	300	SECTION, POLISH
5	170	SECTION, POLISH
6	225	SECTION, POLISH
7	425	SECTION, GRIND, POLISH, ETCH
8	300	SECTION, GRIND, ELECTRO POLISH

the hole (henceforth referred to as "far field"), the extensometer was placed three hole diameters away from the centerline of the hole as was shown in figure 5. At this distance, the stress concentration effects of the hole are minimized. This test was used to establish the tensile strength and the stress level associated with the well documented "knee" in the stress - strain curve. From this curve, the stress levels for the fatigue tests were determined. Table II shows the test matrix and the related post failure processing. In the second test, the extensometer was placed far field in order to characterize the damage away from the hole. Specimens three through eight had one

extensometer rod on each side of the hole (henceforth referred to as "enclosing the hole"). This is shown in figure 6. Table three shows the test matrix. The last specimen, number eight, was fatigued until large cracks developed. Once this test was stopped the specimen was sectioned and mounted such that the entire hole and all cracks could be observed microscopically.

Post-Failure Analysis

Once a specimen failed, the fracture surface was observed visually for color, fiber pullout, and overall appearance of the fracture. Following initial inspection, the specimen was then sectioned as shown in figure 7. The fracture surface was then examined via SEM to characterize the failure. Some of the details noted were the type of failure (i.e. brittle or ductile), transition zones, and cracking within the hole.

Other non-fracture surface sections were mounted in Buehler Konductimet, a conductive mounting compound, using a Simplimet mounting press. First the specimen section was cleaned in Isopropanol, mounted, then it was rough polished on the Maximet with a number eight platen then a permat using 45 micron diamond slurry followed by 15 micron then 9 micron slurries. To provide a smooth surface, the mounted section was placed on a Buehler Vibromet vibrating polisher with a one micron diamond slurry for 24 hours. This eliminates all

Table III: Test Matrix

	MAXIMUM STRESS LEVEL	EXTENSOMETER POSITION
1	STATIC TENSION	FAR FIELD
2	240 MPa	FAR FIELD
3	300 MPa	ENCLOSING
4	400 MPa	ENCLOSING
5	170 MPa	ENCLOSING
6	225 MPa	ENCLOSING
7	425 MPa	ENCLOSING
8	300 MPa	ENCLOSING

scratches larger than one micron. Next the mount is transferred to a Vibromet with half micron diamond slurry for 24 to 48 hours. Finally, the mount is transferred to Mastermet, an aggressive chemical polish which removes all scratches larger than 0.06 micron, for 30 to 45 minutes. After polishing, the mounted section is ready for SEM examination. This examination entailed looking for cracks within the matrix and/or fiber, debonding around the fibers, and matrix plasticity.

The last specimen was sectioned and mounted such that the hole and all of the cracks could be observed. The mounting procedure for this specimen was exactly the same as before. Following mounting, this specimen was hand ground on abrasive

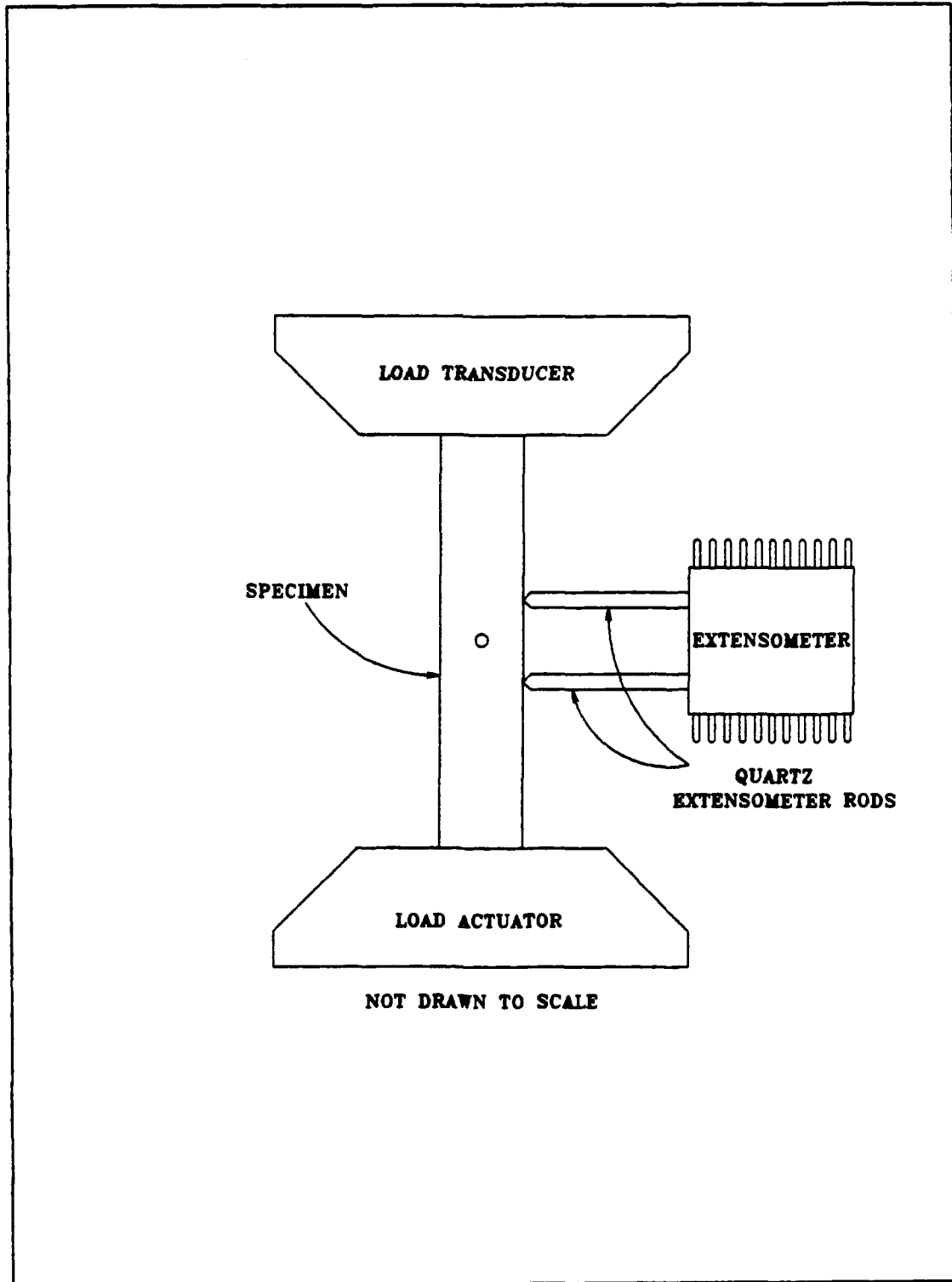


Figure 6: Strain Measurement Equipment (with extensometer "enclosing" the hole)

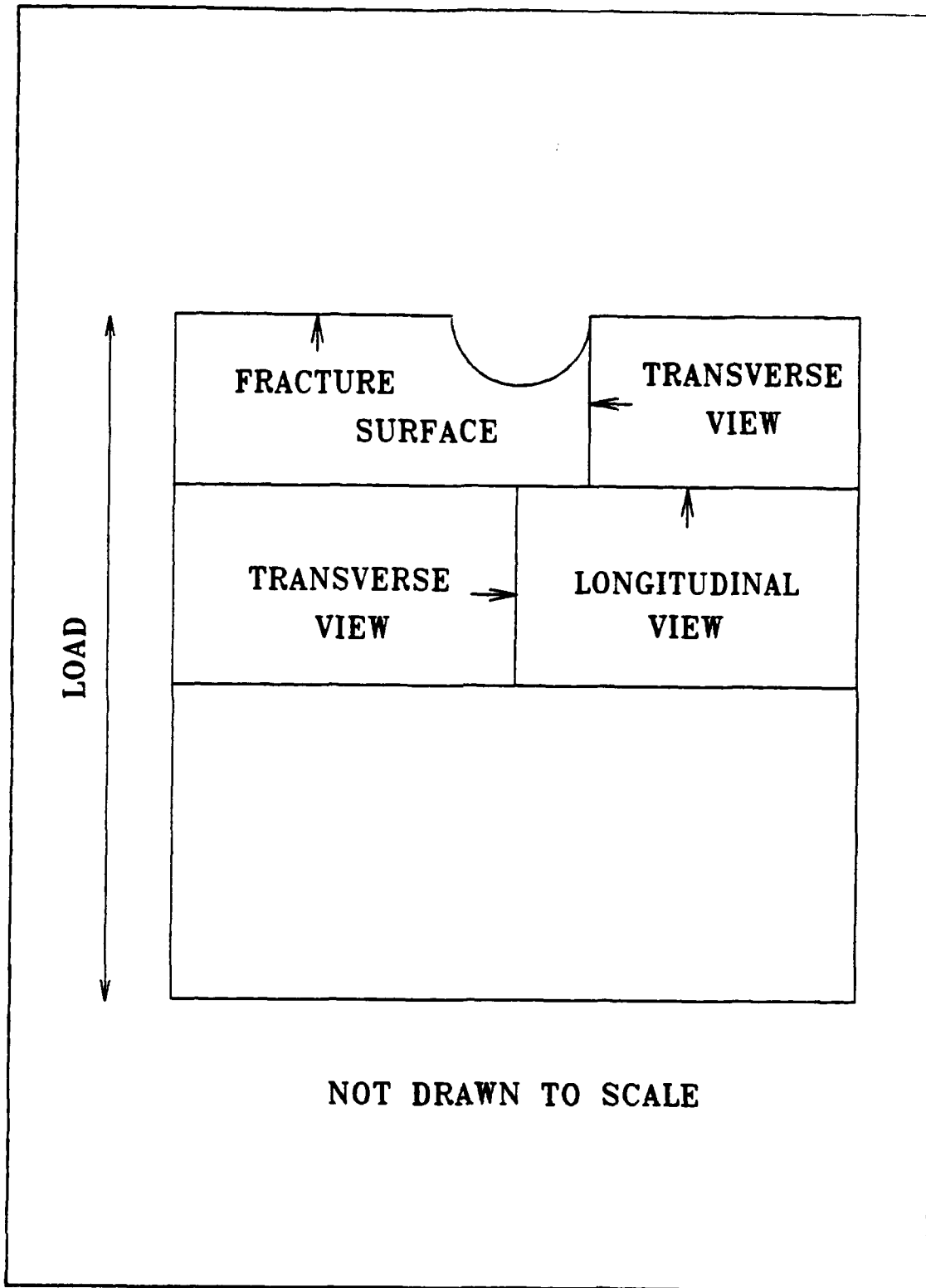


Figure 7: Specimen sectioning diagram

disks proceeding from 180 grit to 800 grit. When the fibers became exposed, the specimen was placed on a stainless steel mesh Vibromet with one micron diamond slurry for eight hours. The specimen was then transferred to the half micron Vibromet for 24 hours followed by an hour on the 0.06 micron Mastermet. This was done to ensure a smooth surface for evaluation while inducing minimal damage to the section.

Specimen number seven was sectioned, mounted, and polished to a 0.06 micron finish as before. The main difference is that the outer layer of matrix material was not removed. This specimen was then electropolished and etched with a three percent solution of Ammonium Fluoride and Hydrofluoric Acid ($\text{NH}_4\text{F}+\text{HF}$) to bring out grains, grain boundaries, and slip bands.

IV. Results and Discussion

As mentioned previously, the objective of this research was to investigate the initiation and progression of cracks which develop in notched $[0/90]_{28}$ SCS-6/Ti-15-3 at elevated temperature. To accomplish this, fatigue testing was conducted at 427°C with a load ratio of 0.1 and a frequency of 10 Hz. The fatigue cycles for initiation and failure were recorded as was the crack growth rate.

Damage was monitored in two fashions. First, during the testing, strain change and stiffness change were recorded and correlated to observed damage. Second, damage progression was observed with telemicroscope and recorded by acetate replication of the specimen face and edges. The face replicas were examined for crack initiation which was defined to be the point at which a crack exceeded 0.124 mm in length. Crack length was measured at each replication interval by the SEM's particle measurement system. This length was then plotted as a function of the number of cycles.

Failure was characterized by metallographic examination of the specimen sections (see chapter 3 figure 7) and by fractographic analysis of the fracture surface. Each section was then inspected for signs of debonding, cracking, and matrix plasticity. The fracture surfaces were scrutinized for

failure mode, matrix yielding, and crack development within the hole.

Terminology

To ensure a clear understanding of explanations contained herein, some definitions must first be made. Two cross-sectional areas are involved in this research: nominal cross-sectional area and reduced area (see figure 8). All stresses referenced are based on the reduced area.

The exact moment of crack initiation is ambiguous because crack detection is dependent upon the capabilities of detection equipment as well as the investigator's expertise in interpreting the data. Often, different researchers will report different numbers of cycles to initiation. Generally, a minimum detectible crack length is established: for this study, crack initiation is said to have occurred when a crack length of .124 mm has been obtained. This minimum length was chosen because of the resolution limitations of the detection techniques employed.

Cracks tend to form at four points around the hole's periphery. These initial cracks are referred to as minor cracks. Two of the four cracks become dominant and will be referred to as either major cracks or dominant cracks. The two cracks which do not grow as rapidly as the major cracks are referred to as either minor cracks or secondary cracks.

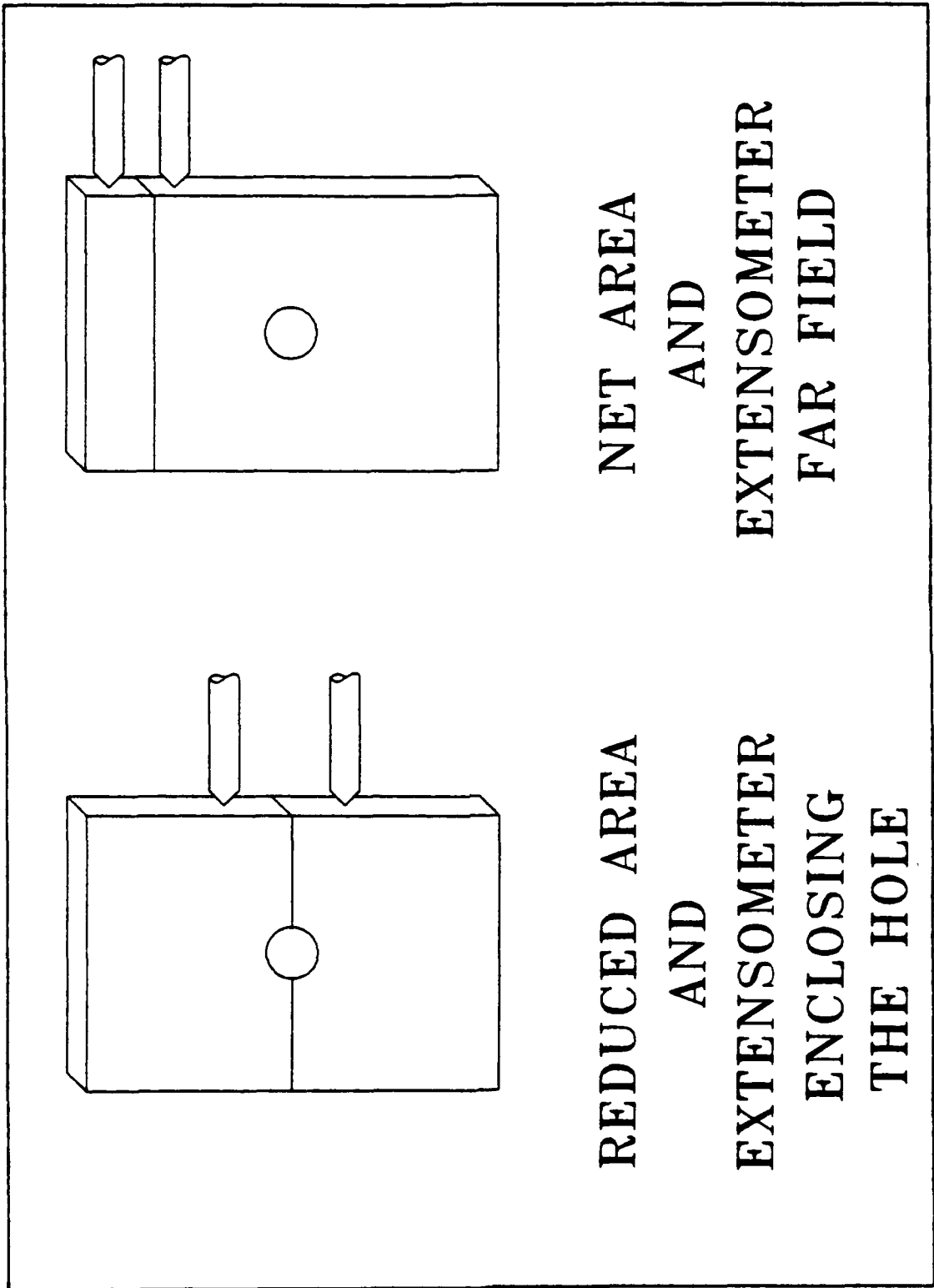


Figure 8: Cross-sectional area definitions

When dealing with notched specimens, the placement of the strain measurement equipment is important because strain and modulus will change depending on the measurement site. Two locations for extensometer placement were used and are termed either "far field" or "enclosing" the hole. "Far Field" measurements were taken three hole diameters away from the hole to minimize the effects of the stress concentration. The purpose of this was to get an idea of the unnotched material response. Measurements with the extensometer "enclosing" the hole were used to determine the effect of the hole on the composite's response. For this measurement, each leg of the extensometer was placed on opposite sides of the hole.

Cyclic Life

The number of cycles to initiation and to failure at each stress level are listed in Table IV. These values are used to generate the S-N curves shown in figures 7, 8, and 9. These curves portray the "typical" fatigue life of the material at 427°C.

The initiation curve, shown in figure 9, indicates the number of cycles needed at a given stress level required for cracks to form. This curve reflects the point at which the first detectable crack appeared on either the front or back face of the specimen. Specimens subjected to fatigue loading below the first ply failure level (180 MPa, unnotched)

Table IV: Test Results

SPECIMEN ID	STRESS LEVEL (MPa)	CYCLES PRIOR TO OBSERVED INITIATION	OBSERVED CYCLES TO INITIATION	CYCLES TO FAILURE
2	240	20,000	25,000	494,234
3	400	5,500	7,500	18,940
4	300	10,500	12,500	155,139
5	170	8,500,000	>8,500,000	NO FAILURE
6	225	40,000	50,000	703,968
7	425	2,000	4,000	14,202
8	300	7,000	9,000	STOPPED

exhibited no visible damage even up to 8.5 million cycles.

Figure 10 shows the stress plotted against the number of cycles to failure for each associated stress level. This curve depicts the number of cycles which may be expected to cause failure at a given stress level.

To examine the interrelationships between the initiation and failure curves, figure 11 includes both plots. Observe that at low stress levels the curves become almost parallel indicating that the specimen will not fail.

S-N Curve Comparisons. Figure 12 incorporates data from Portner (30:29), and Naik and Johnson (24:22) in comparison with current data. Portner performed elevated temperature

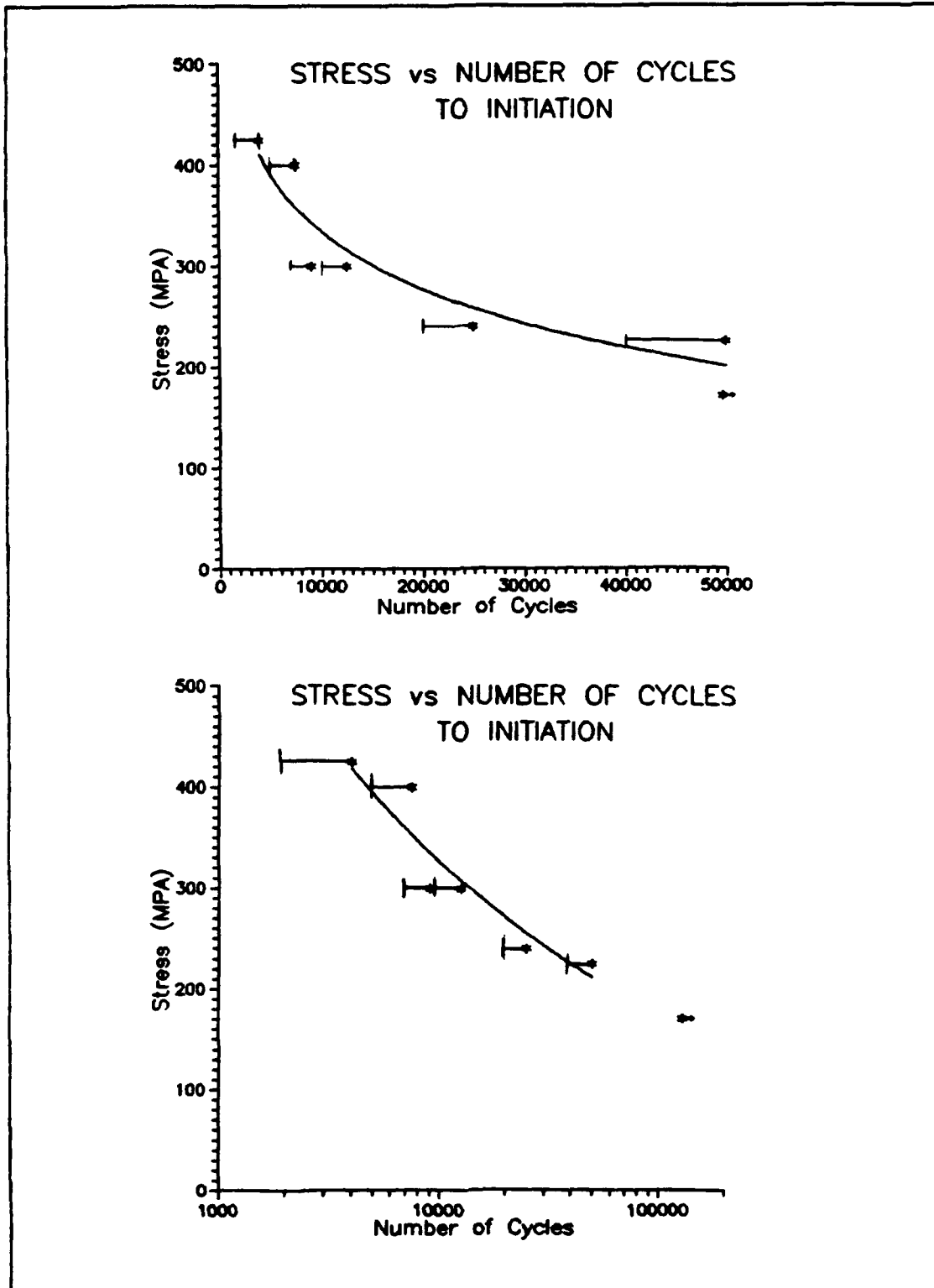


Figure 9: Crack Initiation S-N Curve

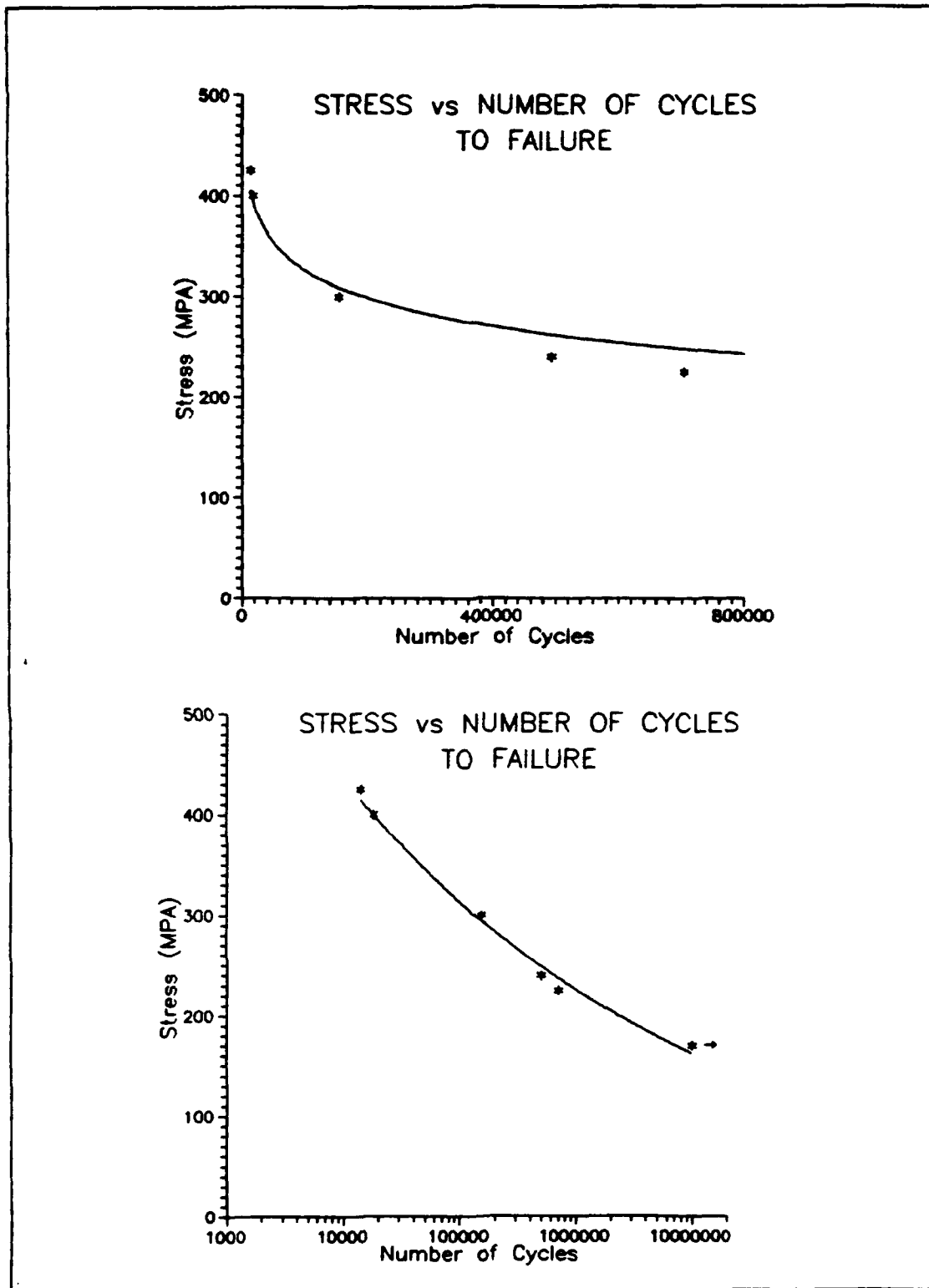


Figure 10: Failure S-N Curve

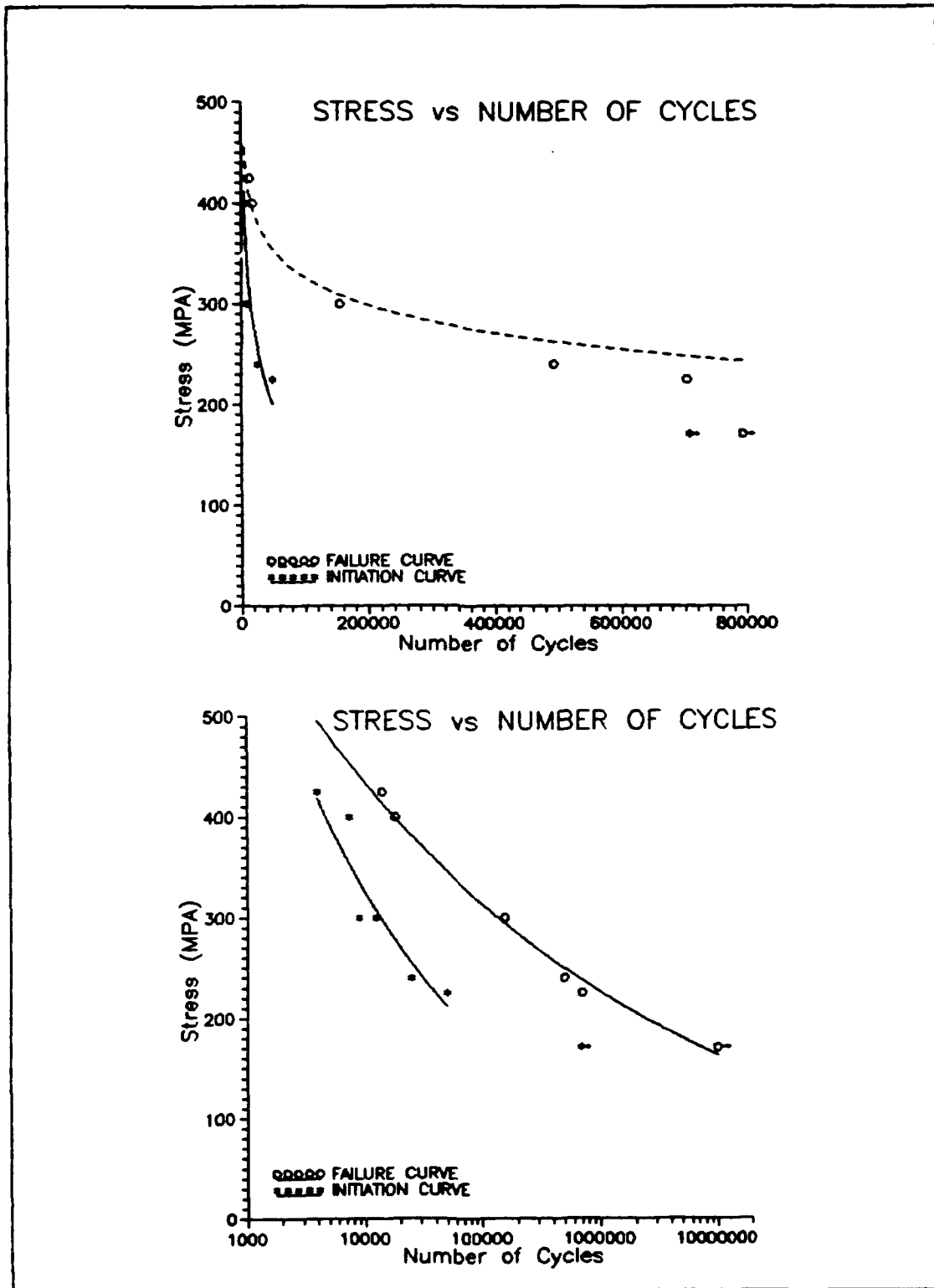


Figure 11: Initiation and Failure S-N Curves

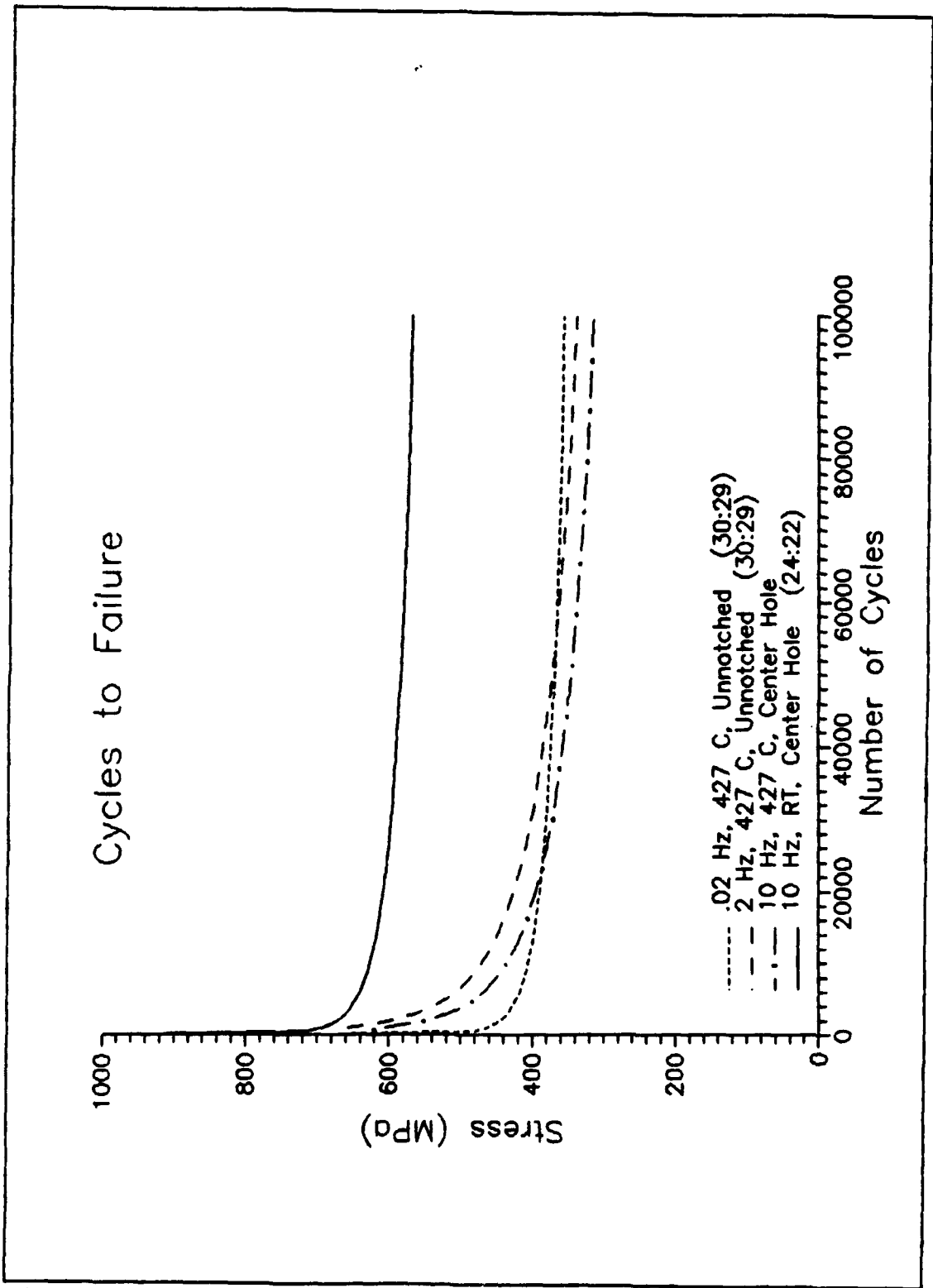


Figure 12: Comparison of Cyclic Failure

(427°C) tests of the same material and $[0/90]_{28}$ ply lay-up at two frequencies, 2 Hz and 0.02 Hz, both of which involved unnotched specimens. The low frequency (0.02 Hz) specimens were subjected to high temperatures for long periods of time resulting in strain hardening of the material. At the lower load levels (below 360 MPa), this means that low cyclic frequency specimens will have a longer life than those at high frequency. Here the presence of the center hole does play a slightly larger role in determining the life of the low load specimen.

High load levels (above 400 MPa) result in shorter life and are influenced more by the cyclic frequency than the presence of a center hole. For a given load level, the expected life is shortest for the low frequency specimens, followed by the high frequency notched specimens, then the high frequency unnotched specimens.

When looking at the overall S-N regime of figure 12 observe that, at high temperature, the presence of a center hole has little effect on the fatigue life of the material. Indeed, Figure 12 shows that elevated temperatures play a much larger role in fatigue life than does the presence of the center hole. The expected life of the notched material at high frequency and ambient temperature is orders of magnitude greater than any of the elevated temperature specimens - notched or unnotched.

Tensile Test

A tensile test at elevated temperature was performed to establish the material's baseline high temperature performance. The associated stress-strain curve is displayed in figure 13. To characterize the unnotched material, this test was performed with the extensometer measuring the far field strain. At 427°C, the notched specimen exhibited a bilinear response at 180 MPa. At this point the 90° fibers debond from the matrix. Notched specimen tensile strength at elevated temperature was determined to be 587 MPa (which corresponds to an unnotched strength of 408 MPa). The far field modulus was found to be 122 GPa. Portner reports an unnotched strength of 890 MPa at room temperature and 740 MPa at 427°C. This is a 21% decrease in tensile strength is due to the presence of the hole.

Strain Curves

Damage progression was monitored during the testing by plotting the total strain measured across the hole against the number of cycles. Figure 14 shows the strain at the reduced cross-section plotted as a function of the number of cycles to failure. Observe that the strain increases steadily over the life of the specimen. As it approaches failure, the strain increases rapidly. Use of this method proved valuable in determining when to stop the test for replicas prior to

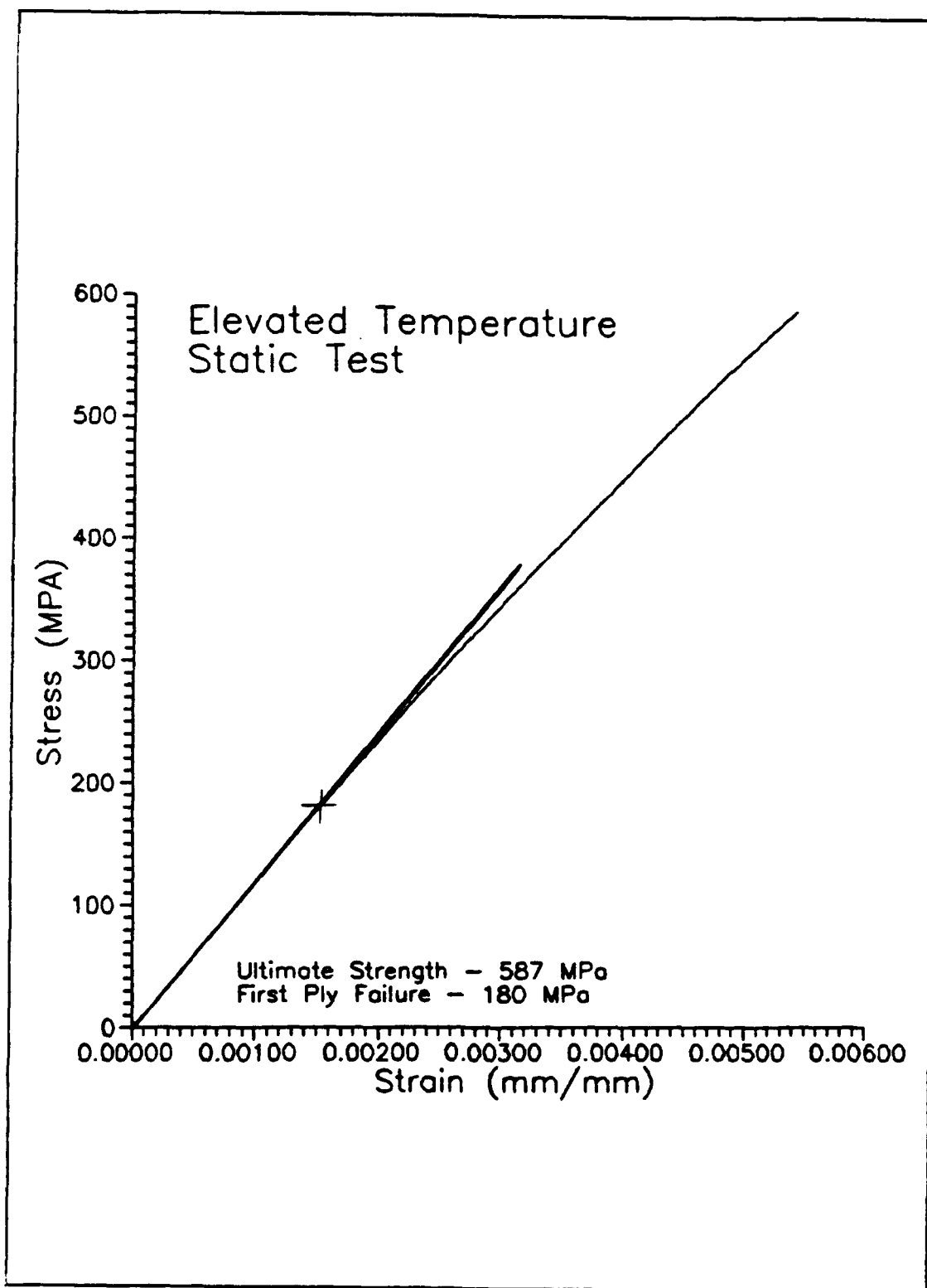


Figure 13: Monotonic Tension Test

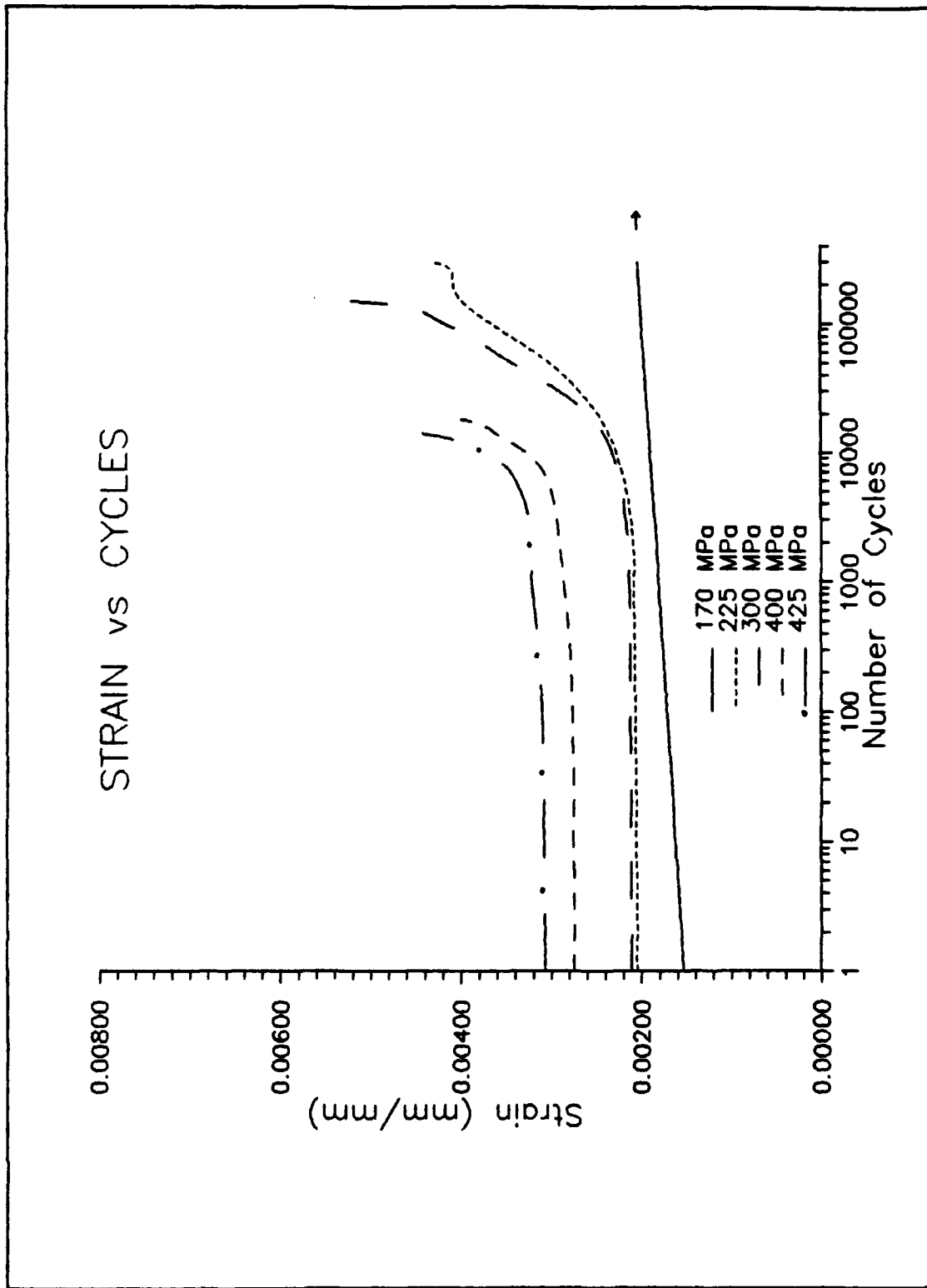


Figure 14: Strain vs. Cycles to Failure

failure. Individual strain curves are in appendix 1.

From figure 14, observe that the material response can be divided into either high stress or low stress categories by noting the maximum strain level. The high stress category includes the 400 MPa and 425 MPa tests. Stress levels between 170 MPa and 300 MPa (inclusive) compose the low stress category.

High stress tests were characterized by high strains and short lives; whereas, the low stress tests have lives which are an order of magnitude higher than those of the high stress. Once cracking initiates in the high stress specimens, failure follows within 10,000 cycles. Low stress tests, on the other hand, could last hundreds of thousands of cycles after crack initiation which is indicative of slow crack growth.

As mentioned earlier, the position of the extensometer is critical in monitoring the damage progression. Figure 15 demonstrates the effect of extensometer location on the strain reading. Far field placement of the extensometer records only the damage occurring within the extensometer gage length. Observe that the strain remains constant over the life of the specimen then as it approaches failure, the strain increases slightly. This increase is due to damage in the region away from the hole. In contrast, the strain measured with the extensometer enclosing the hole continually increases over the

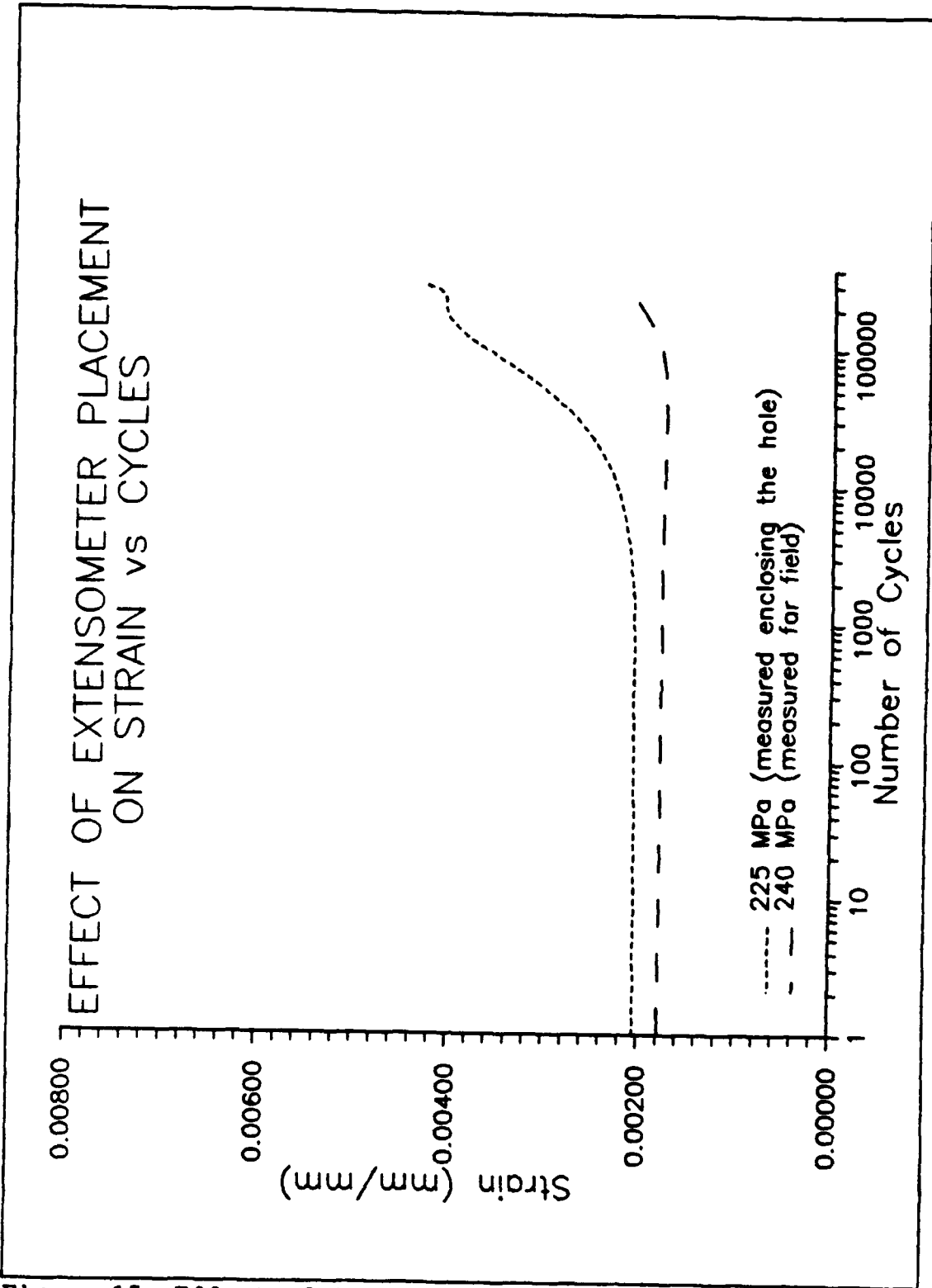


Figure 15: Effect of Extensometer Placement

specimen life. The strain is then seen to drastically increase as the point of failure is approached. In this case, the strain increase is due to matrix yielding followed by crack initiation and progression. Far field extensometer placement does not capture this aspect of damage in the region of interest. For this reason, the extensometer was placed enclosing the hole.

Modulus Curves

As with the maximum strain, instantaneous modulus was plotted against the number of cycles then used to monitor the progression of damage. The instantaneous modulus was found by dividing the change in applied stress by the change in mechanical strain for a given cycle. Note from figure 16 that through out the life of the high stress specimens the stiffness is continually decreasing. The low stress specimens, however, show an increase in modulus over the majority of the specimen life followed by a large decrease as the point of failure is approached (see figure 17). This apparent strengthening was shown by Portner (30:71-82) to be due to strain hardening of the material caused by prolonged exposure to high temperatures. The large stiffness decrease prior to failure is attributed to damage effects overriding the strengthening effects. Individual modulus curves are located in appendix 2.

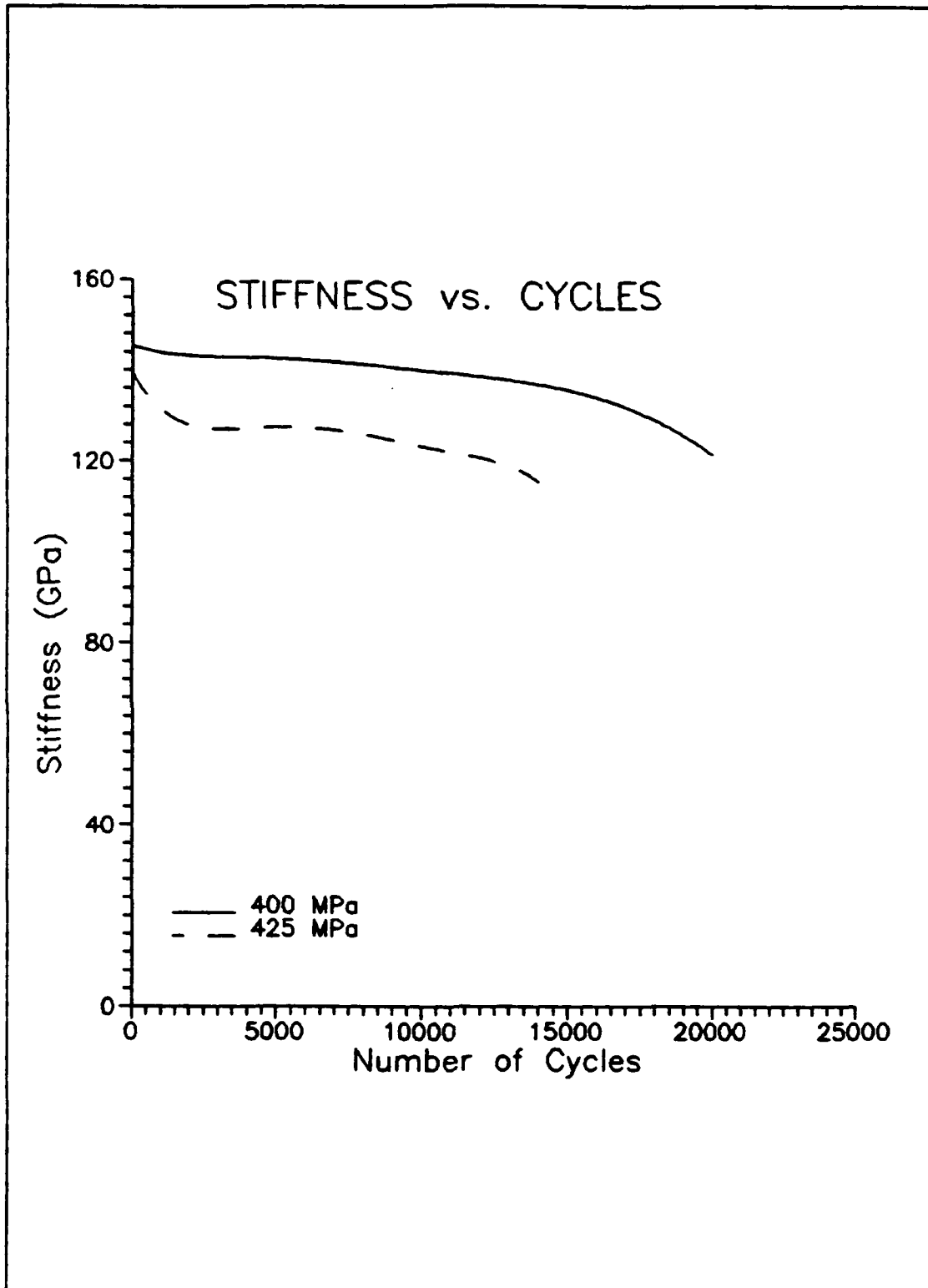


Figure 16: High Stress Stiffness vs Cycles to Failure

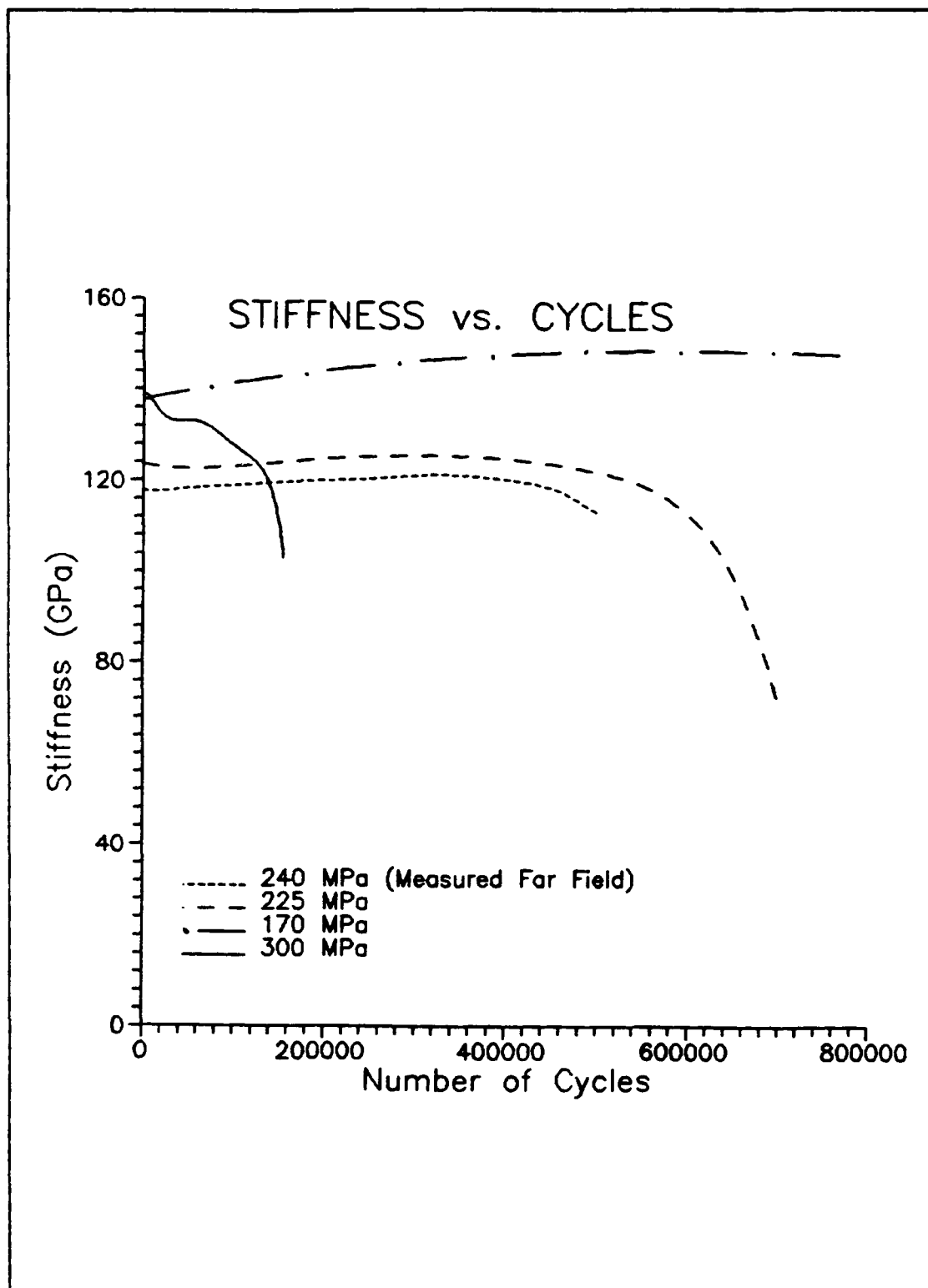


Figure 17: Low Stress Stiffness vs. Cycles to Failure

Strain Range is the difference between the maximum strain and the minimum strain, and may be used to monitor the damage. The modulus may be thought of as the stress range divided by the strain range (i.e. $\Delta\sigma/\Delta\epsilon$). Figure 18 shows the strain range of a high stress test and a low stress test. Note that as the number of cycles increases the strain range also increases. With a constant stress ratio, this implies that the modulus reduction is due to the increase in the strain range.

Crack Initiation and Growth

This section discusses the findings of microscopic evaluation of edge and face replicas, fracture surfaces, and specimen sections. Crack growth curves for high and low stress levels are then examined and compared to the microscopic observations. Damage progression is then compared to the room temperature findings of Johnson et al (3 and 11). Following a quantitative analysis, a clear picture of the damage progression is then drawn.

Replica Evaluation. Replicas taken during testing were examined by optical microscope for clarity and quality. Face replicas and selected edge replicas were then carbon coated for SEM examination. Each type of replica will be addressed separately.

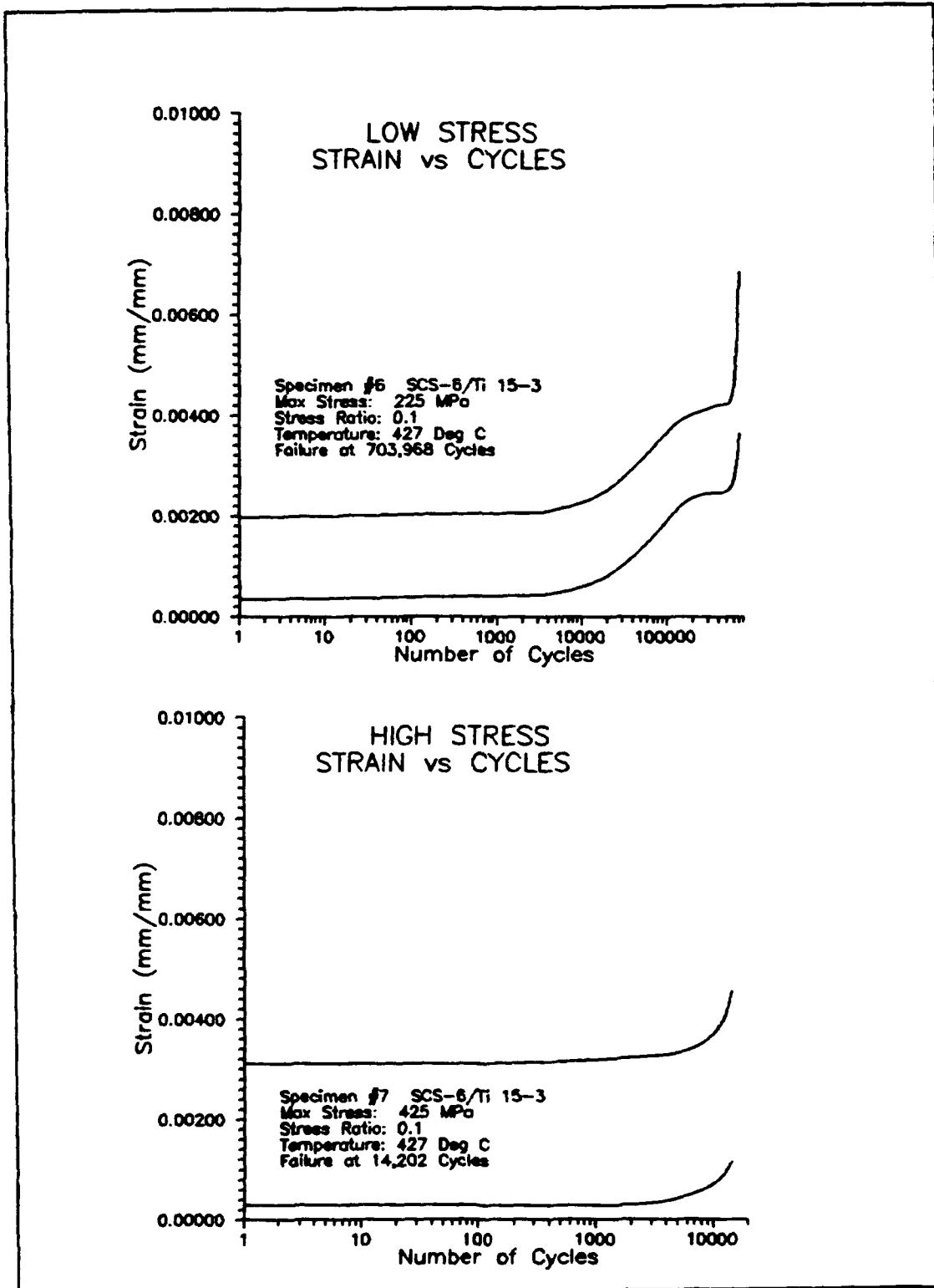


Figure 18: Strain Range

Edge Replicas. Edge replicas revealed that the 90° fibers in the region near the hole (within 2 hole diameters) debonded first (see figure 19). As the stress in the reduced area section exceeds the first ply failure level (180 MPa), debonding occurs. At this point, the far field stress is still below the first ply failure level and the 90° fibers have not yet debonded. When the far field stress reaches 180 MPa the 90° fibers debond. Typically, this happened on the first cycle of fatigue loading. When the reduced cross-sectional stress is between 180 MPa and 220 MPa debonding will occur in

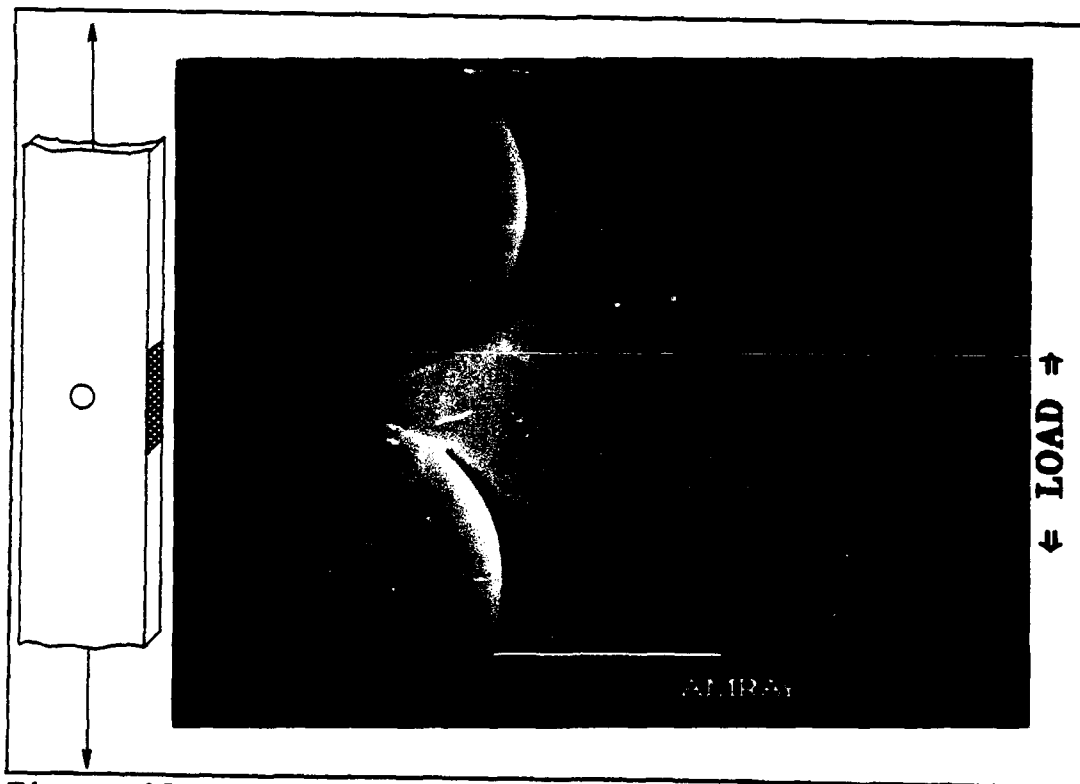


Figure 19: Debonding of 90° fibers (300 MPa Edge Replica)

the region adjacent to the hole while 90° fibers in the far field region remain bonded.

The only other damage noticed on the edge were longitudinal cracks emanating from the points where the 0° fibers enter and exit the matrix. This type of cracking was observed early in the life of the high stress specimens and much later in the low stress specimens. Little other damage transpired during the testing. No transverse cracking was noted. In contrast, Portner (30:35-37) noted that the edge of the unnotched specimen at 427°C witnessed transverse cracking. The hole sufficiently weakens the material so that this behavior is not seen in this experiment.

Face Replicas. Face replica examination revealed that cracks initiate at four points around the periphery of the hole on both front and back of the specimen. These minor cracks formed between 60° and 80° from the loading axis (see figure 20). Newaz and Majumdar (27:1-11) showed that for a $[0]_g$ unidirectional MMC at room temperature, cracks initiated between 65° and 72° from the loading axis due to large shear stress components. Two of the four minor cracks continued to grow and become dominant while the other two cracks either stopped growing or grew at a significantly slower rate. The two cracks which continued to grow will be referred to, interchangeably, as dominant or major cracks. Likewise, the two remaining cracks will be referred to as minor cracks.

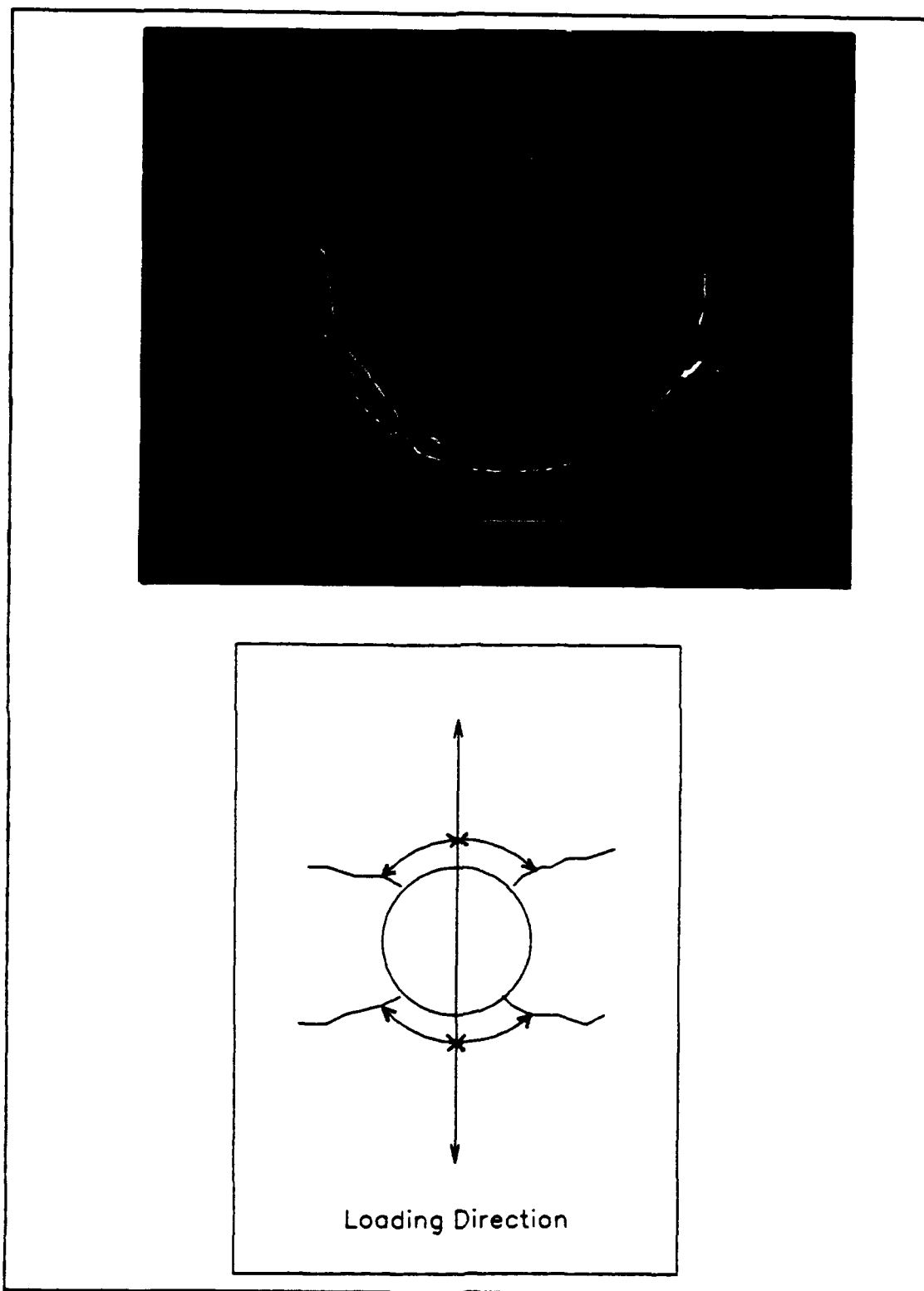


Figure 20: Crack Initiation Sites

Fatigue cracks on the face of specimens subjected to high stresses (above 400 MPa) exhibited crack bifurcation and the formation of tiny, discontinuous fatigue cracks parallel to the major cracks (see figure 21). These tiny, discontinuous

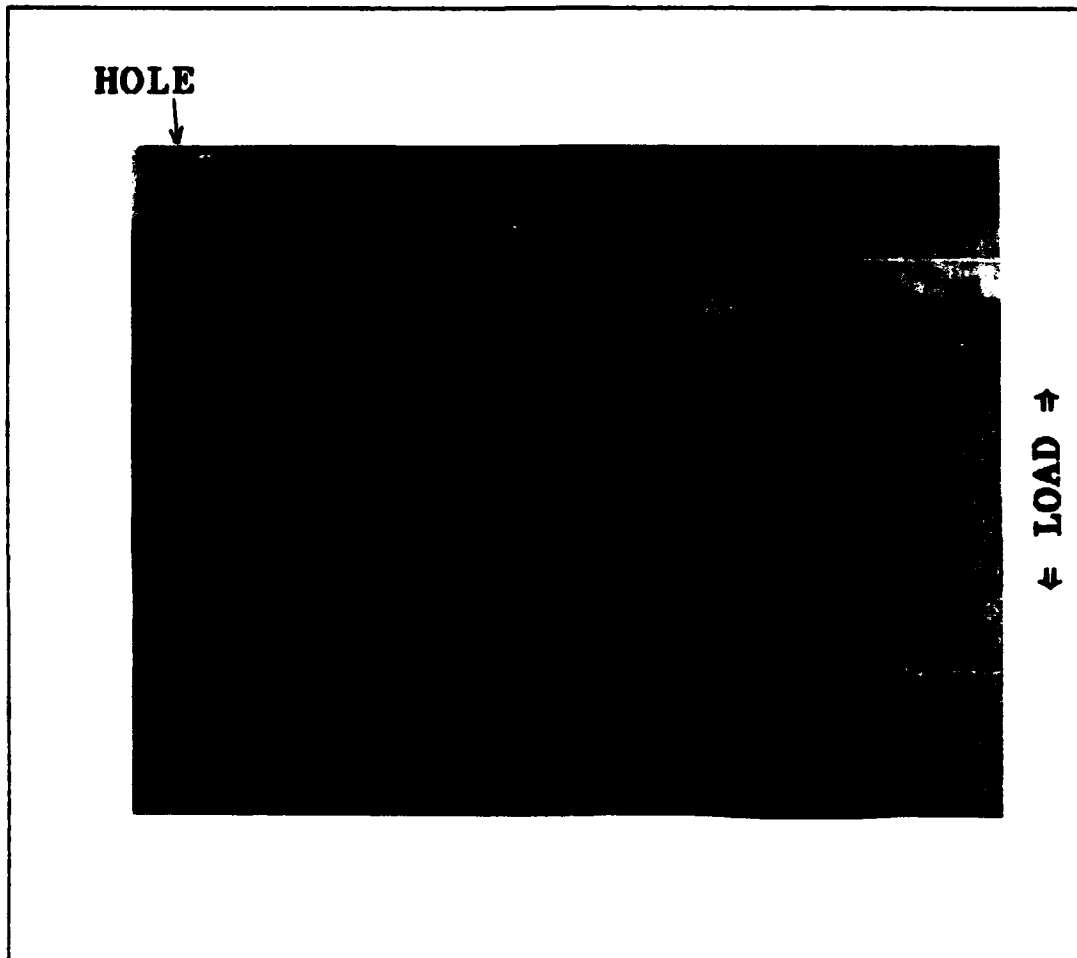


Figure 21: Crack Bifurcation on High Stress Specimen Face (100x)

fatigue cracks were located on each side of the major crack about 100 microns away. During testing, they were observed to initiate at the same time as the minor face cracks. These

cracks were not found in the far field region and appear to be caused by the high stress region created by the presence of the hole. Low stress level tests (300 MPa and below); however, did not display any crack bifurcation nor any of the tiny, discontinuous cracks.

Johnson et al (3:23) noticed that at room temperature and a 200 MPa stress level, cracks initiated in [0/90], in a manner similar to the high stress, elevated temperature tests. However, 20,000 cycles after initiation, more cracks initiated in the strip of material between the hole and the specimen edge as well as from the hole periphery. Newaz and Majumdar (27:16) saw a similar behavior for the unidirectional ply lay-up.

Formation of these tiny, discontinuous cracks is dependent upon the ductility of the material. Low stress, high temperature tests exposed the composite to high temperature for long periods which caused additional heat treatment that led to formation of a more ductile matrix. Specimens involved in room temperature tests at any stress level along with the high stress tests at high temperature were less ductile and hence formed these tiny, discontinuous cracks.

Fractographic Evaluation. The first step in performing fractographic analysis involves noting the color, amount of

fiber pull-out, and general fracture surface appearance. Examination of the fracture surface color reveals, qualitatively, the amount of time the fracture (at that point) was exposed to air and high temperature. At high temperature the air and titanium react to form an oxide layer which changes color as the exposure time increases. A bright shiny appearance indicates a very short exposure time to air and elevated temperatures. The color becomes brownish-yellow, takes on a straw color, progresses to various shades of blue, then to purple. By noting the color of different regions of the fracture surface, crack history may be determined (see figure 22).

Another aspect to observe during initial inspection is the degree of fiber pull-out. This, when taken in conjunction with microscopic analysis, will help indicate how the specimen failed. For example, low fiber pull-out and ductile dimpling of the matrix is indicative of fiber failure prior to matrix failure. This results in a relatively flat fracture appearance (i.e. the fiber breaks at the main fracture surface).

Figure 23 shows specimens one through four (left to right). Specimen one was monotonically loaded to failure at 427°C. Note in figure 24 that the fracture surface of specimen one is located 90° from the loading axis. The fracture surface was flat with little fiber pull-out and a

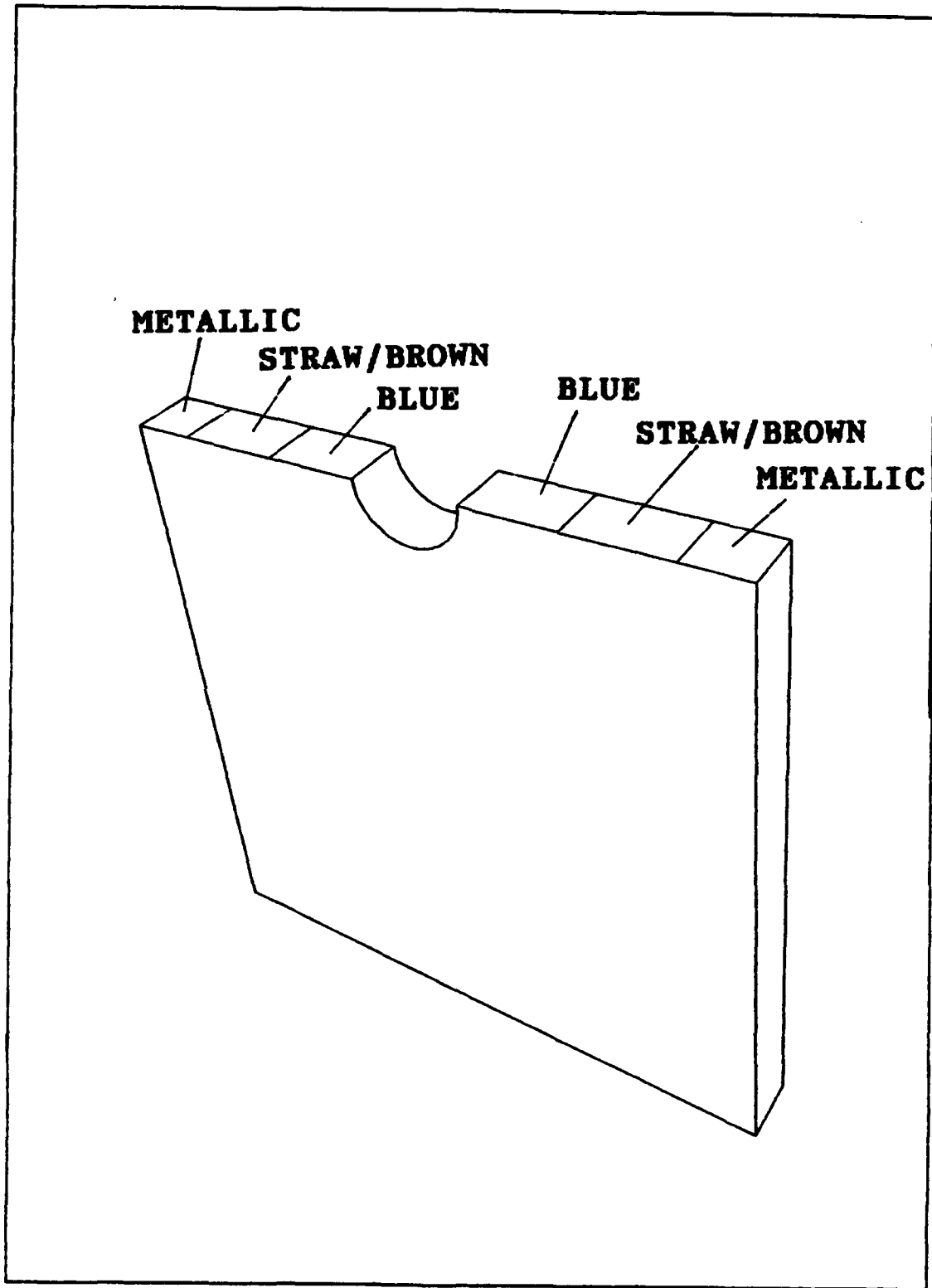


Figure 22: Typical Fracture Surface Coloration

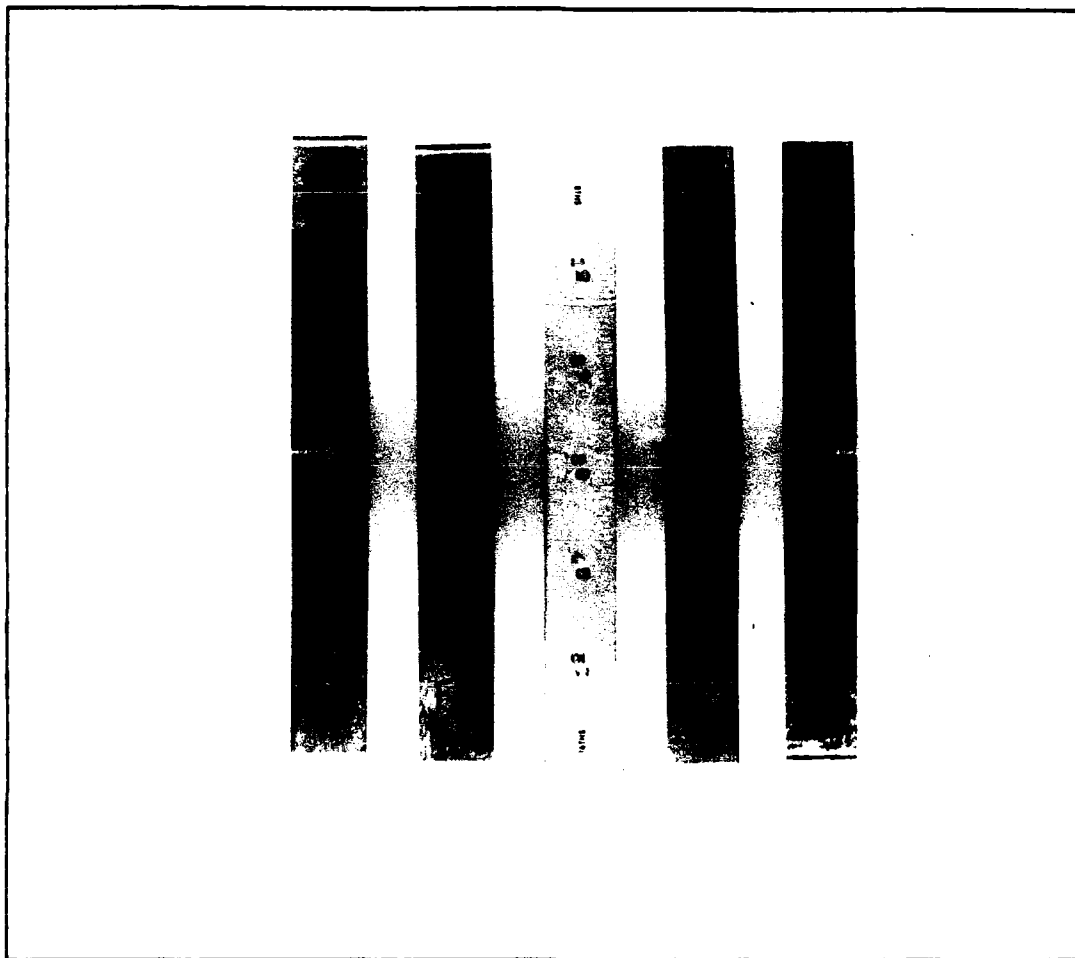


Figure 23: Specimens 1 through 4 (left to right)

bright, shiny appearance uniformly over the cross-section. Microscopic analysis revealed wide spread ductile failure of the matrix (as shown later). Fiber failure leading to tensile overload of the matrix caused this specimen's failure.

All of the fatigued specimens had the same general fracture surface appearance which is different from that of the monotonically loaded specimen (see figure 25). First, note that there exists a large amount of fiber pull-out. The color distribution was as shown in figure 22 above. Bright

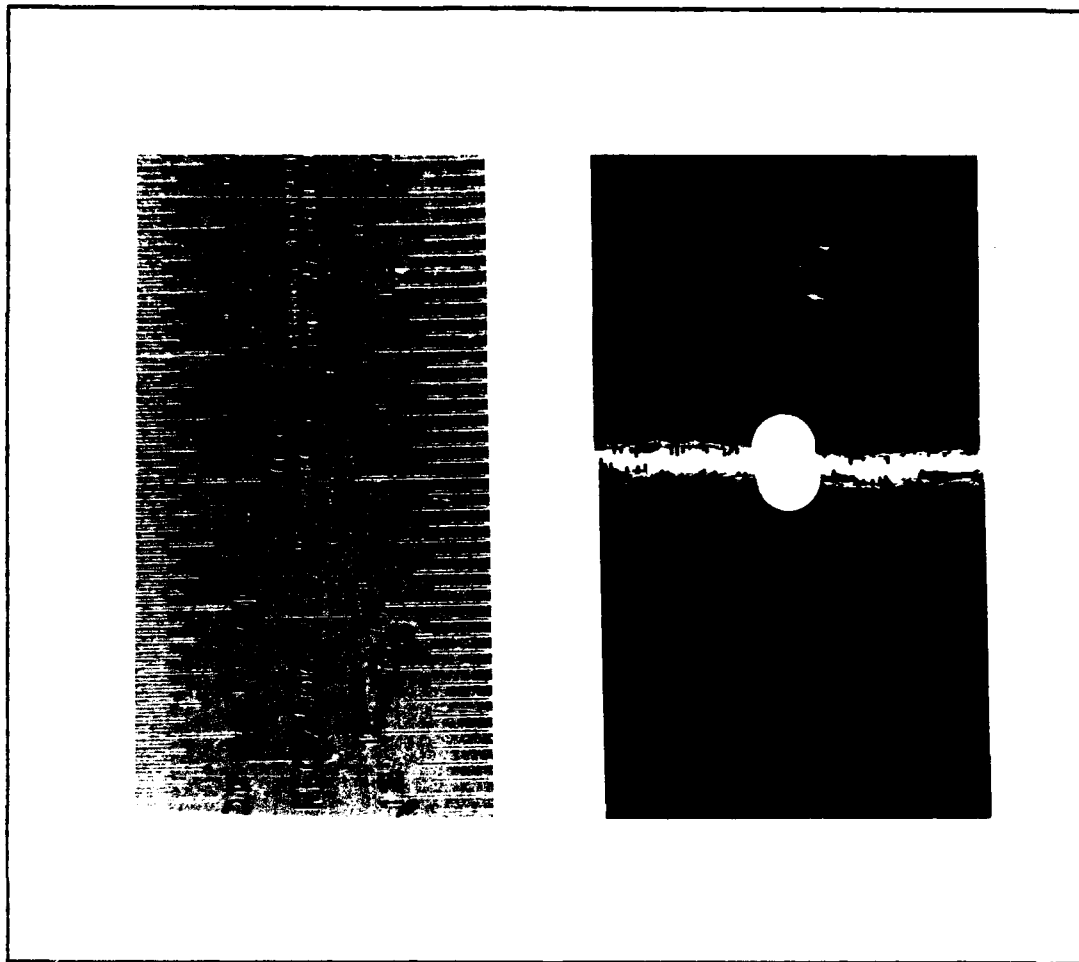


Figure 24: Monotonically Loaded Specimen Fracture Surface

blue color near the hole indicates that the crack initiated at the hole and was subsequently subjected to air and high temperature for a longer period of time. The bright metallic color shows where the crack reached a critical length at which time the specimen failed due to tensile overload. Microscopic evaluation revealed that cracking at the hole was primarily brittle cleavage in nature (see figure 26) while the fracture at the specimen edge was characterized by ductile dimpling (see figure 27 top photo). This failure surface is similar to

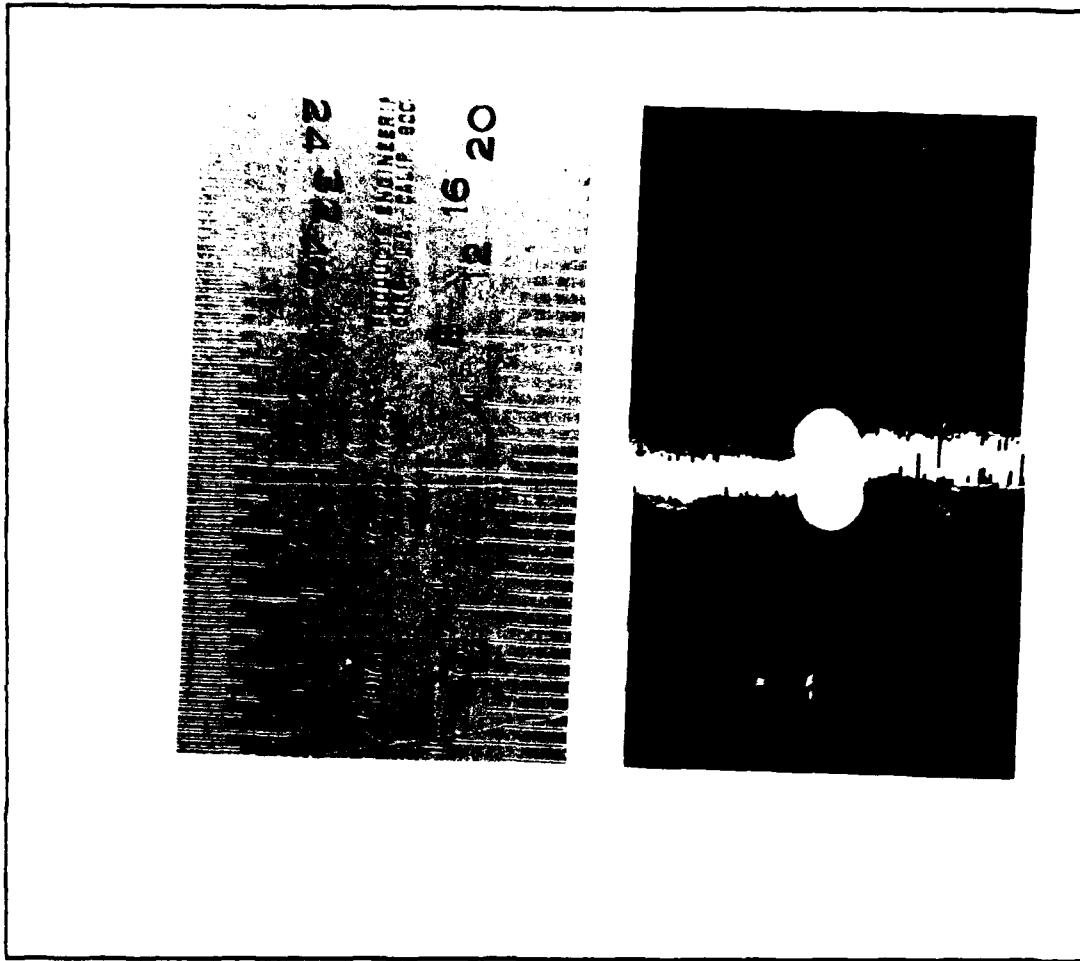


Figure 25: Fatigue Loaded Specimen Fracture Surface

that of the monotonic tension test shown in bottom photo of figure 27. The transition point from brittle cleavage fracture to ductile fracture is dependent upon the stress level. A critical crack length can be defined as the length from the hole periphery to the brittle/ductile transition as shown in figure 28. As the crack grows, the area available to carry the load reduces to a point where the stress in the cross-section approaches the composite's ultimate strength. A method for predicting the critical crack length is presented

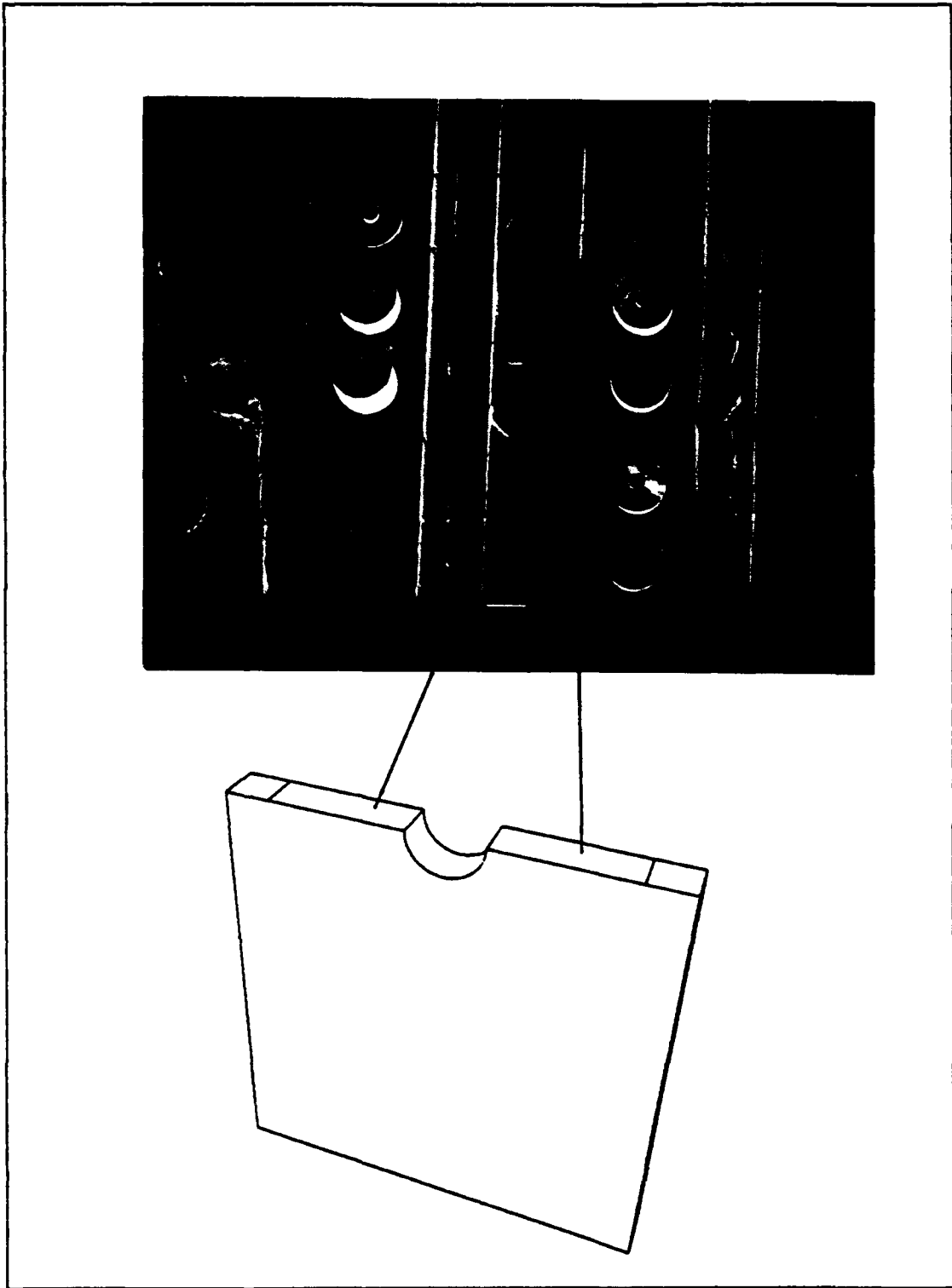


Figure 26: Fracture Surface of a Fatigued Specimen (at the hole)

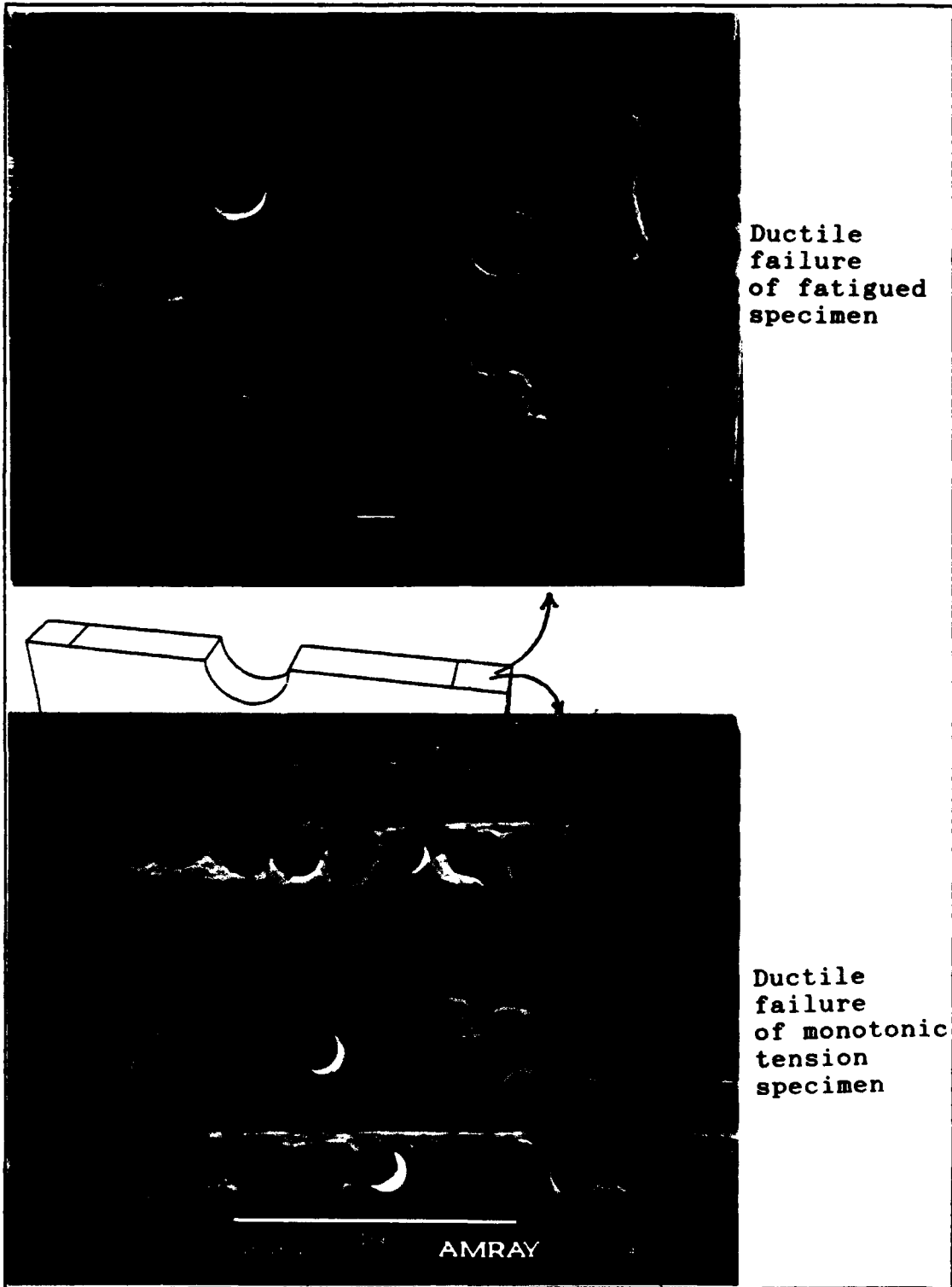


Figure 27: Fracture Surface of a Fatigued Specimen (at the edge)

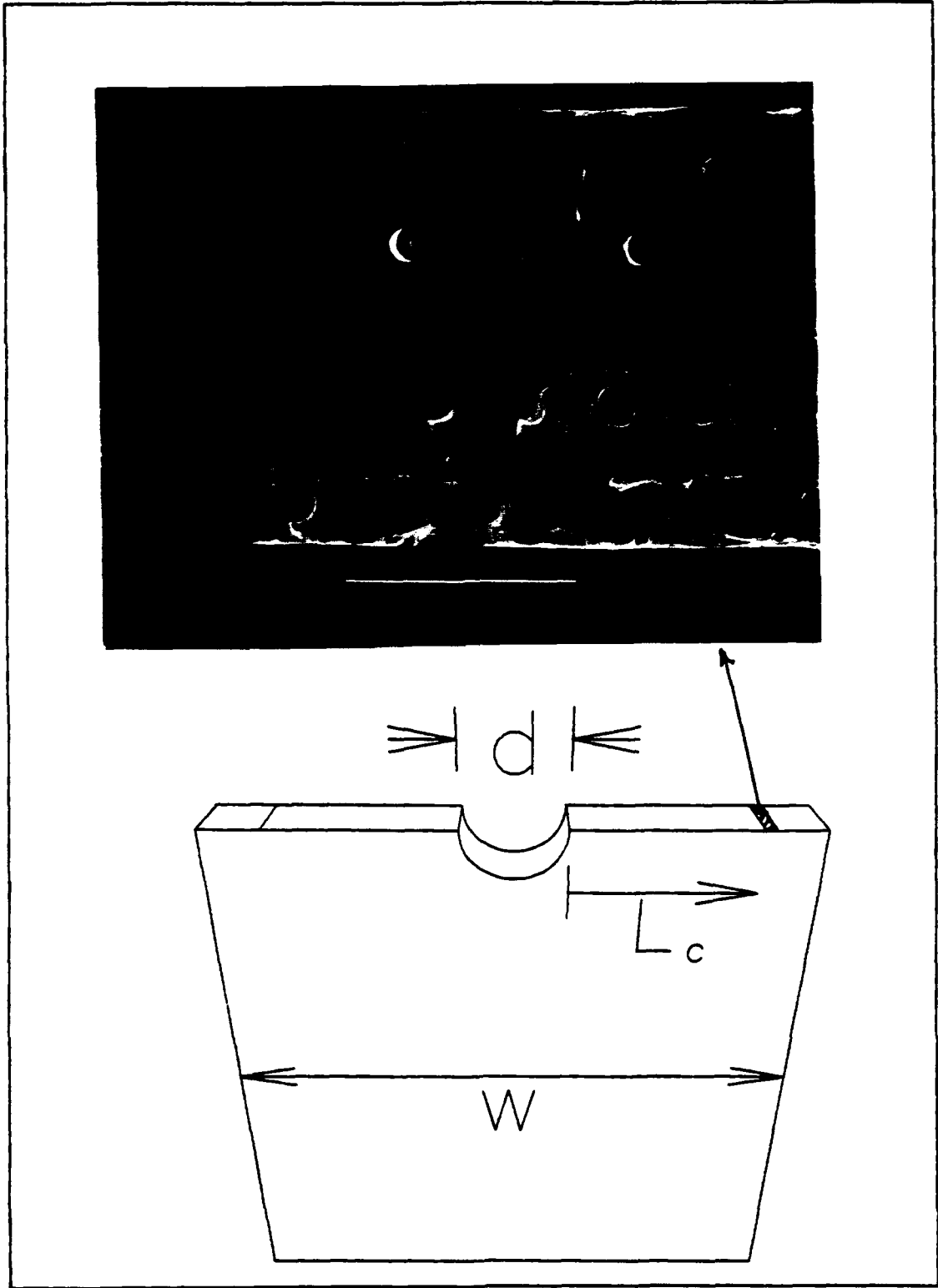


Figure 28: Ductile to Brittle Transition

in the section entitled *Quantitative Analysis*.

Examining the inside of the hole, reveals cracks on the front and back faces which penetrate into the specimen. Figure 29 shows that the crack opening is greater on the faces than in the center of the specimen. This indicates that the damage starts on the face due to high shear stresses, then progress inward until the front and back cracks coalesce in the center of the specimen (in the thickness direction). It appears that the once the front and back cracks join in the center, they form through the thickness cracks which then grow toward the specimen's edge. Notice that the cracks move around the fibers without fracturing them. This behavior is typical of the specimens examined.

Matrix plasticity in the form of necking around and between fibers was noted in the ductile region of each specimen. In contrast, the brittle region showed very little matrix plasticity. Note in the photo of figure 28, the brittle surface is in the center of the specimen thickness while the ductile surface is on the face of the specimen. This indicates that, at this point prior to failure, the fatigue crack had a parabolic shape as shown in figure 30. Which means that the brittle fatigue crack front was propagating internal to the specimen ahead of the face crack immediately prior to failure.

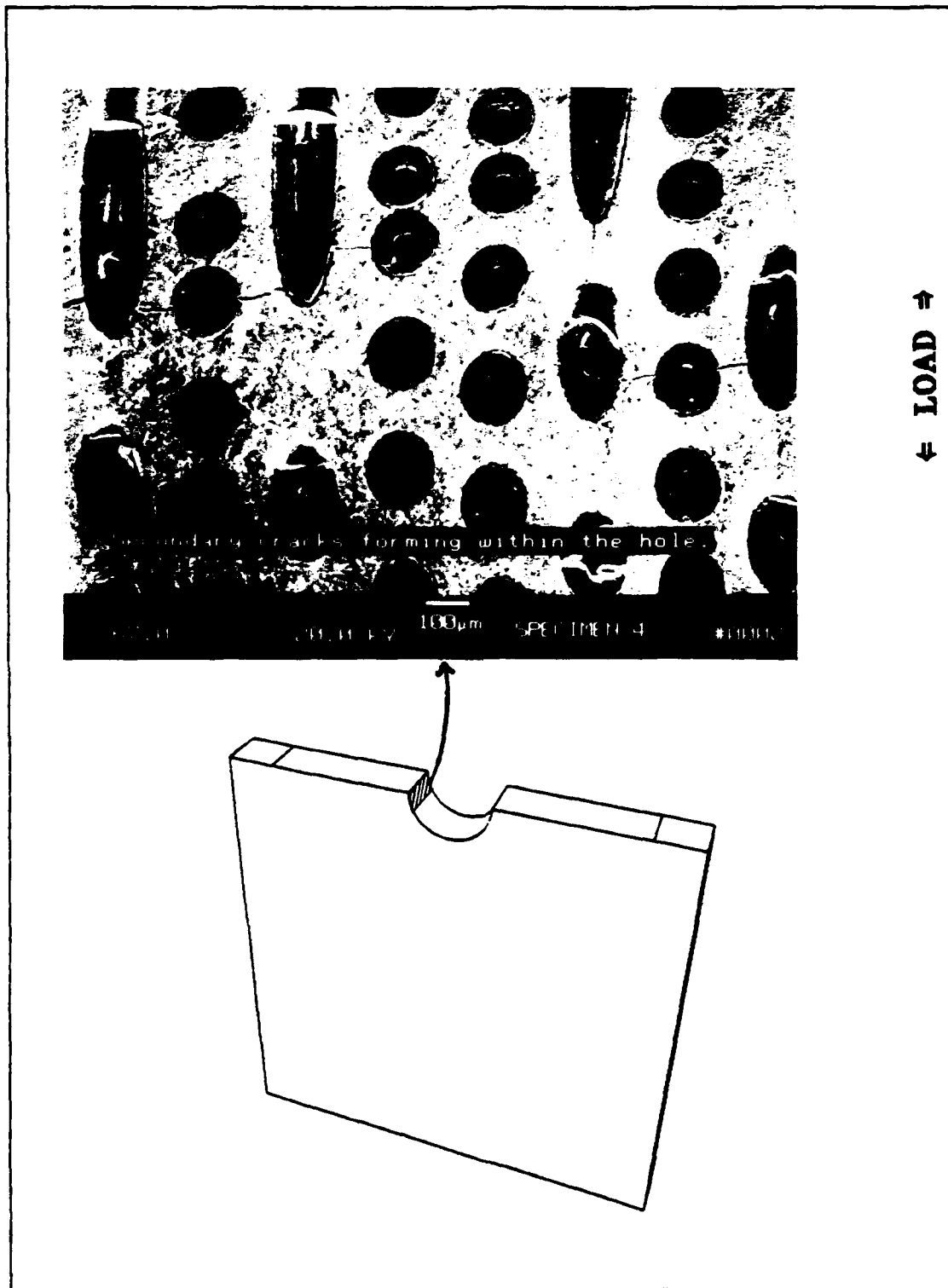


Figure 29: Minor Cracks Progressing into the Specimen (specimen face on the left and right edges of the photo)

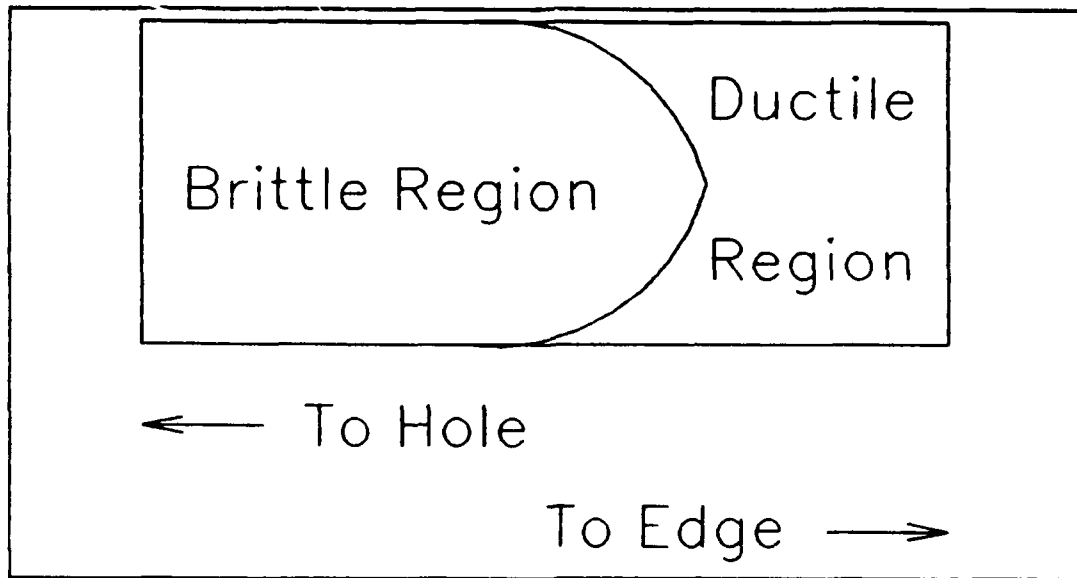


Figure 30: Fatigue Crack Shape Prior to Failure

In all specimens, the fracture surface followed one set of 90° fibers from the hole to the specimen edge (see figures 23 and 24 above). This indicates that the cracks progressed along the debonded fibers and not through any weaknesses in the matrix. In many cases the outer carbon coating had fractured or separated from the fiber. In some rare cases, the 90° fiber fractured, usually at the juncture of a molybdenum cross-weave.

Metallographic Evaluation. Fractographic analysis evaluates the actual fracture surface which gives information about the point of failure, but then questions arise about what happens in the material a short distance from the fracture. Answers to these questions are often resolved through metallographic analysis. Each specimen was sectioned according to figure 7 in chapter 3. Care was taken to not

induce any additional damage during the sectioning and mounting procedure.

Figure 31 shows debonding of 90° fibers directly below the hole indicating that debonding runs along the entire fiber's length. Very little matrix cracking was noticed in



Figure 31: 90° Fiber Debonding Below the Fracture Surface, Inside the Specimen

the transverse direction of all specimens examined. This is shown in the top picture of figure 33 where the crack at the top of the photo is 200 microns below the main fracture surface. It is possible that the crack started at the 0° fiber, proceeded to the 90° fibers. Since the fiber has

debonded, the crack moved around the fiber rather than penetrating it. The bottom picture shows transverse cracking 1.36 mm below the fracture surface. This is the minor crack progressing toward the edge of the specimen with a parabolic crack front. Even when 0° fibers are encountered by transverse cracks, the fibers debond without fiber fracture (see figure 32) thereby permitting fiber bridging. Fiber

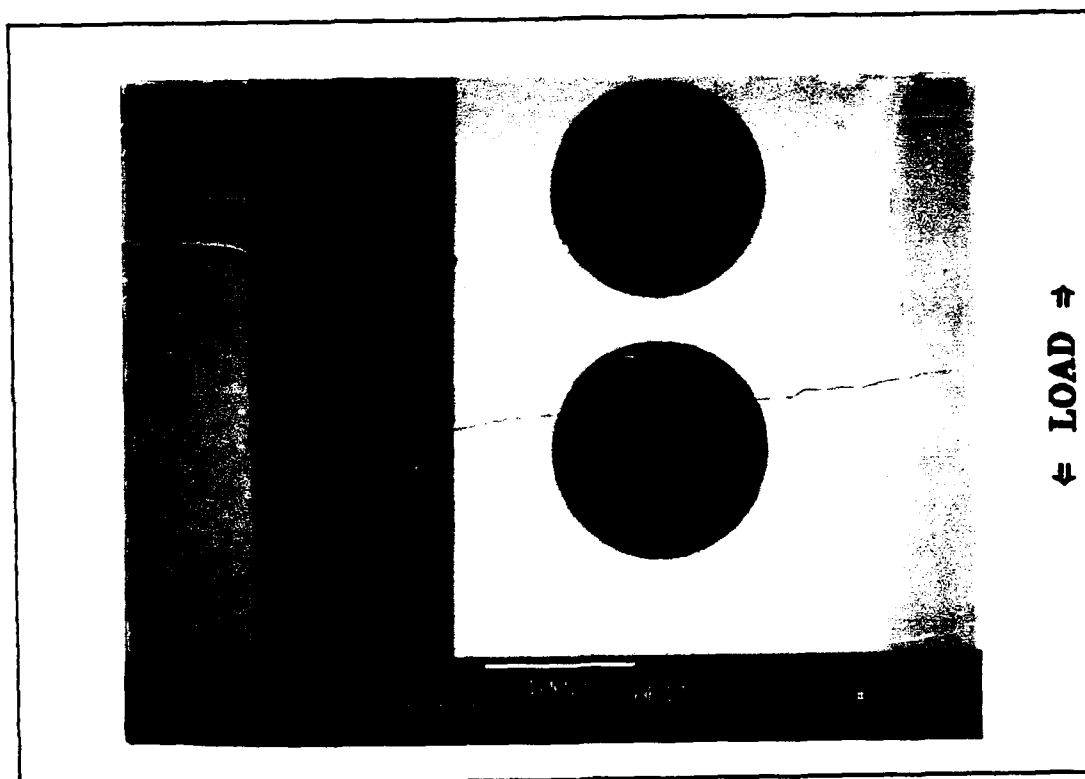


Figure 32: Transverse Crack Propagation Past a 0° Fiber

bridging is a condition in which fibers do not break at the fracture surface. Instead, they span the crack and continue to carry load.

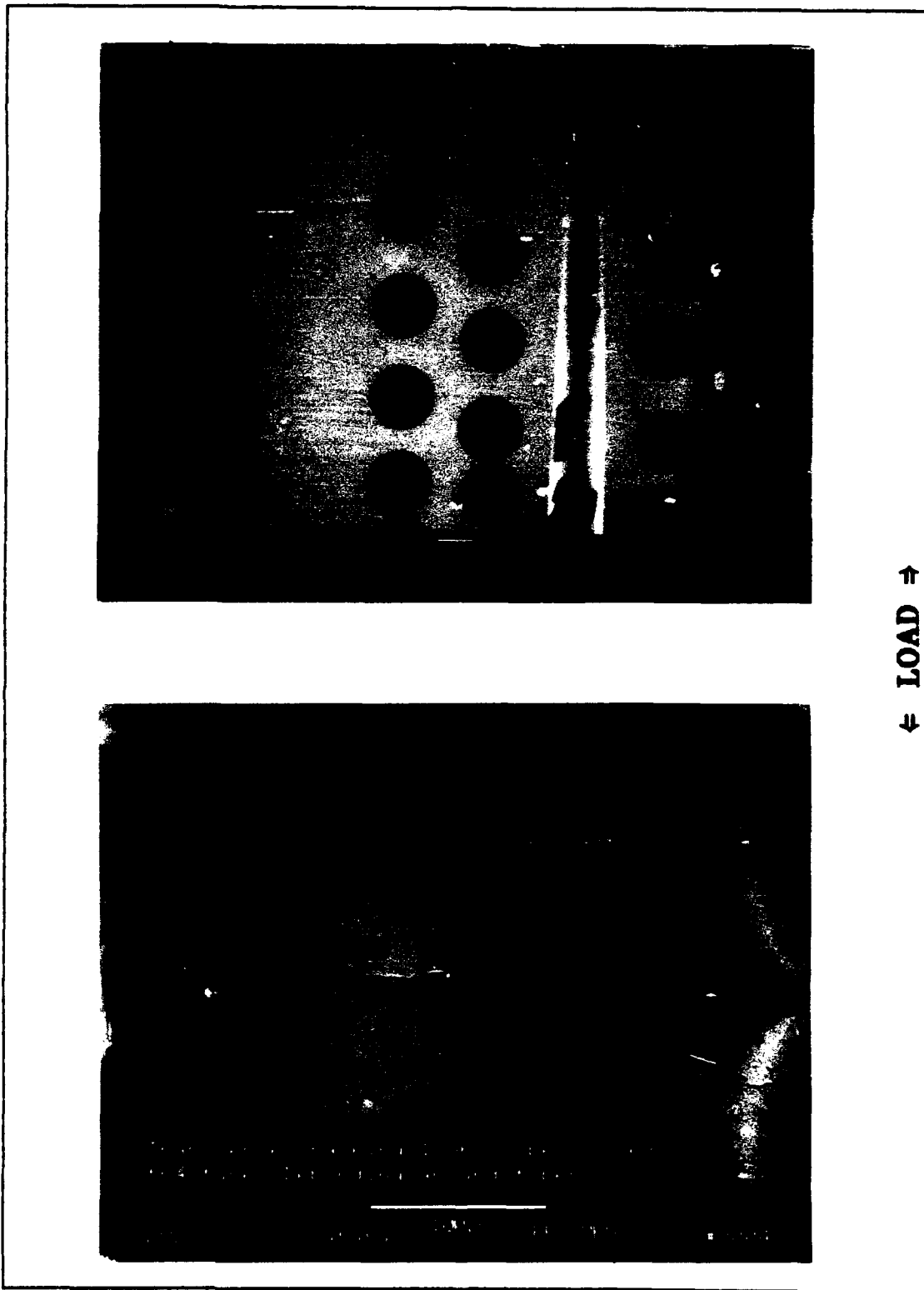


Figure 33: Transverse Cracking within the Specimen

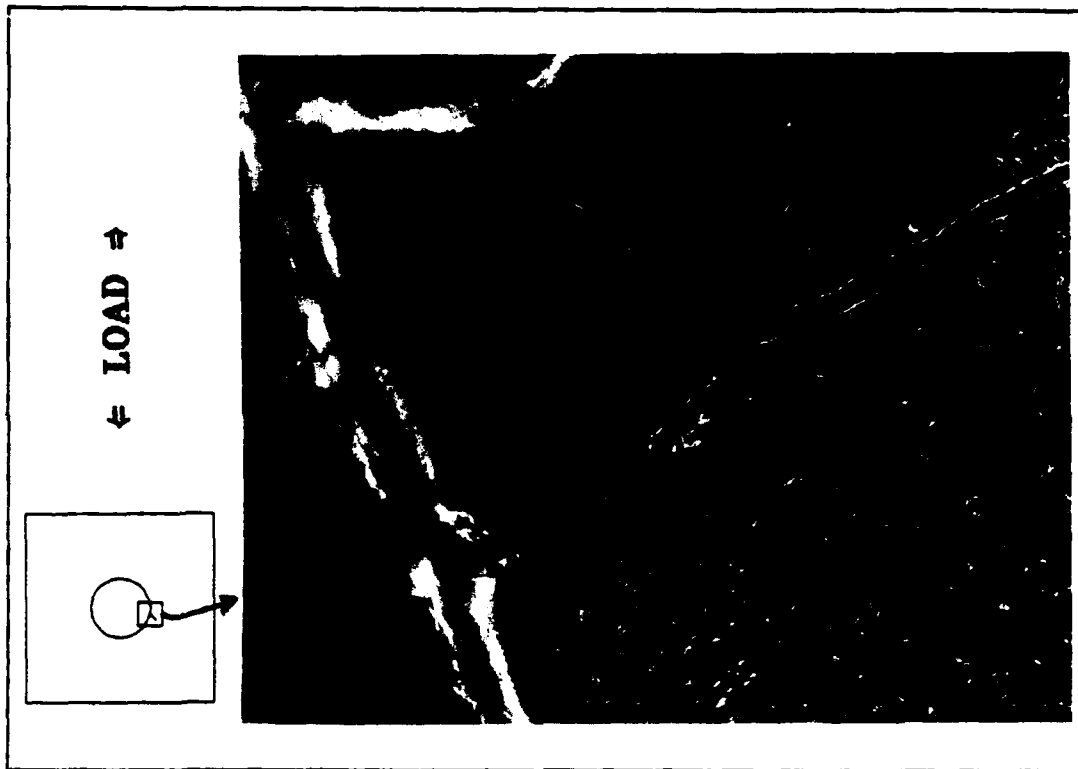


Figure 34: Transgranular Cleavage of Initial Crack

To understand how the cracks grew from the hole to the edge, the face of one specimen was etched to reveal slip bands while two other specimens were polished down to the first set of fibers to reveal damage progression below the outer layer of matrix material. Inspection of the etched specimen did not uncover the presence of slipbands; however, grain boundaries became very clear revealing that the initial face crack did not follow grain boundaries, rather it exhibited transgranular cleavage behavior (see figure 34).

The specimens electro-polished down to the first set of fibers revealed longitudinal and transverse cracking of the outer carbon coating of the 0° fibers as the minor crack

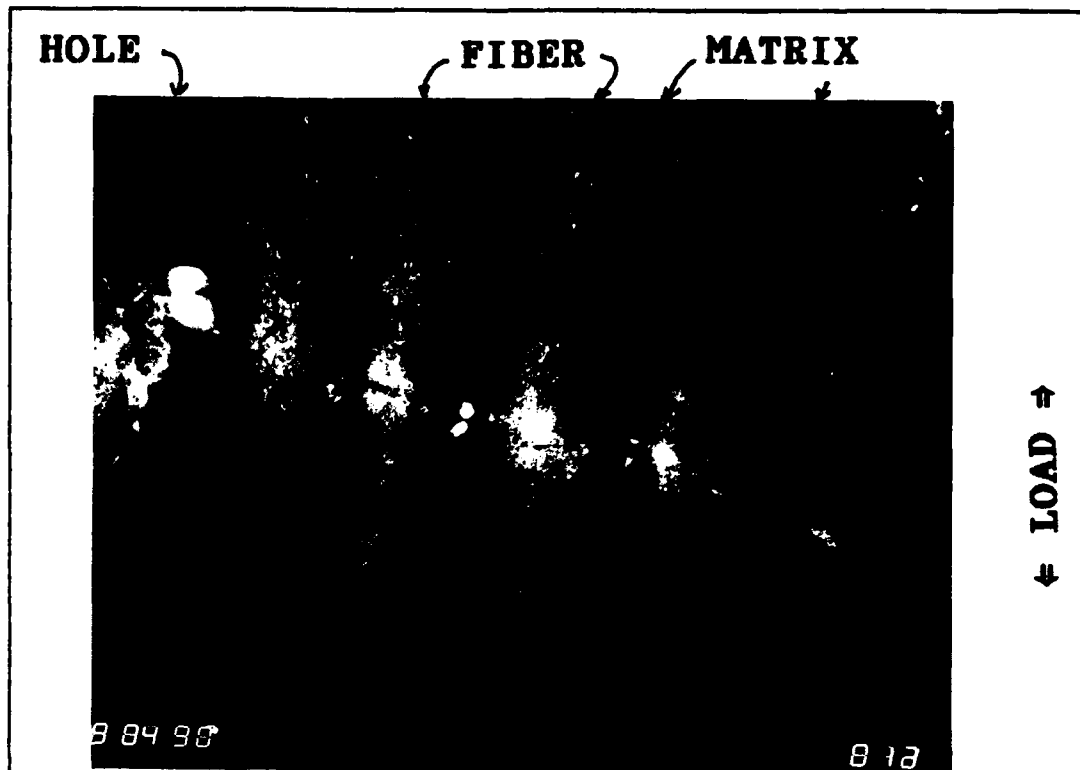


Figure 35: Longitudinal and Transverse Cracking of the Outer Carbon Coating of 0° Fibers.

continued to grow through the matrix. Polarized light was used to show this characteristic in figure 35. The light regions running from the top to the bottom of the picture are the 0° fibers and the dark areas are the matrix material. Notice how the major crack continues to move toward the edge of the specimen while longitudinal cracks proceed up the outer casing of the fiber. This leads to the occasional transverse crack found within the matrix. The same region viewed with ordinary bright field illumination (figure 36) shows the crack passing the fiber, but does not reveal the true nature of the cracking mechanism. At this point the main part of the fiber

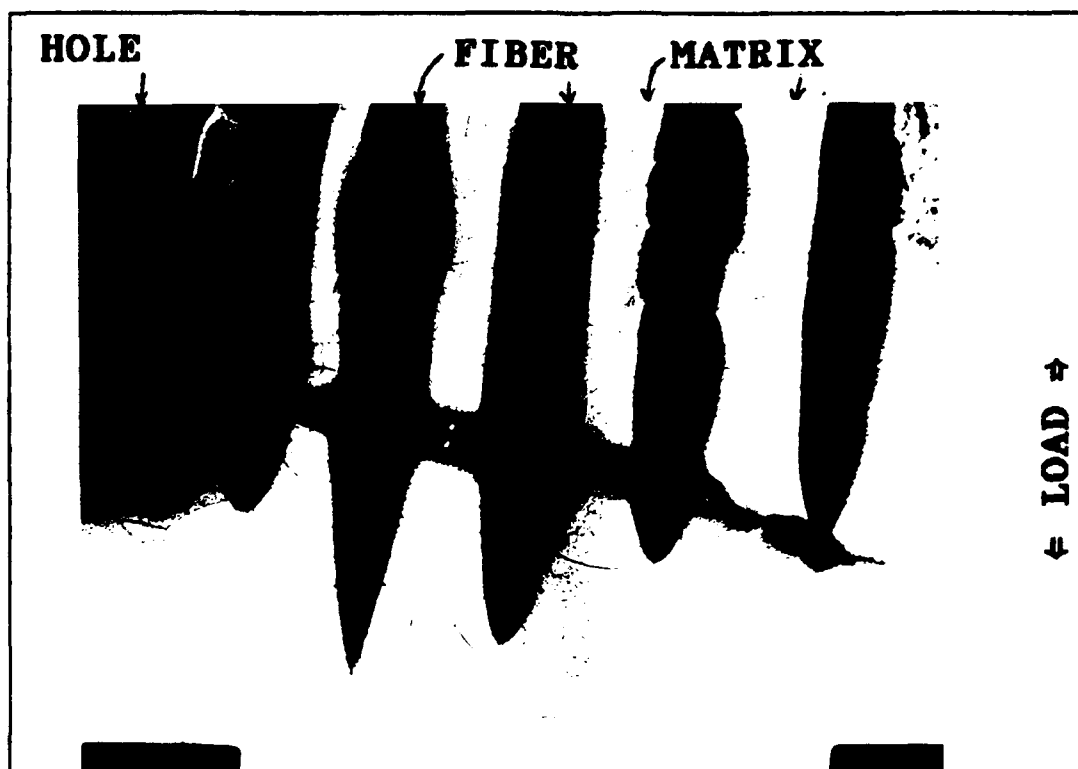


Figure 36: Bright Field Illumination of Fiber Bridging

may or may not be fractured, further polishing was required.

Figure 37 shows 0° fibers (dark vertical stripes) bridging one of the minor matrix cracks. To verify that the same event was occurring with the major cracks, test eight was terminated following the establishment of two dominant cracks. Specimen eight was then polished down to the first set of fibers. Fiber bridging for both the major and minor crack are shown in figure 38, 39, and 40. Upon closer examination of one of the matrix cracks, matrix yielding is observed (see figure 41). Note how the fiber/matrix interface is broken down and the matrix material is pulling away from the outer carbon coating of the fiber.

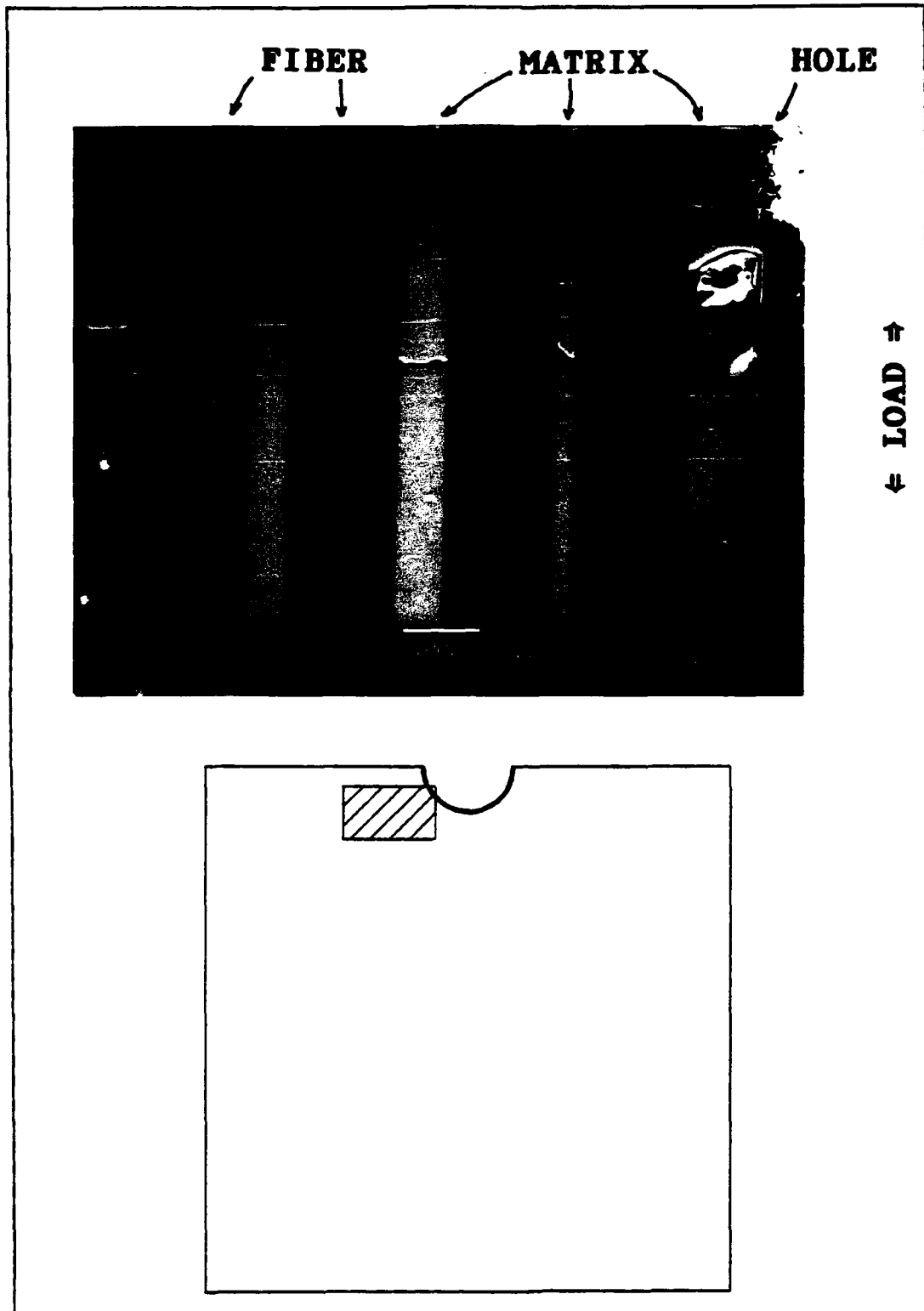


Figure 37: Fiber Bridging Minor Matrix Crack

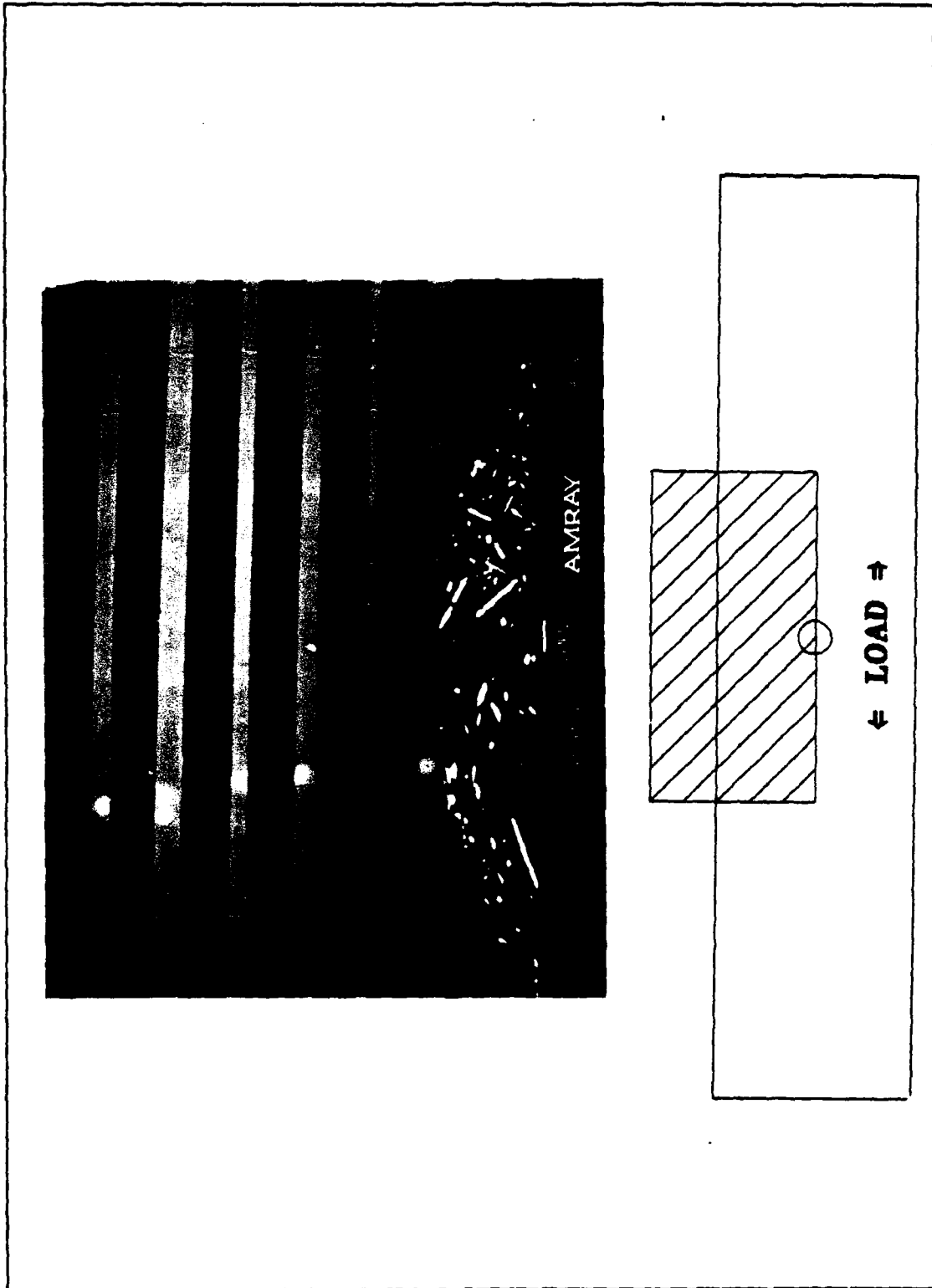


Figure 38: Fiber Bridging of Major and Minor Cracks

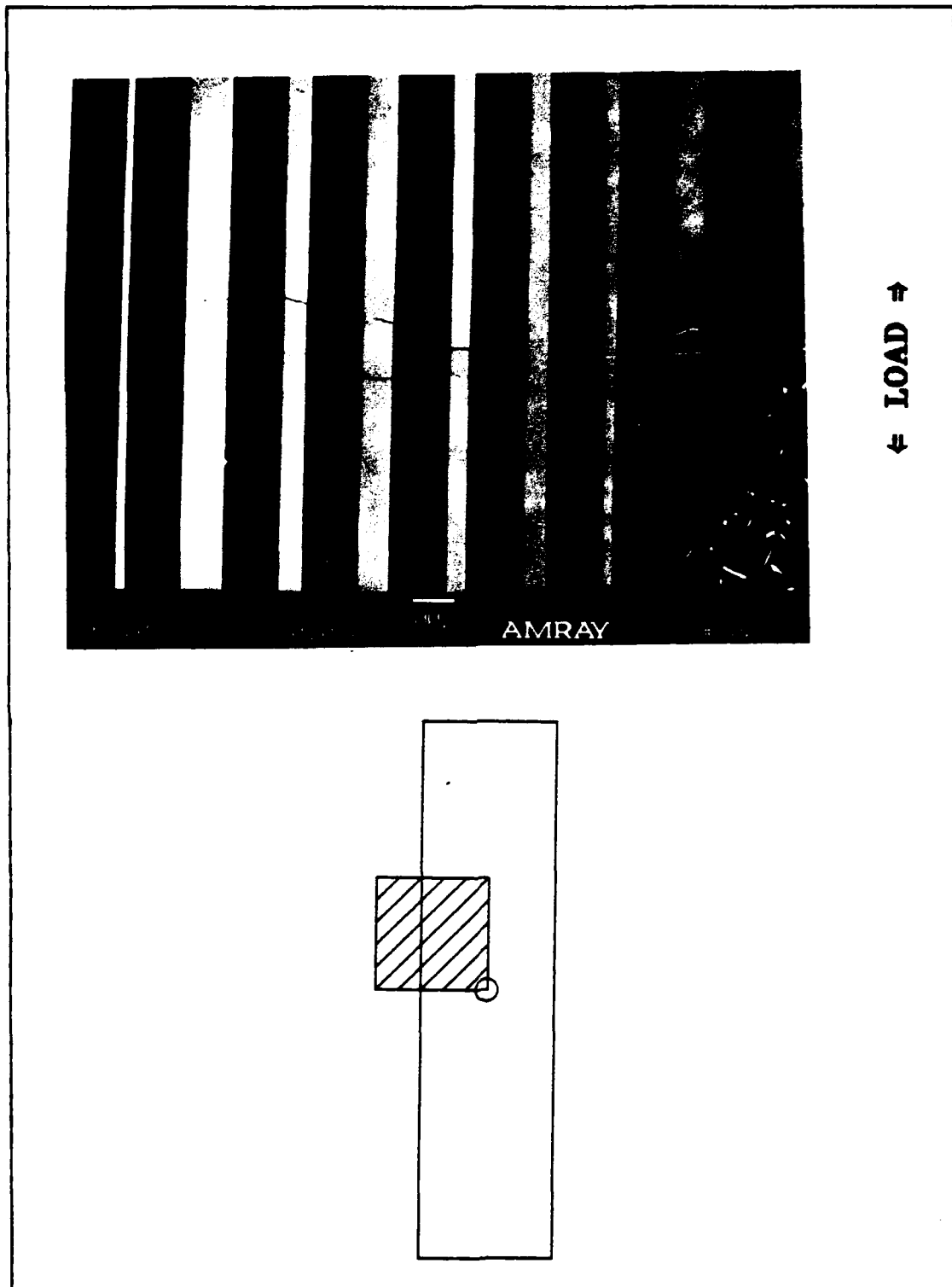


Figure 39: Magnified View of Fiber Bridging of Major Crack (top left crack)

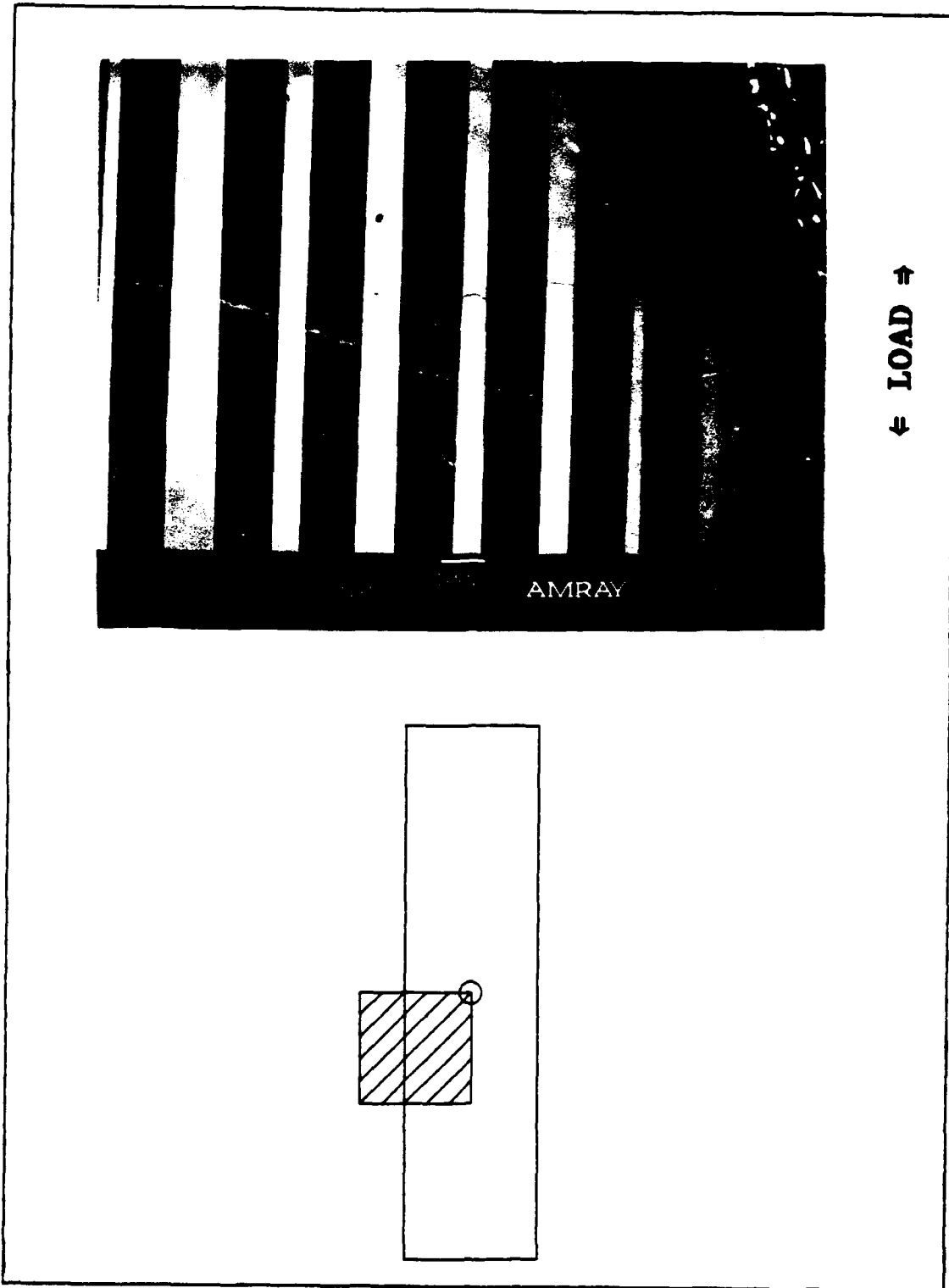


Figure 40: Magnified View of Fiber Bridging of Minor Crack (bottom left crack)

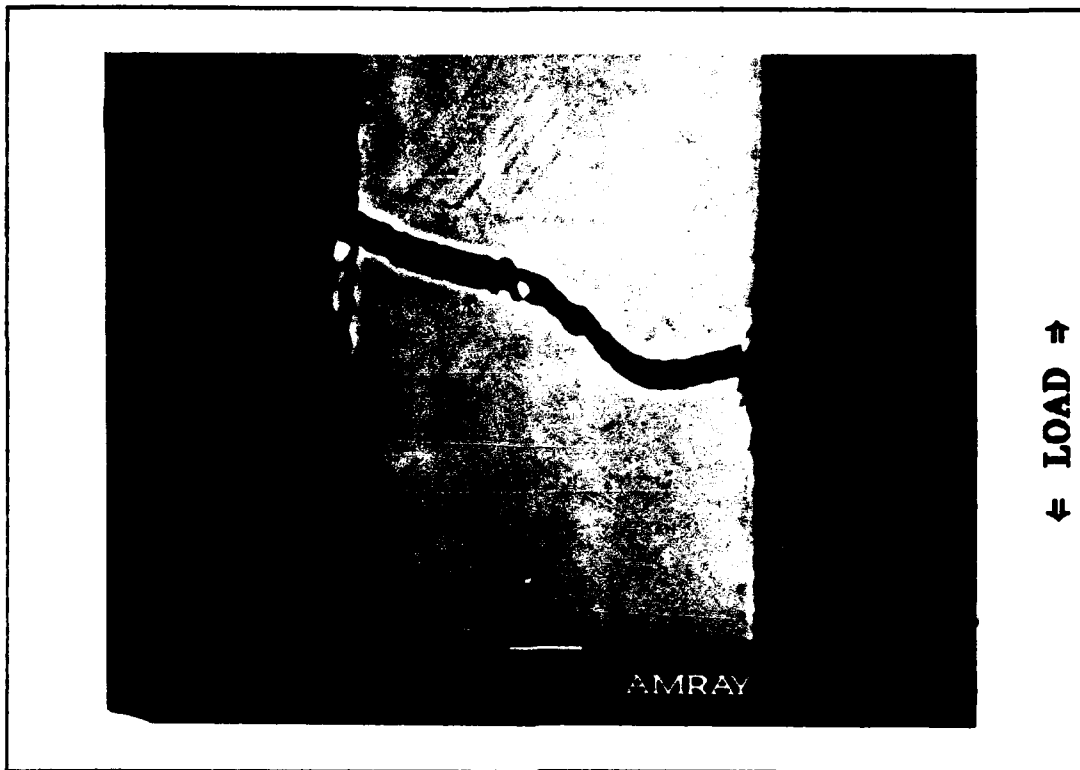


Figure 41: Matrix Yielding Between 0° Fibers Near the Hole

Crack Growth Analysis. Once carbon coated face replicas were examined via SEM, the crack lengths were measured to within 3 microns. Figure 42 shows crack progression for the front and back faces of a typical low stress (300 MPa and below) specimen. Likewise, figure 43 shows the crack progression for a typical high stress (400 MPa and above) specimen. In these figures, references to the crack position are relative to the way an observer would see the specimen face when looking at it.

It appears that when a typical crack initiates, it grows rapidly until the elastic strain energy is dissipated either totally or partially. When this energy is totally dissipated,

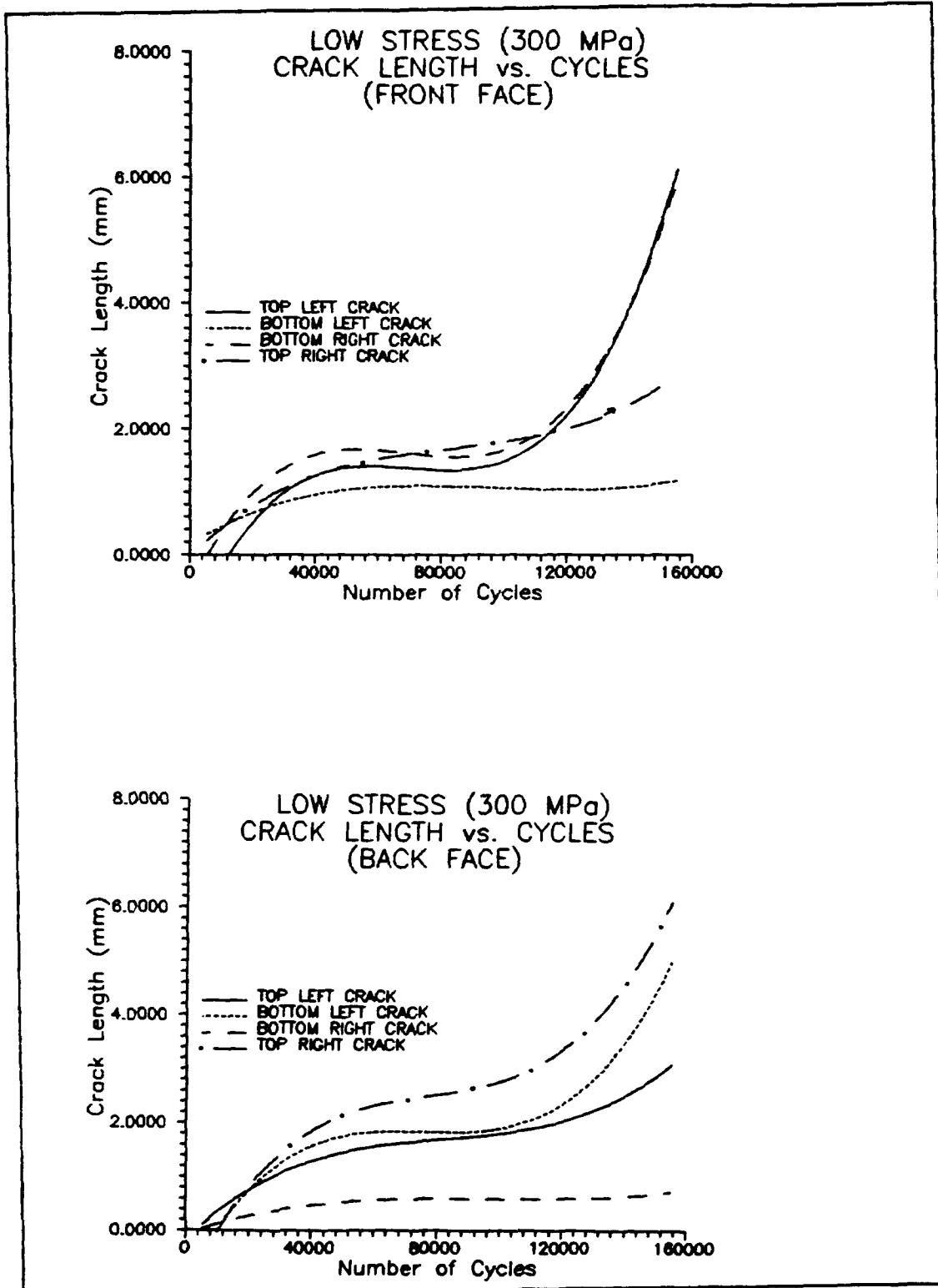


Figure 42: Low Stress Level Crack Length vs. Cycles

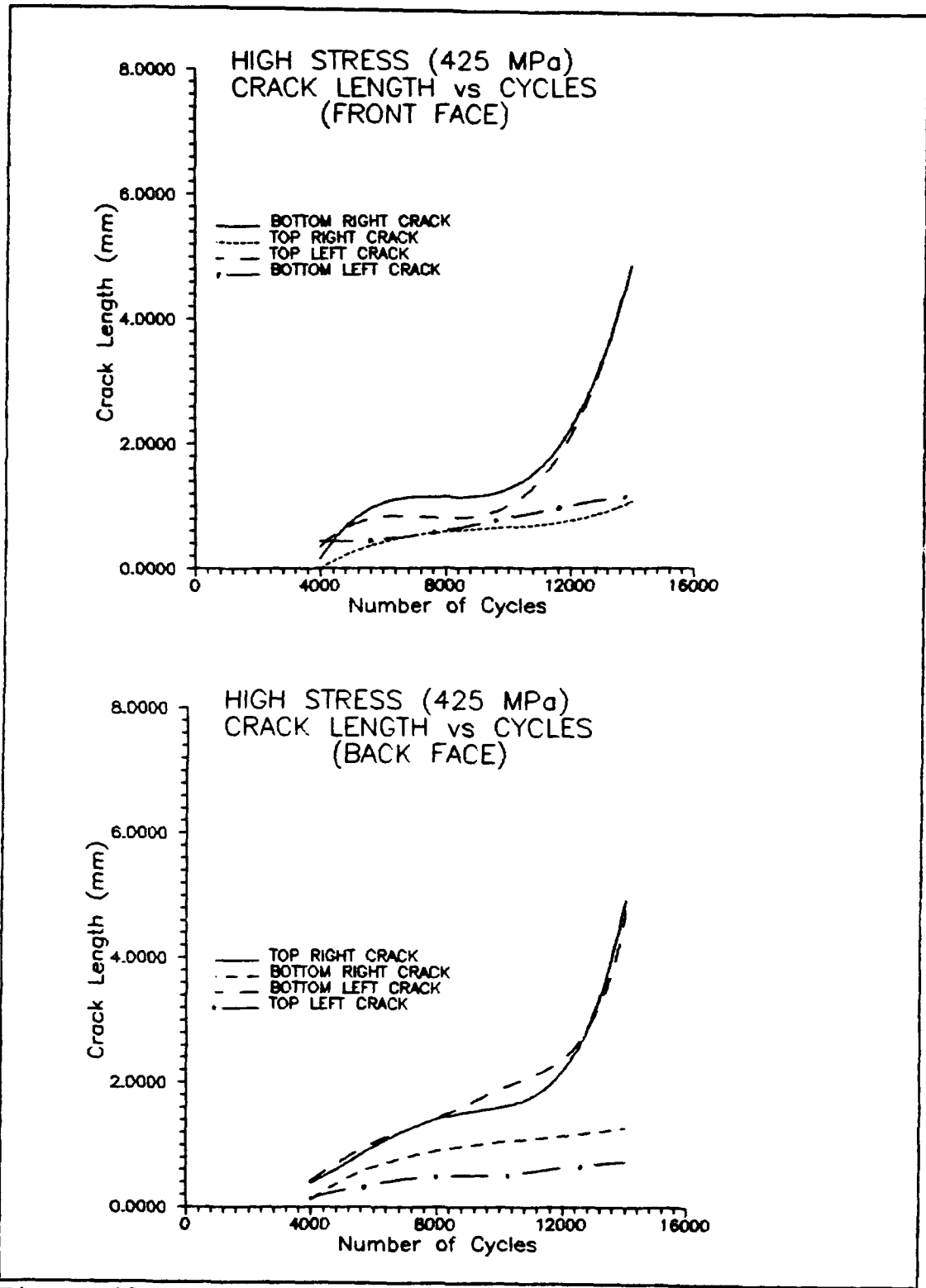


Figure 43: High Stress Level Crack Length vs. Cycles

the crack growth then levels off at this point. If the energy is not completely used up the cracks will continue to grow at a greatly diminished rate. As the crack continues to grow, the amount of load bearing surface area is reduced causing the stress to approach the ultimate strength of the composite. By this time the elastic strain energy has again increased thus leading to increased crack growth rate. When the crack reaches the critical crack length, rapid unstable crack growth occurs. Looking at the two major cracks on any of these figures, note that in most cases dominance is established soon after the crack initiates. The minor cracks do not usually cease growing, but generally grow at a slower rate than the major cracks. In both cases presented, the top left crack and the bottom right crack became the major cracks. This is purely coincidental, the specimens tested did not exhibit any particular pattern as far as which cracks became dominant.

To understand how crack initiation interacts with strain and modulus, figure 44 displays modulus, strain, and crack growth data simultaneously. Note that the modulus dips down at the point of initiation, strain increases, and crack growth rate increases simultaneously. Strain then increases rapidly as the critical crack length is reached.

Johnson et al (3:24) determined a total crack length based on the summation of all cracks formed between the hole and specimen edge on one half of the specimen's front face.

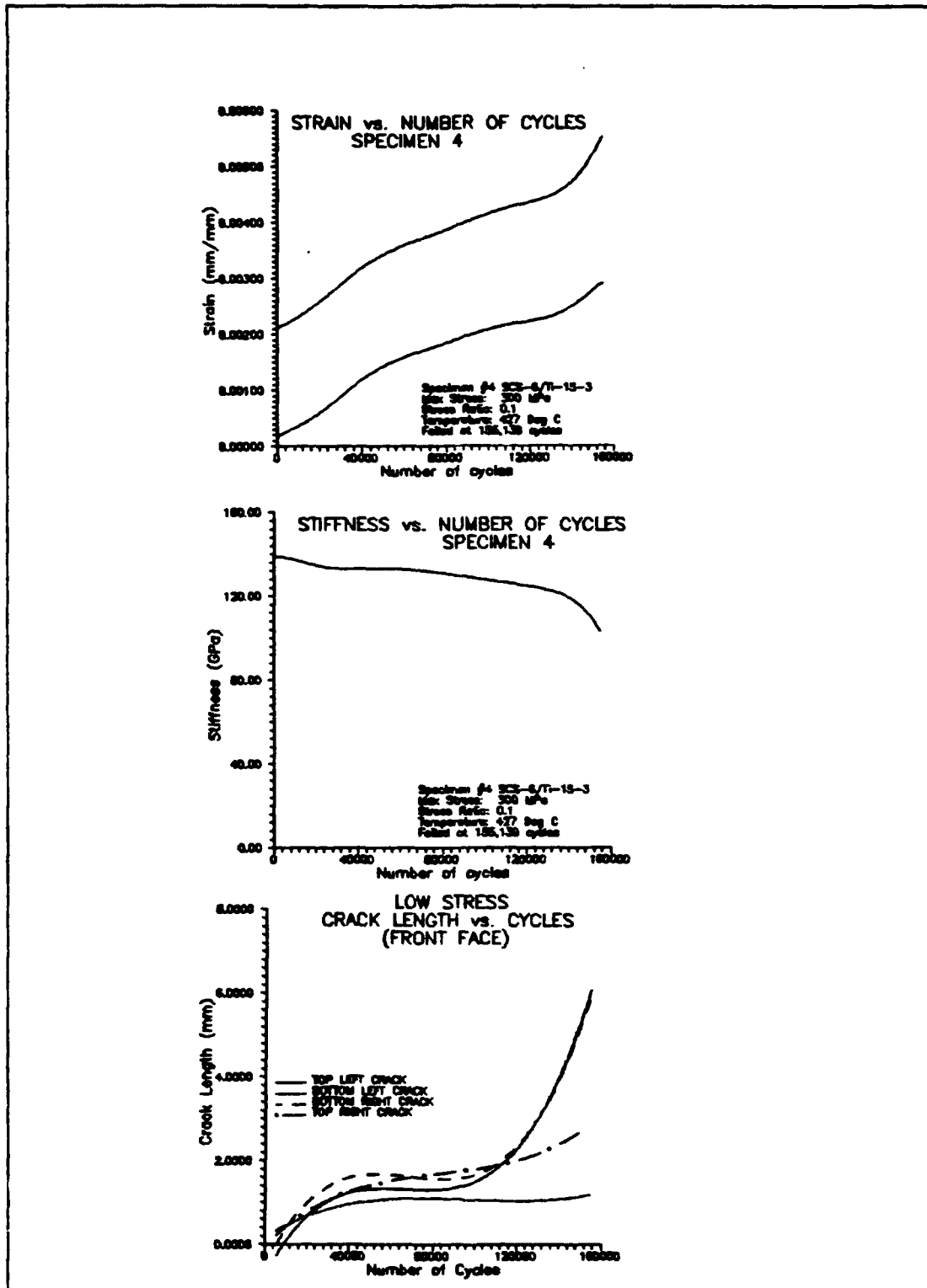


Figure 44: Strain, Modulus, and Crack Growth Comparison

This was done to provide a measure of the damage sustained due to ambient temperature fatigue. A similar summation was performed for elevated temperature and is shown in figure 45. Note that the total crack length at ambient temperature shoots up drastically soon after initiation. This is due to the formation of the tiny, discontinuous cracks as noted in the *metallographic analysis* section for the 425 MPa test at 427°C. Because the high temperature specimens do not form these small cracks, the total crack length will be much shorter than those of the ambient tests. For each temperature condition, the total crack length grows faster and longer at the higher load levels as expected.

Quantitative Analysis

Once experimental observations have been collected, a quantifiable accounting of the events witnessed needs to be performed so that accurate predictions of future events may be made. Two such prediction methods are considered here. The first is a technique for estimating the critical crack length for a composite specimen with a center hole. The second technique examined, involved predicting the number of cycles to damage initiation.

Critical Crack Length. A simple Strength of Materials

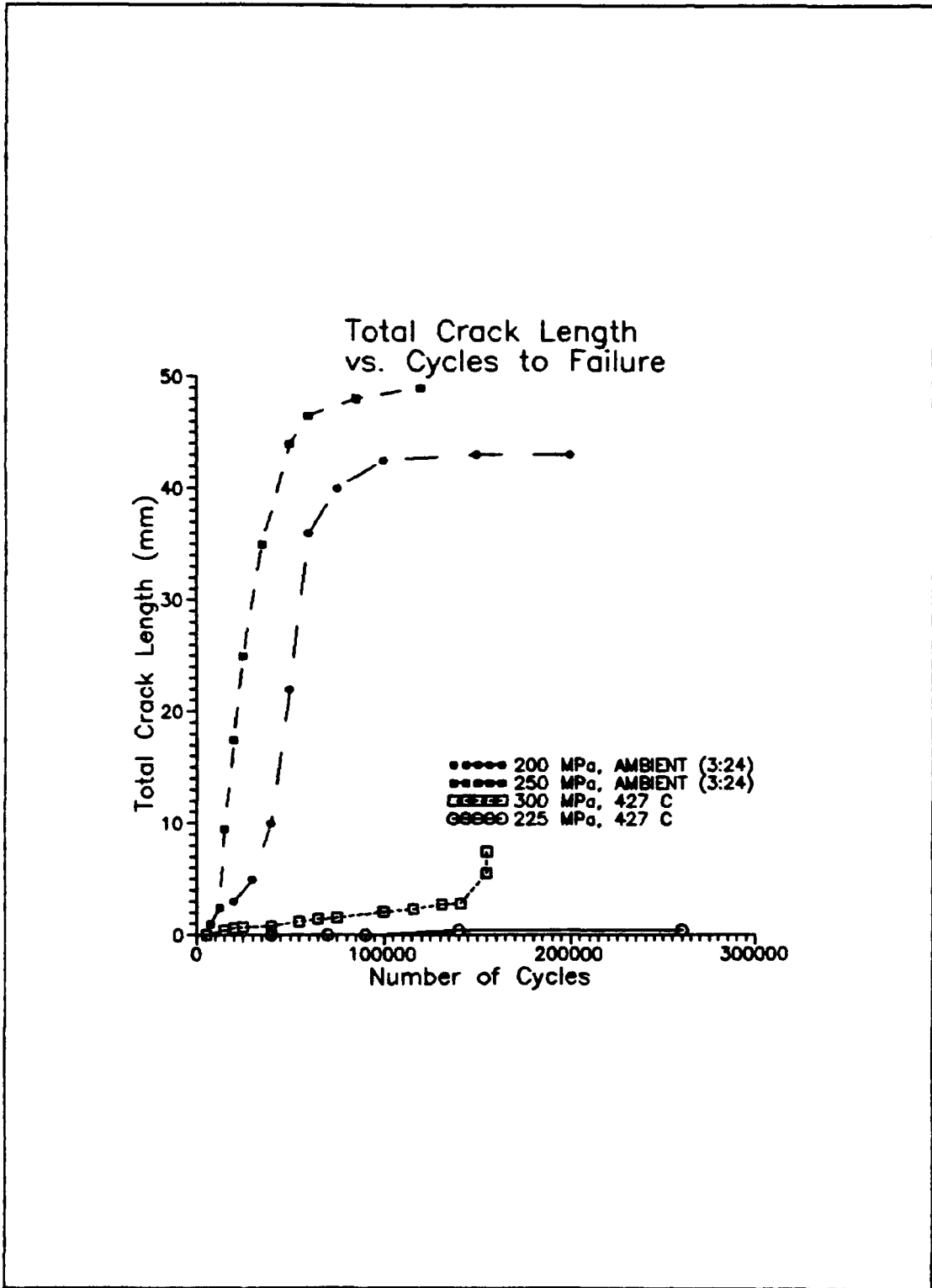


Figure 45: Total Crack Length Comparison

approach was used to develop a model for the critical crack length, L_c , is:

$$L_c = \frac{(w-d) \left(1 - \frac{\sigma_{test}}{\sigma_{ult}}\right)}{2(1-\beta V_f)} \quad (1)$$

where w is the specimen width, d is the hole diameter, σ_{test} is the stress level of the test in progress, σ_{ult} is the material ultimate strength, β is the percentage of fibers bridging the crack, and V_f is the fiber volume fraction. Derivation of this formulation is located in appendix 4. Theoretical and experimental critical crack lengths are plotted against stress level in figure 46. Note that the actual crack length differs from the predicted crack length because fibers behind the crack front are bridging the fracture and are carrying some of the load. To account for this fiber bridging, the volume fraction term is included in the denominator of equation 1. Since some of the fibers behind the crack front have fractured, the load carrying capacity has diminished thus necessitating the introduction of the coefficient β to account for the percentage of failed fibers. The lower bound corresponds to $\beta=0$ and represents the case when there are no fibers bridging the crack behind the crack front. The material's fiber volume fraction ($\beta=1$) provides the upper bound. This corresponds to a situation in which all of the

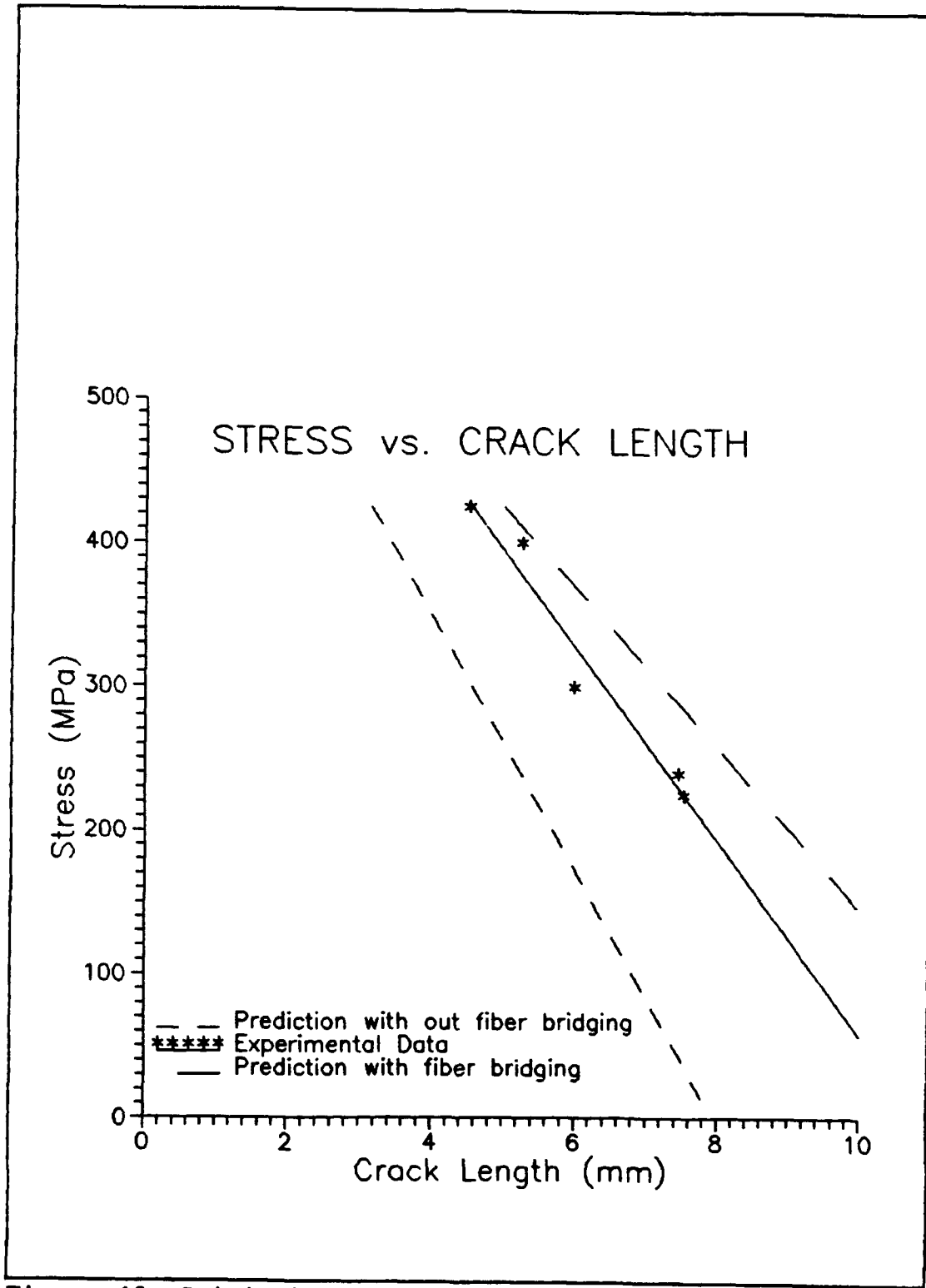


Figure 46: Critical Crack Length vs. Stress Level

fibers behind the crack front are bridging the fracture and thus aid in carrying the load. The position of the experimental line between the upper and lower boundaries is directly related to the amount of fibers bridging the crack. In this case, $\beta = .7687$ which means that 77% of the fibers behind the crack front are bridging the crack.

Damage Initiation. Hillberry and Johnson (11:5-7) developed a modified effective strain parameter based upon work done by Smith, Watson, and Topper (34) on monolithic materials. This method was devised to account for the presence of a center hole, thermal residual stresses from processing, and the fact that the material is a composite and not a monolithic.

The basic premise behind this approach is that the matrix material will fail at a given strain level. Once the strain level is reached in a composite, the matrix fails and cracks initiate. Fibers take the lion's share of the load and tend to restrain the elongation of the matrix material; therefore, the matrix is assumed to be subjected to strain controlled fatigue loading. This leads to the assumption that the matrix behaves in an elastic manner which may be checked by observing a typical stress-strain hysteresis loop (figure 47). The ratio of plastic strain to elastic strain is approximately zero which means that in fact the matrix is behaving in an

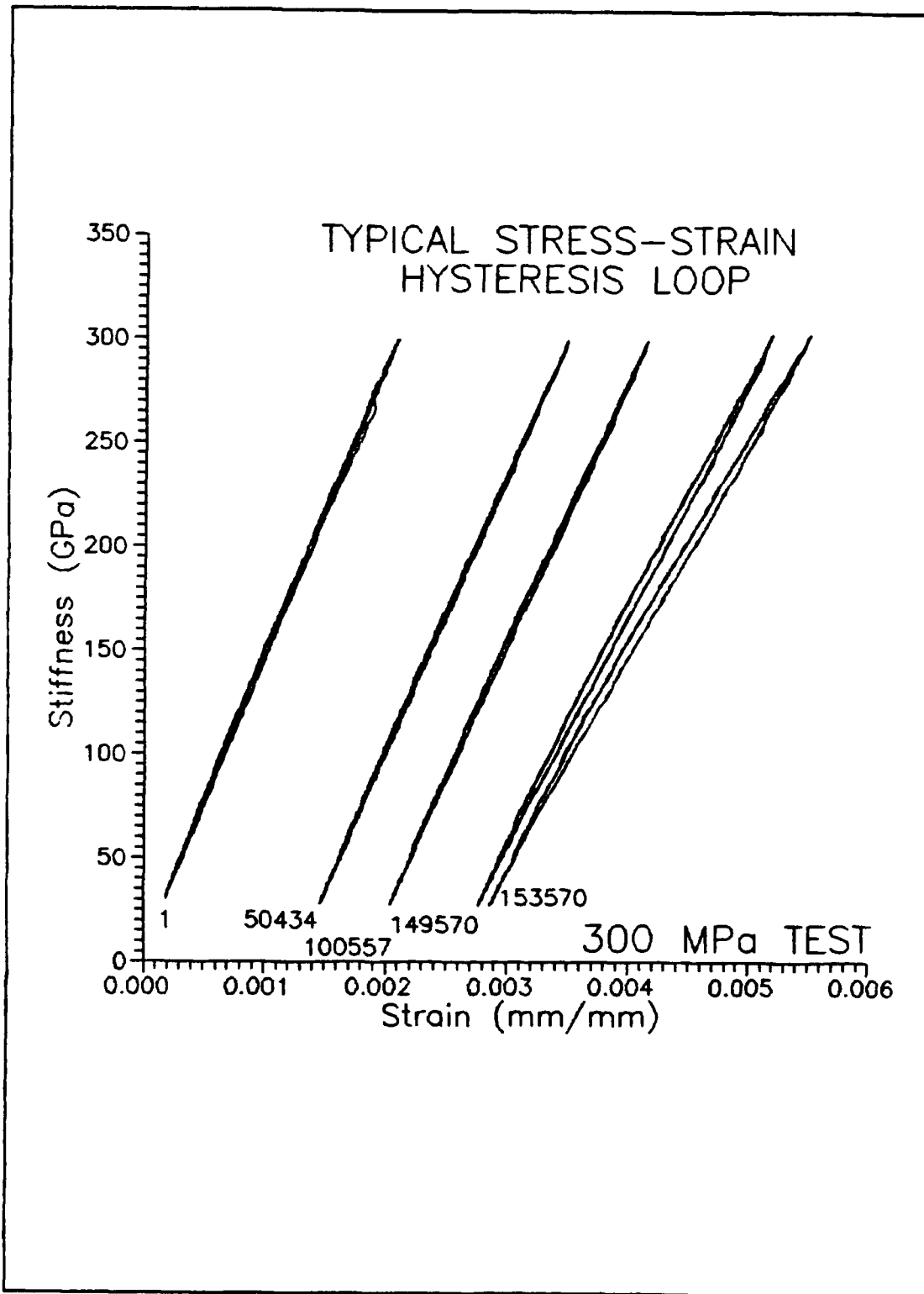


Figure 47: Stress-Strain Hysteresis Loop

elastic fashion. With the matrix acting elastically over the majority of the specimen life, the strain concentration factor can be assumed to be the same as the stress concentration factor. Thus the strain range at the edge of the hole is $K_t \Delta \epsilon$ (11:5).

To find the effective strain of the composite, Johnson defined the following quantities:

$$\epsilon_{\max} = \frac{S_{\max}}{E_L}; \Delta \epsilon = \frac{(1-R) S_{\max}}{E_L} \quad (2)$$

where R is the stress ratio, E_L is the longitudinal modulus of the laminate, and S_{\max} is the maximum far-field stress. To ensure that valid comparisons are drawn, the stress concentration factor expression used by Bakuckas et al (3:17) will be used here. It was initially developed by Lekhnitskii and is as follows:

$$K_t = a K_t^{\infty} \quad (3)$$

where a is the finite width correction factor and K_t^{∞} is the stress concentration factor for an infinite plate as defined below in equations (4) and (5). The infinite plate stress concentration factor is:

$$K_t^{\infty} = 1 + \sqrt{\frac{E_L}{G_{LT}} - 2\nu_{LT}} + 2\sqrt{\frac{E_L}{E_T}} \quad (4)$$

where E_l is the longitudinal modulus, E_T is the transverse modulus, G_{LT} is the shear modulus, and ν_{LT} is the Poisson's ratio of the composite laminate. The finite width correction factor is expressed as:

$$\alpha = \frac{2 + (1 - \frac{d}{W})^3}{3(1 - \frac{d}{W})} \quad (5)$$

where d is the hole diameter and W is the specimen width. These expressions are then incorporated into the effective strain parameter relation given below

$$\Delta \epsilon_{eff} = \sqrt{(K_t \epsilon_{max} + \frac{\sigma_m^r}{E_m}) K_t \frac{\Delta \epsilon}{2}} \quad (6)$$

where K_t is the stress concentration factor, ϵ_{max} is the maximum applied strain, σ_m^r is the matrix residual stress from manufacturing cool down, E_m is the matrix modulus, and $\Delta \epsilon$ is the applied strain range. Based on composite properties determined by METCAN and equation 5, the stress concentration factor for this set of experiments was determined to be 3.31.

Laminate properties were calculated by METCAN the Metal Matrix Composite Analyzer developed by Hopkins and Murthy at NASA's Lewis Research Center. To accomplish this, METCAN

utilizes a set micromechanical equations developed from a mechanics of materials approach for a square unit cell (13:1). Material properties used in this program are listed in Table V below for matrix properties and Table VI for the fiber properties as reported by Mirdamadi et al (23:14-15). The

Table V: Ti-15-3 Material Properties (23:14-15)

TEMP (°C)	MODULUS (GPa)	POISSON'S RATIO	COEFFICIENT OF THERMAL EXPANSION ($\times 10^6$ mm/mm/°C)
25	91.800	0.36	8.48
316	80.440	0.36	9.16
482	72.240	0.36	9.71
566	64.400	0.36	9.98
650	53.000	0.36	10.25

input file and material databank for METCAN are listed in appendix 3. Laminate properties from the METCAN program output are listed in Table VII below. Modulus values

Table VI: SCS-6 Fiber Material Properties (23:14-15)

LONGITUDINAL MODULUS	400 GPa
POISSON'S RATIO	.25
COEFFICIENT OF THERMAL EXPANSION	4.86×10^{-6} mm/mm/°C

predicted are within the data scatter band shown in figures 14 and 15 above. Once the effective strain for the composite was found, S-N curves for the matrix material at different temperatures and types of heat treatment available from literature were used to predict the initiation curve for the composite. This is done because whenever the matrix material fails, cracks initiate within the composite. Figure 48 depicts the experimental S-N curve for crack initiation plotted with the predicted S-N curves for the various heat treatments. Three different matrix conditions are examined. The first comparison is with the material used by Johnson et al (3:21). They used material in the as received condition (ASF) with a strain ratio of 0.1 at room temperature. Second, a comparison is made with strain data recorded by Gabb et al (7:4) which was heat treated at 700°C for 24 hours in a vacuum (same as this experiment). Gabb's experiment was performed with a strain ratio of 0 at room temperature. The third material, examined by Gayda et al (8:501), was heat treated at 593°C for 24 hours in an argon atmosphere. Their tests were run with a strain ratio of 0 at 300°C. The cyclic life for each condition is listed in Table VIII. Unfortunately, data for material heat treated at 700°C for 24 hours in a vacuum with a strain ratio of 0.1 at 427°C was not available. However, data extrapolated from the experiment indicates that the matrix curve for the condition tested here should lie

Table VII: Laminate Properties from METCAN at 427°C

LONGITUDINAL MODULUS	153.9 GPa
TRANSVERSE MODULUS	153.9 GPa
POISSON'S RATIO	.2339
ULTIMATE STRENGTH	704.0 MPa

Table VIII: Stress Level and Cyclic Life

STRESS (MPa)	$\Delta\epsilon_{eff}$	ACTUAL	ASF, AMB	700/24/VAC, AMB	593/24/Ar, 300°C
170	.00234	>8.5M	100K	252K	15.5M
225	.00301	50.0K	50K	136K	2.75M
240	.00322	25.0K	35K	116K	1.74M
300	.00384	12.5K	25K	75K	551K
400	.00505	7.5K	12K	38K	78K
425	.00540	4.0K	8K	33K	49K

along the solid line of figure 48 below.

At room temperature, the heat treated material is seen to be able to withstand higher loads for a given life span and is reflected by the heat treated curve being above and to the right of the non-heat treated curve as shown in figure 48. At the lower stress levels, additional cold working takes place which tends to weaken the heat treated material sufficiently that the non-heat treated material would have a longer life.

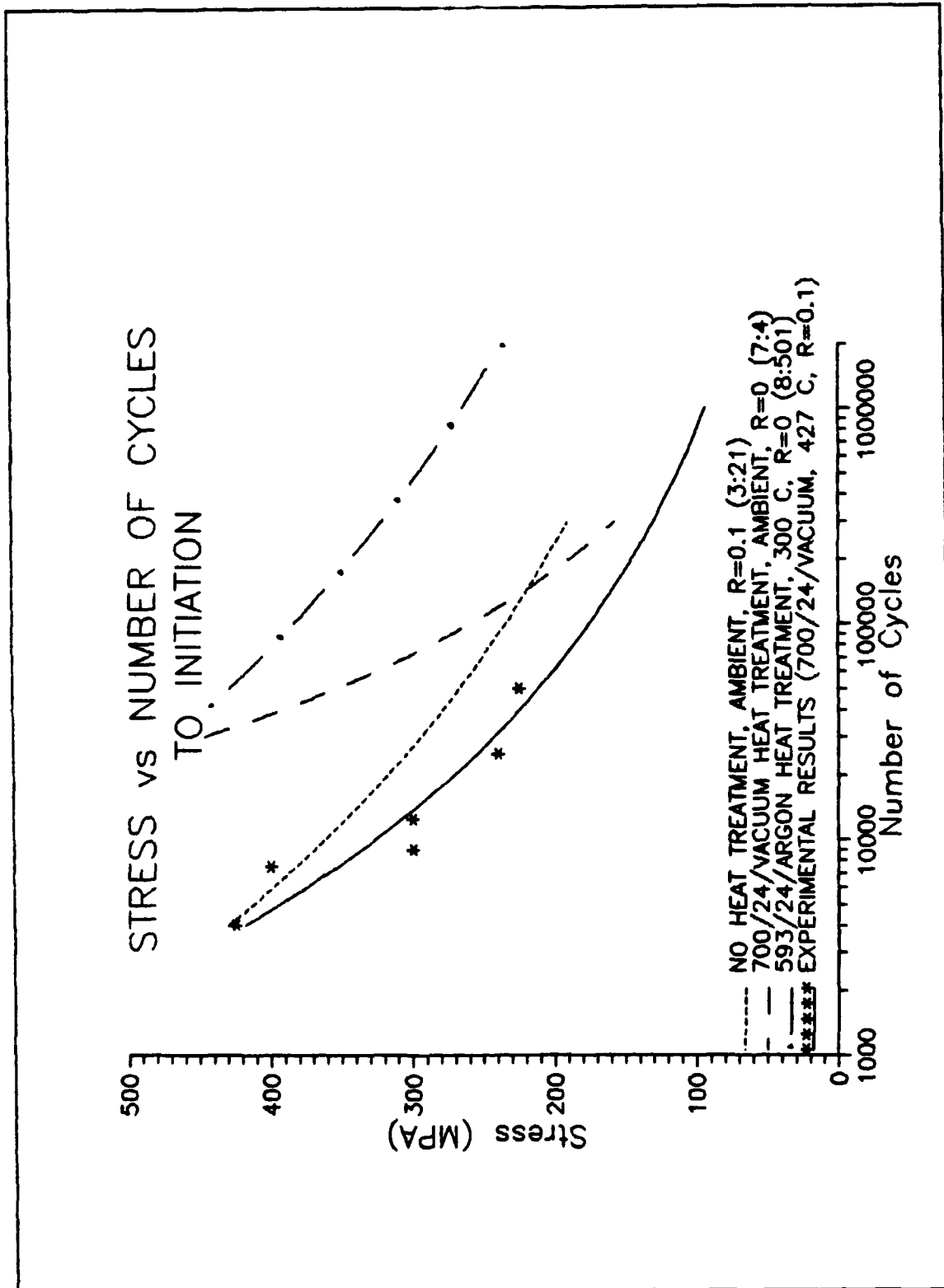


Figure 48: Crack Initiation Prediction

In general, heat treatment yields a longer life for a given stress level because the micro-structure of the composite is allowed to stabilize.

For a given heat treatment, the ambient curve overpredicts the results obtained at elevated temperatures. That is, specimens subjected to ambient temperatures will have a longer life than those at elevated temperatures. To see this, observe that the ambient temperature 700/24/vacuum curve is above and to the right of the elevated temperature 700/24/vacuum curve. This can be thought of as being the limiting case for a specimen's life. Note that at the lower stress levels, the high temperature experimental results and the room temperature curves approach one another asymptotically. This indicates that, at low stress levels, the life should not change drastically between room temperature and 427°C (for this heat treatment). Depending on the type of heat treatment, the S-N curve will shift from the ambient, no heat treatment position to the heat treated curve position by different amounts. For example, the curve for specimens heat treated at 593°C for 24 hours in an argon atmosphere is shifted much higher than that for the 700/24/vacuum heat treatment.

Generally, the high temperature curves are shifted down and toward the left proportionately from the ambient curve for a given heat treatment. Individual variations, however, may occur due to strain ratio differences. This leads to a longer life at higher temperature for a given stress level and heat treatment.

Crack Initiation and Growth Synopsis

Combining the information from above, with replica analysis, fractographic examination, and the metallographic inspection a clear picture of the damage progression may be drawn. For a given heat treatment, maximum far field applied stress, and given material properties; a prediction of the number of cycles to crack initiation may be made using the modified effective strain parameter (equation 4) developed by Johnson et al. METCAN, AGLPLY, or any of the algorithms which calculate laminate and composite properties are acceptable for determining the properties for use Johnson's formulation.

At high temperature, this study observed that damage initiates on the front and back specimen faces at four points located between 60° and 80° from the loading axis along the hole periphery. This is due to high shear stresses in the material as shown by Newaz and Majumdar for a unidirectional composite. These initial cracks are, by nature, brittle cleavage fractures. Fractography reveals that the four major

cracks grow from the faces toward the interior of the specimen. Once the front and back face cracks intersect in the center of the specimen, the cracks progress rapidly toward the specimen edge. When the majority of the elastic strain energy is consumed during crack formation, the growth rate slows down. During the crack growth phase, 77% of the fibers behind the crack front were bridging the fracture and aided in carrying the load. Simultaneously, low stress specimens are being work hardened by the loading action combined with long exposure to high temperature. Damage then accelerates as the cracks approach the critical crack length predicted by equation (1). Once this length is reached, the fracture changes nature from brittle cleavage to ductile fracture. At this point the material fails due to tensile overload and the specimen separates.

V. Conclusions and Recommendations

Studies of this nature require many tests with frequent stops for replication. For this reason, the study is labor intensive and progress is slow. This work is but a small piece of the larger body of research necessary for the complete characterization of this material and its response to fatigue loading.

Through the execution of one static test at elevated temperature, material behavior and properties were determined as were the load levels to be used in fatigue testing. Seven fatigue tests were conducted at different load levels and a temperature of 427°C. Replica analysis in conjunction with fractographic and metallographic analysis of failed specimens showed that cracks form on the specimen face then grow toward the center of the specimen (in the thickness direction). The number of cycles to initiation was predicted by the use of the modified effective strain parameter developed by Hillberry and Johnson (10 and 11). These cracks form between 65° and 72° from the loading axis. The fracture surface at this point is brittle cleavage in nature. Once a critical crack length is attained, as predicted by equation (1), the fracture transitions from brittle failure to ductile failure.

This study provided insight into the initiation and progression of damage in cross-ply SCS-6/Ti-15-3 at elevated temperature. Room temperature tests have shown that damage starts at four locations between 65° and 72° from the loading axis for a unidirectional [0]₁ composite of the same material. This study demonstrated that the same mechanisms are at work to induce damage at high temperatures. Cracking initiates at these points because of the presence of the outer 0° layer of fibers. Additional investigation should be conducted at both room temperature and 427°C for unidirectional [90]₁ and [90/0]₂ to determine the location of crack initiation.

The modified effective strain parameter was shown to be an effective tool in predicting crack initiation at high temperature. METCAN was shown to be a viable tool in predicting the material properties for use in this prediction method. Analysis showed the interrelationships between different heat treatments, temperatures, and strain ratios. More work is needed to characterize the behavior of the matrix material for different temperatures and heat treatment conditions. A complete database could be generated for just this information.

This study developed a simple strength of materials approach for the prediction of the critical crack length at which point failure occurs. This model accounts for fiber bridging and permits determination of the percentage of

bridging fibers behind the crack. Though not specifically addressed in the calculations, this model uses laminate properties at the temperature at which the test is run and thus is useful for tests at both ambient and elevated temperatures. Crack lengths and growth were measured and recorded. Trends were then analyzed. Additionally, S-N curves were generated for crack initiation and failure for this notched cross ply MMC at 427°C. Detailed metallographic and fractographic analysis led to the formation of a clear picture of crack initiation and progression.

Characterization of a material's fatigue response is a long and laborious task. This study provided a small piece of the much bigger picture. A large body of research still needs to be conducted in order to fully characterize the material's behavior. One proposed use for this material is as a structural member on the National Aerospace Plane (NASP) which would be subjected to extremely high temperatures in atmospheric flight and orbital reentry. Much work has been done to identify the high temperature attributes of SCS-6/Ti-15-3. But, space is inherently cold. What are the low temperature properties and what fatigue characteristics exist when the material is cold? Work needs to be done to examine the material's low temperature responses.

Appendix 1

Strain vs Cycle Curves

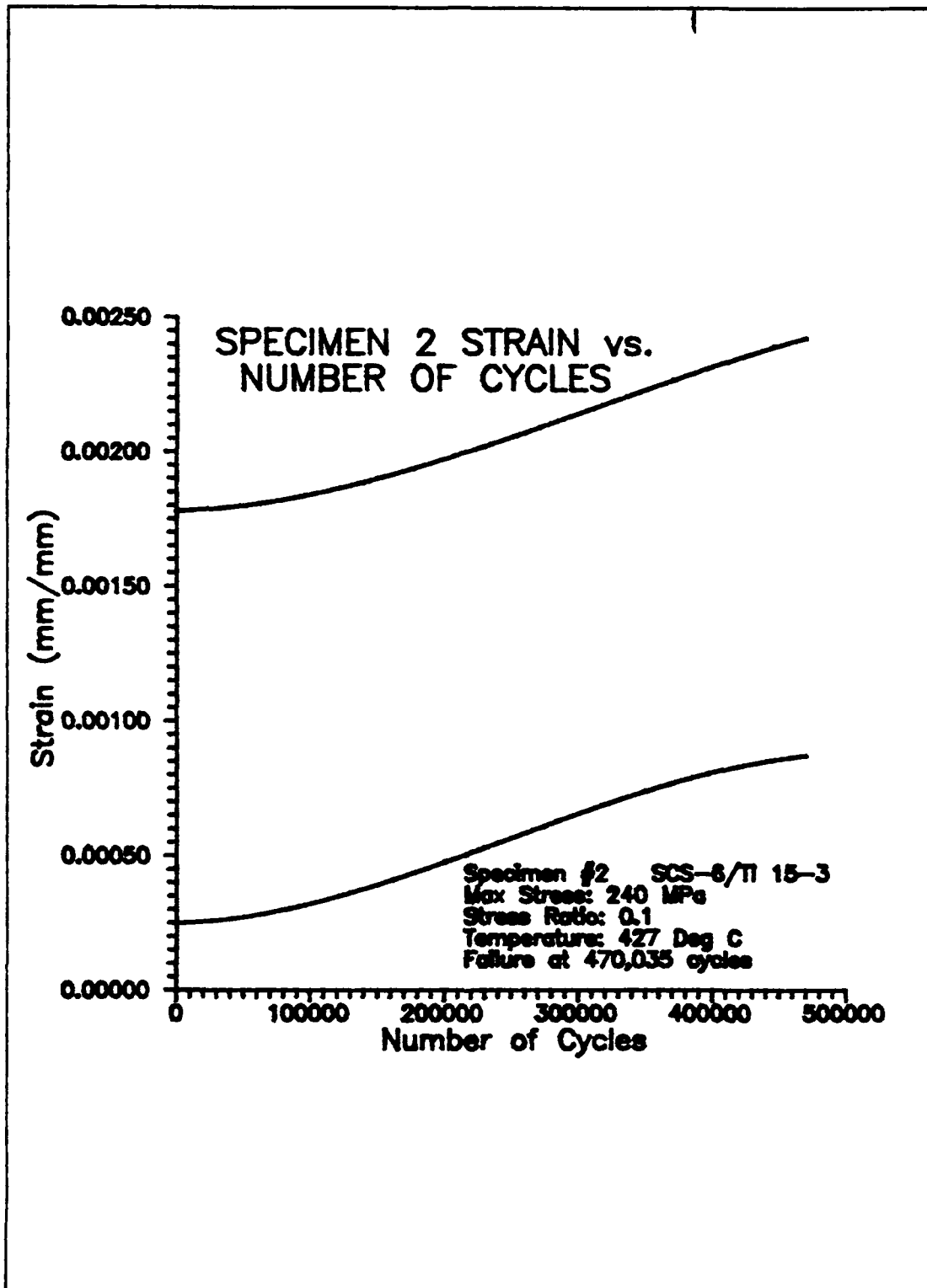


Figure 49: Specimen 2 (240 MPa) Strain vs. Cycles

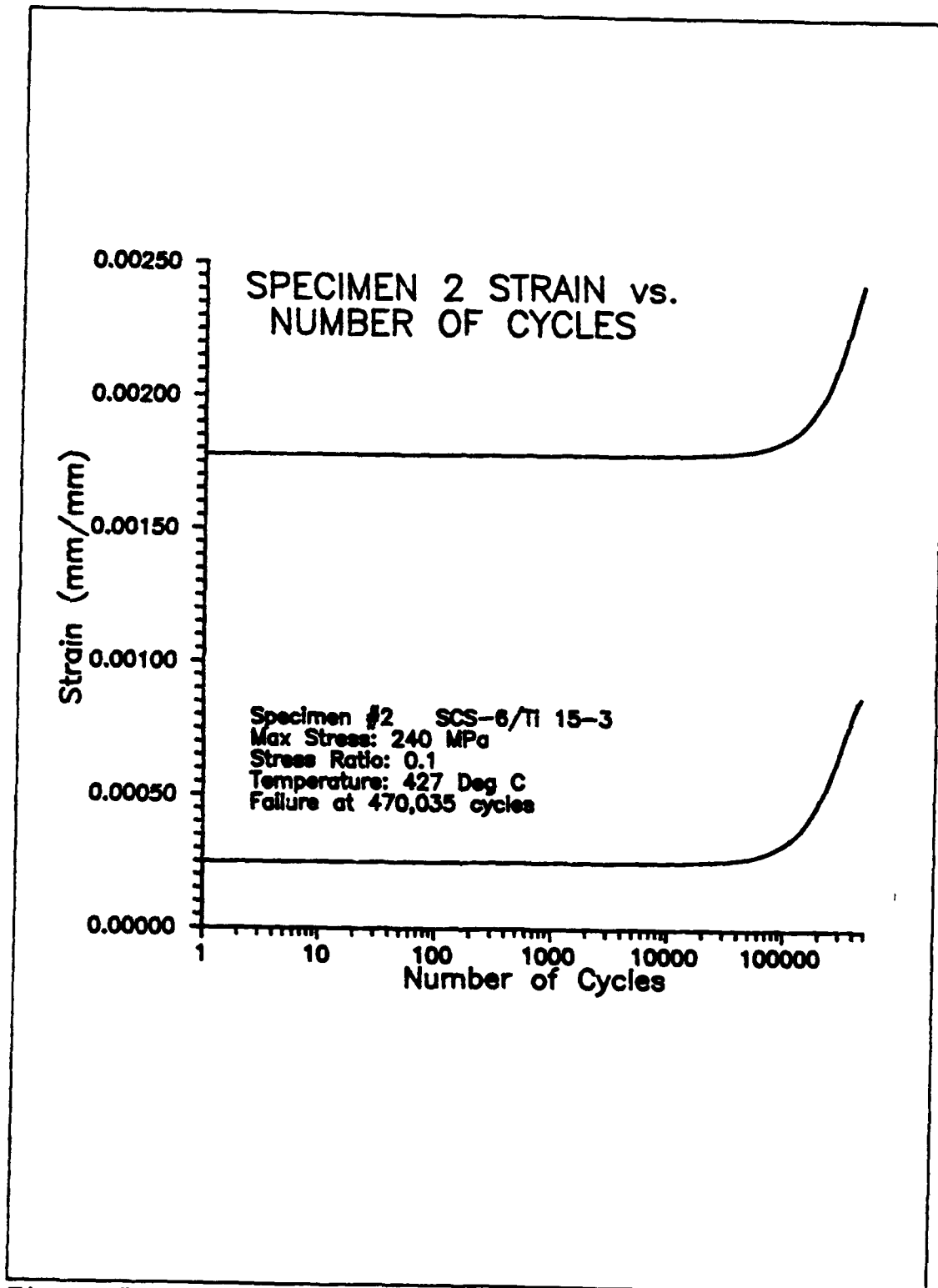


Figure 50: Specimen 2 (240 MPa) Strain vs. Log Cycles

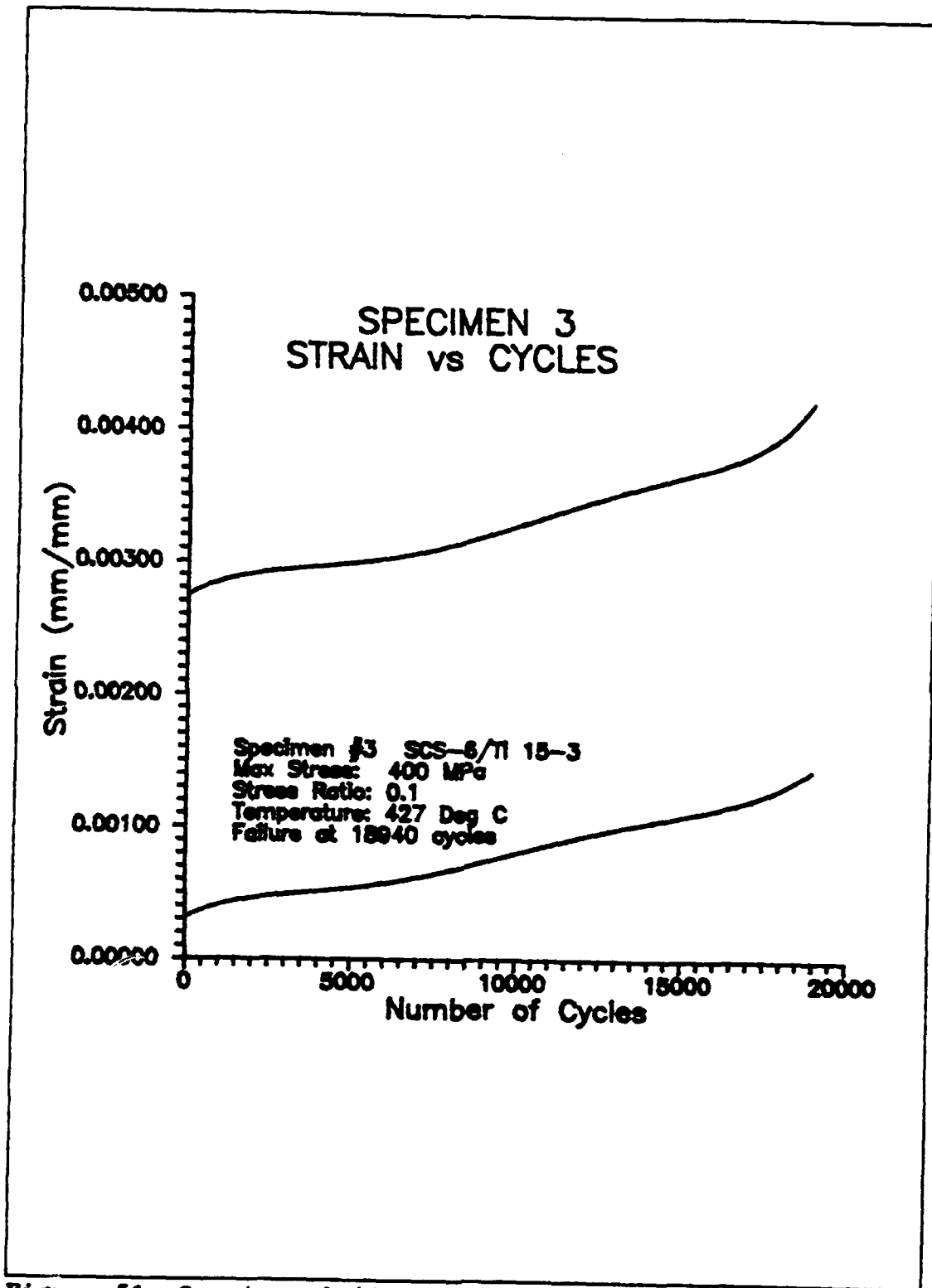


Figure 51: Specimen 3 (400 MPa) Strain vs. Cycles

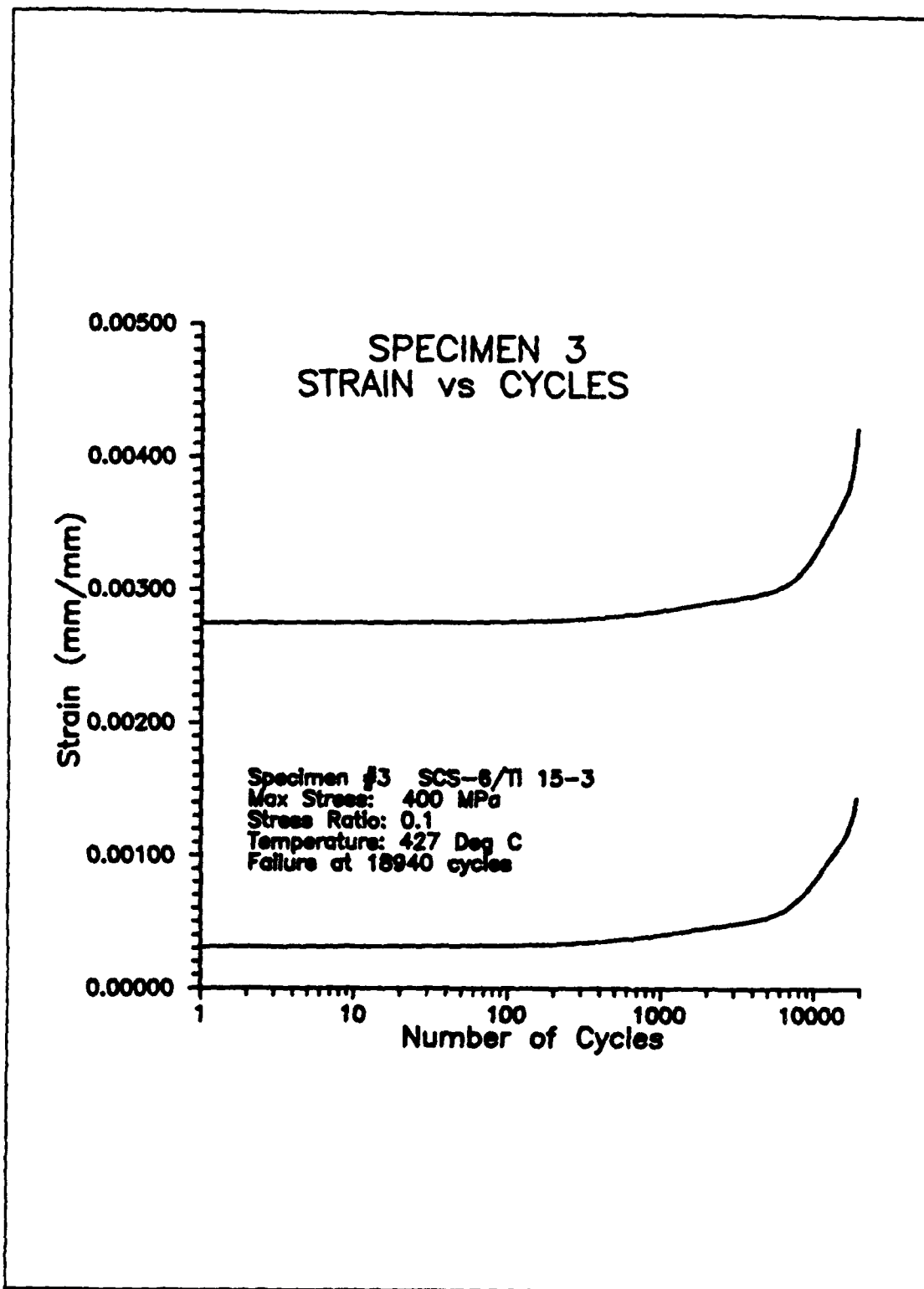


Figure 52: Specimen 3 (400 MPa) Strain vs. Log Cycles

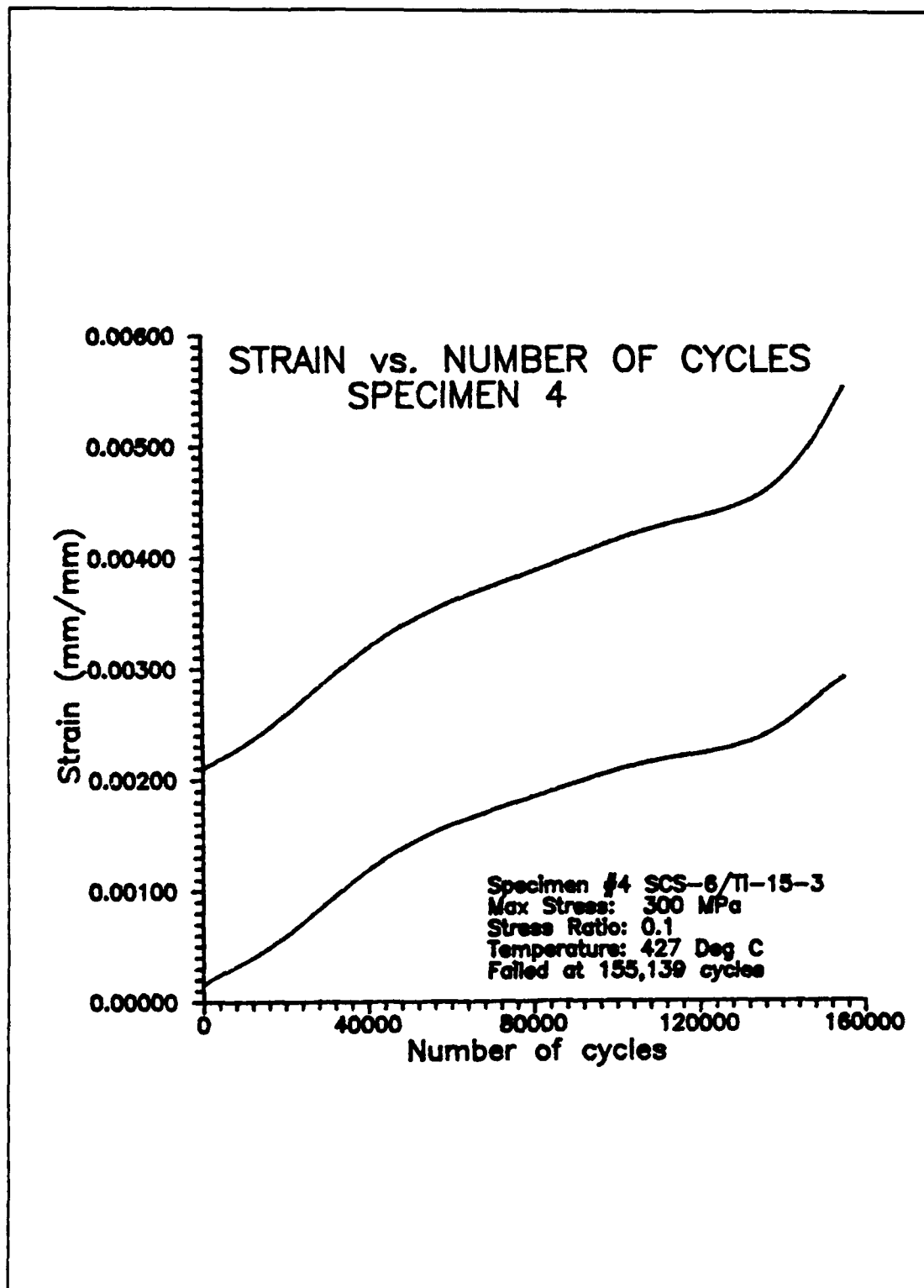


Figure 53: Specimen 4 (300 MPa) Strain vs. Cycles

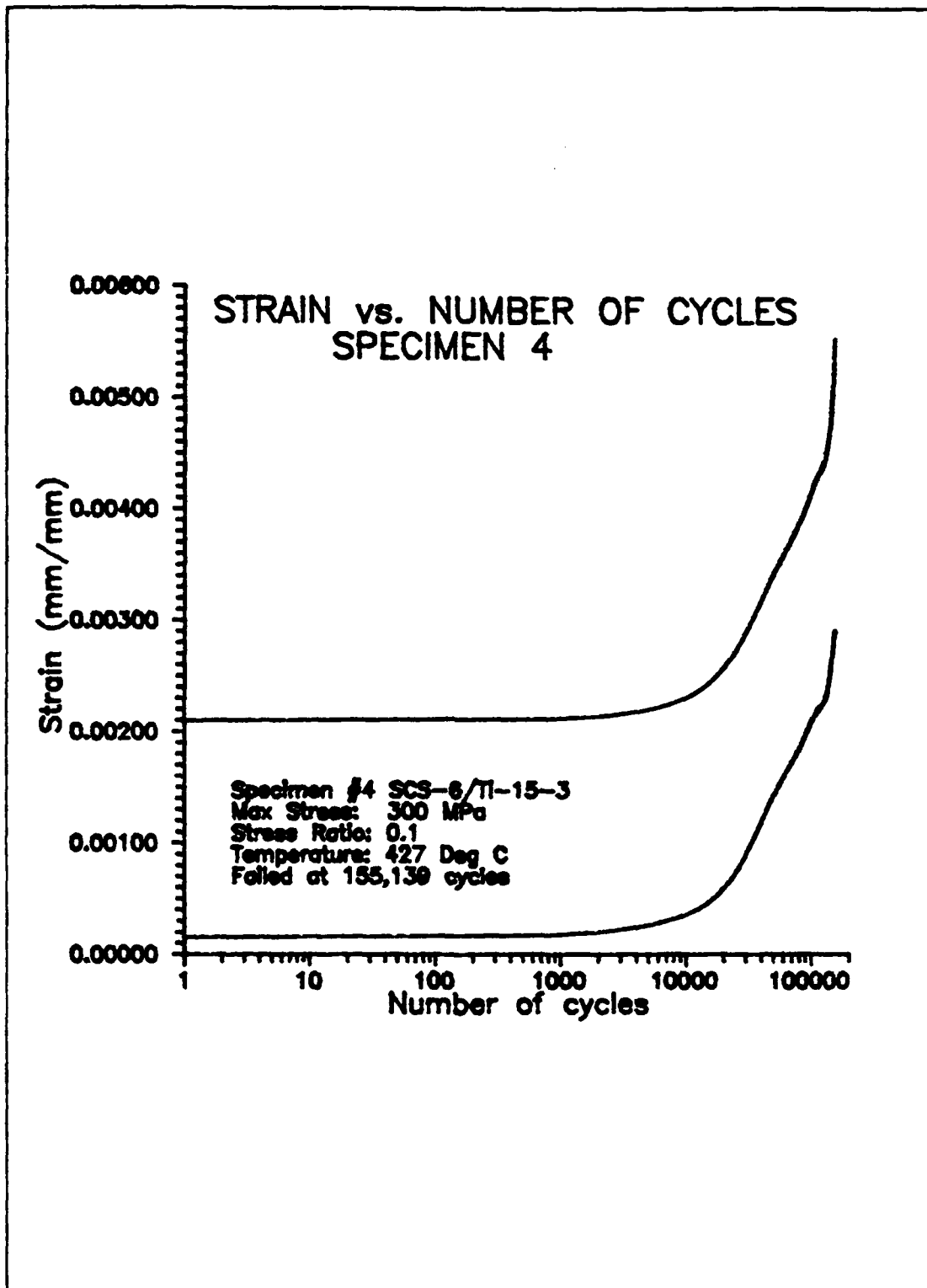


Figure 54: Specimen 4 (300 MPa) Strain vs. Log Cycles

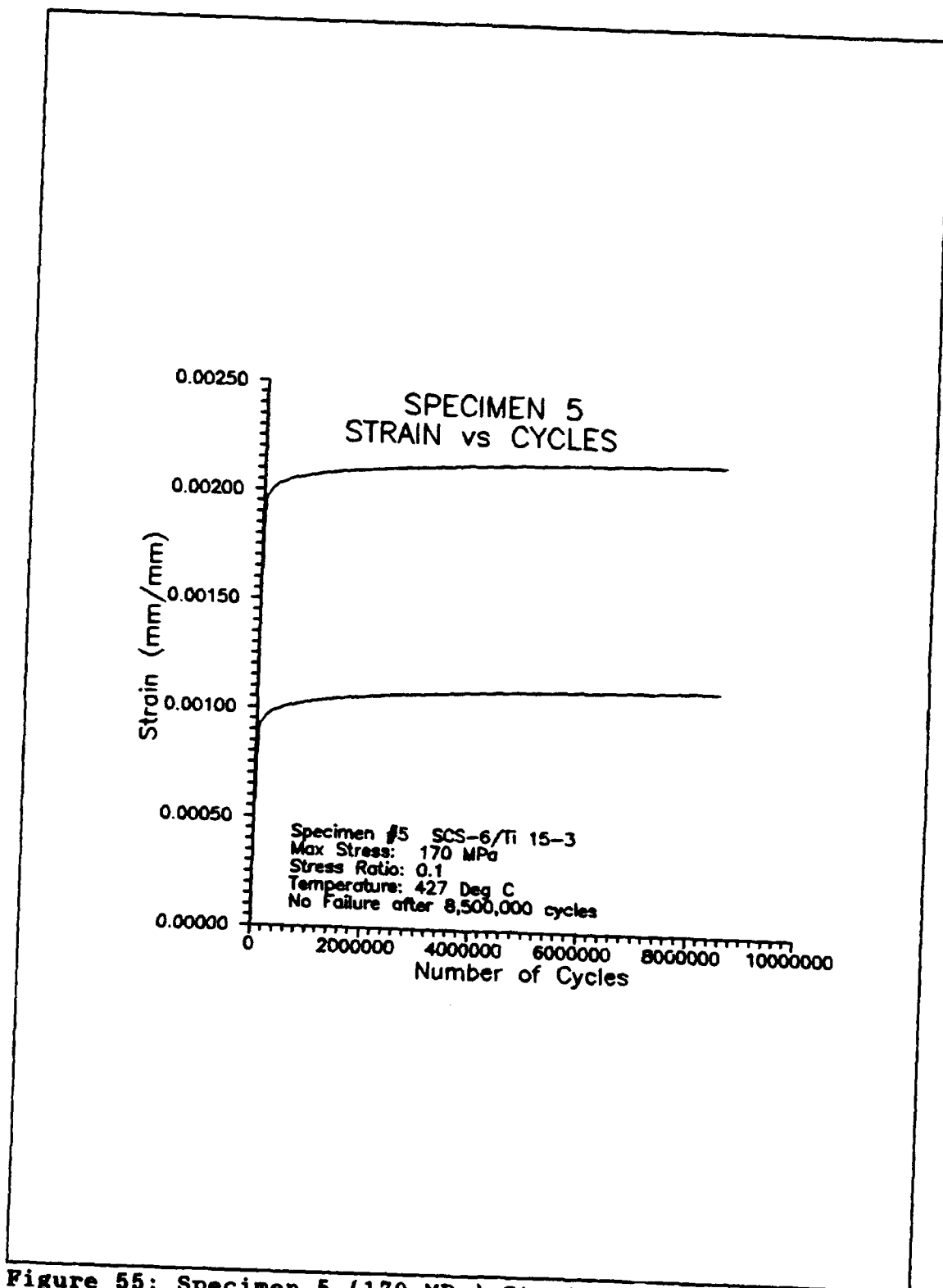


Figure 55: Specimen 5 (170 MPa) Strain vs. Cycles

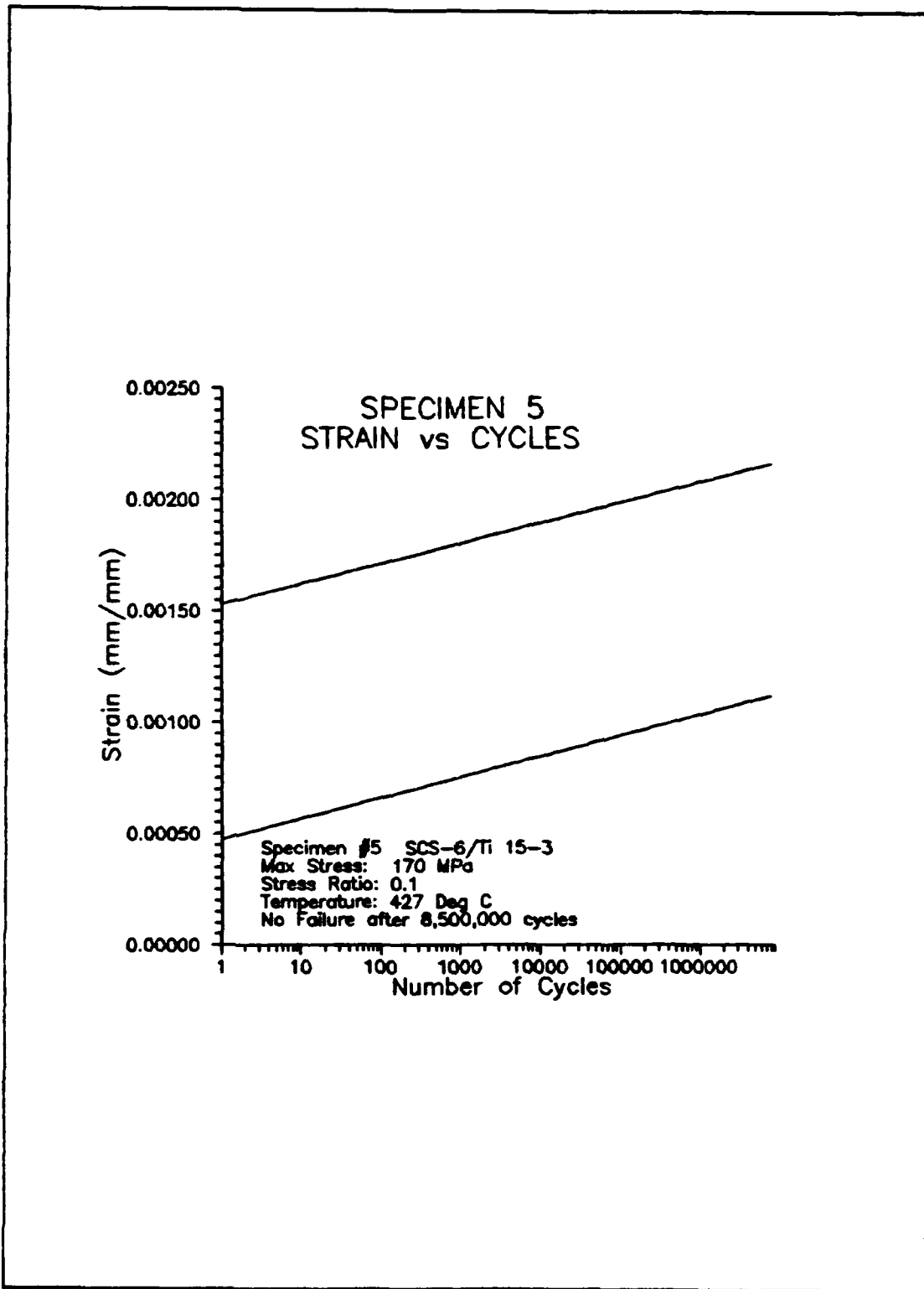


Figure 56: Specimen 5 (170 MPa) Strain vs. Log Cycles

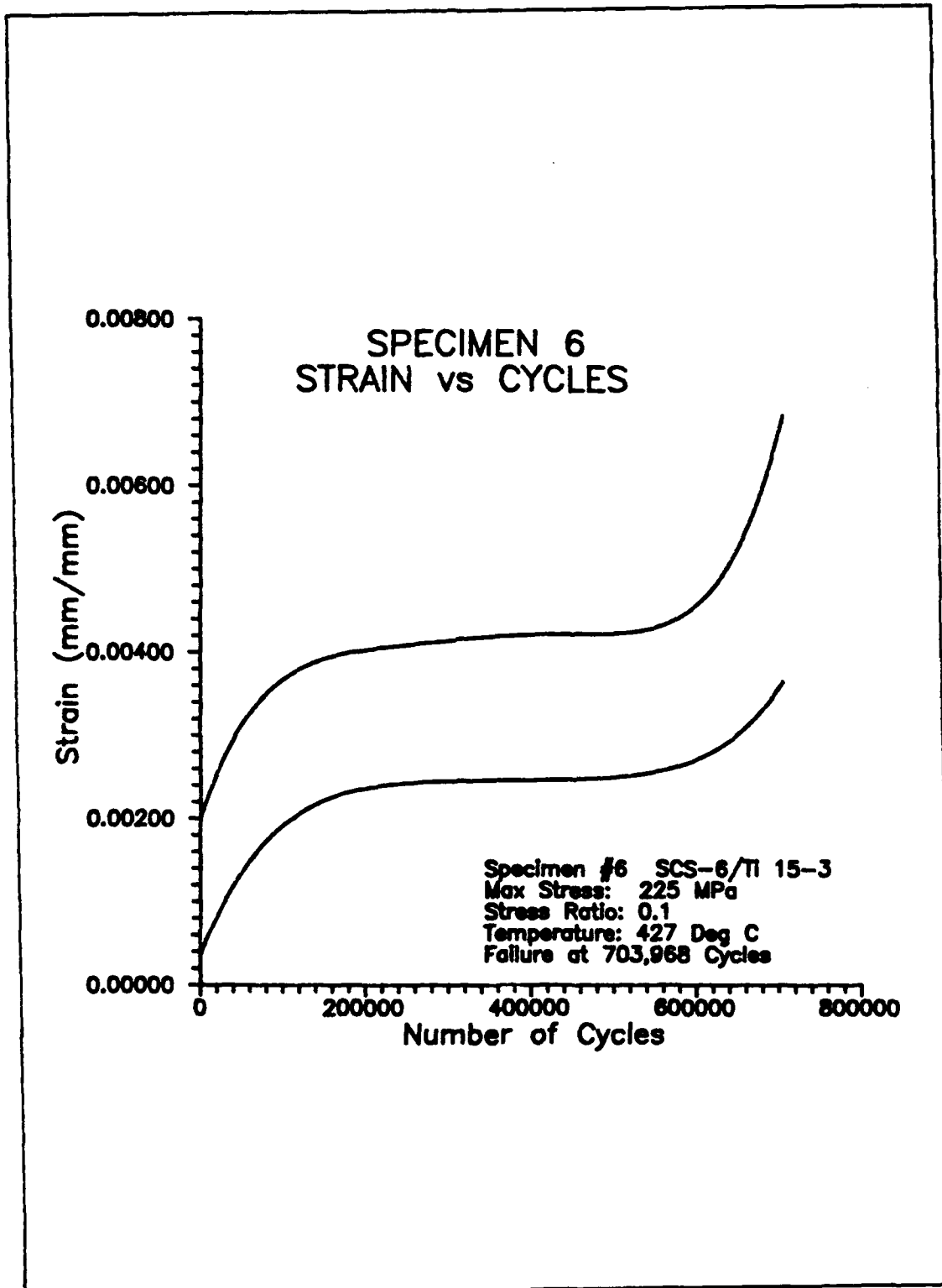


Figure 57: Specimen 6 (225 MPa) Strain vs. Cycles

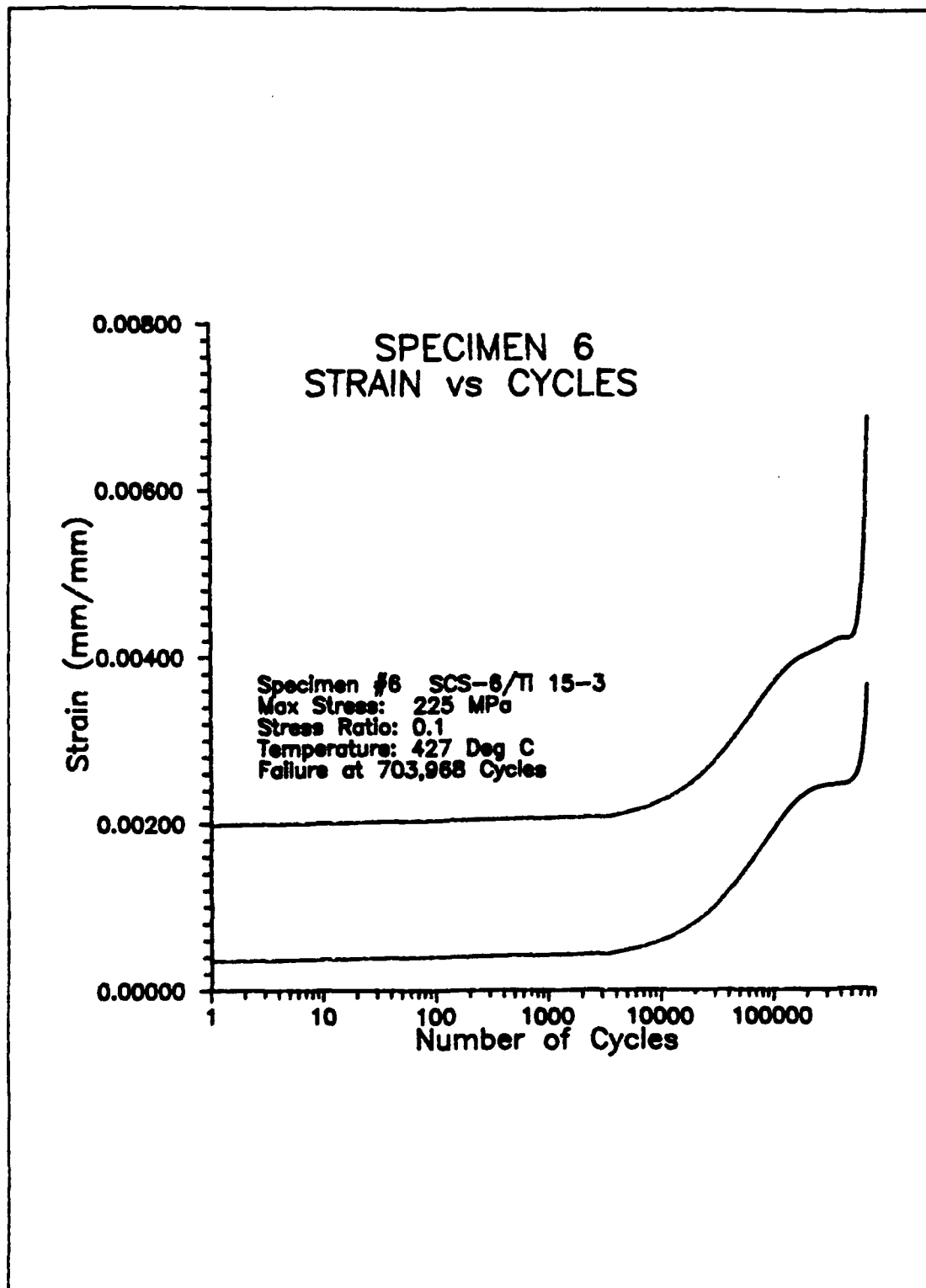


Figure 58: Specimen 6 (225 MPa) Strain vs. Log Cycles

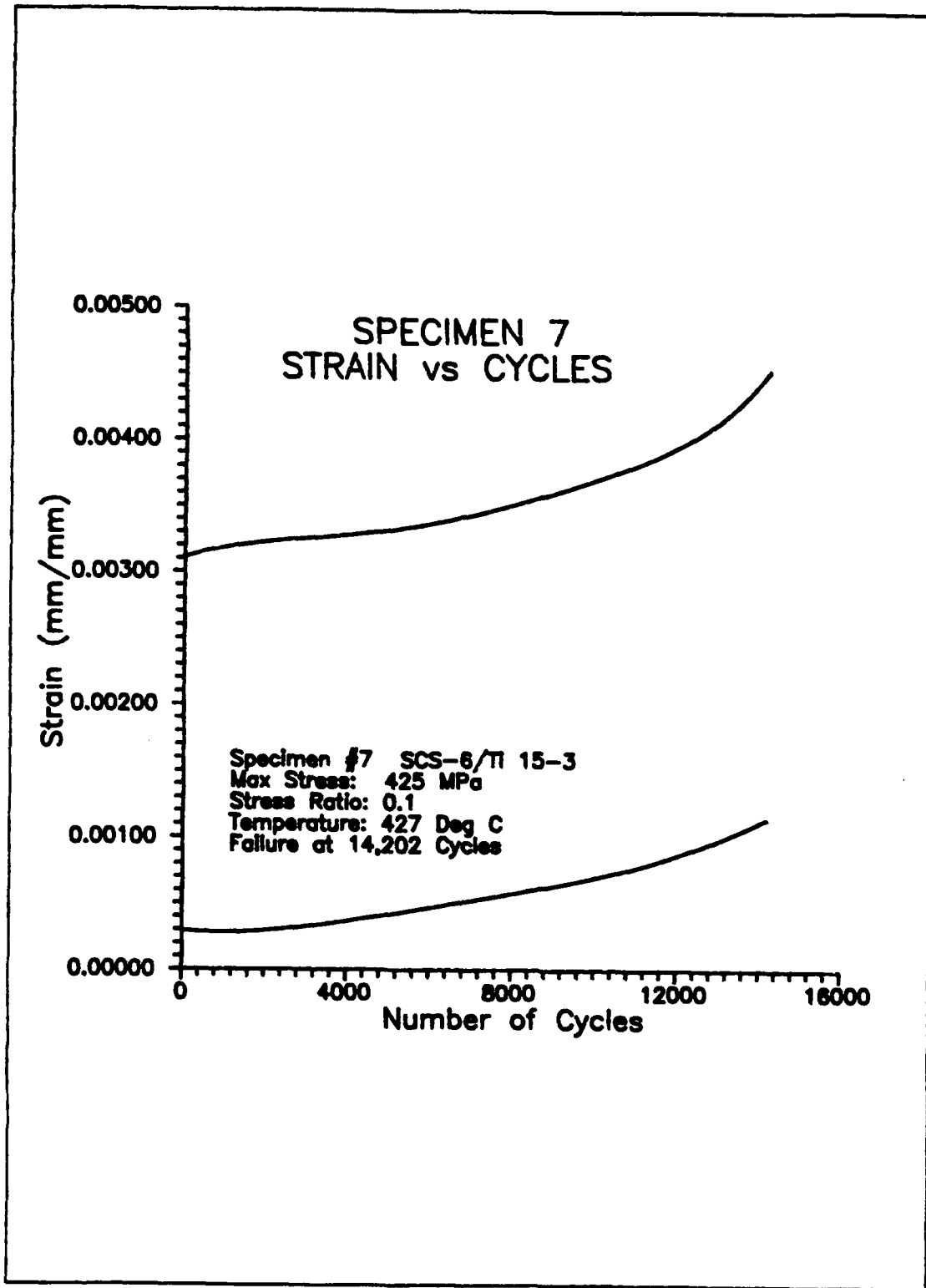


Figure 59: Specimen 7 (425 MPa) Strain vs. Cycles

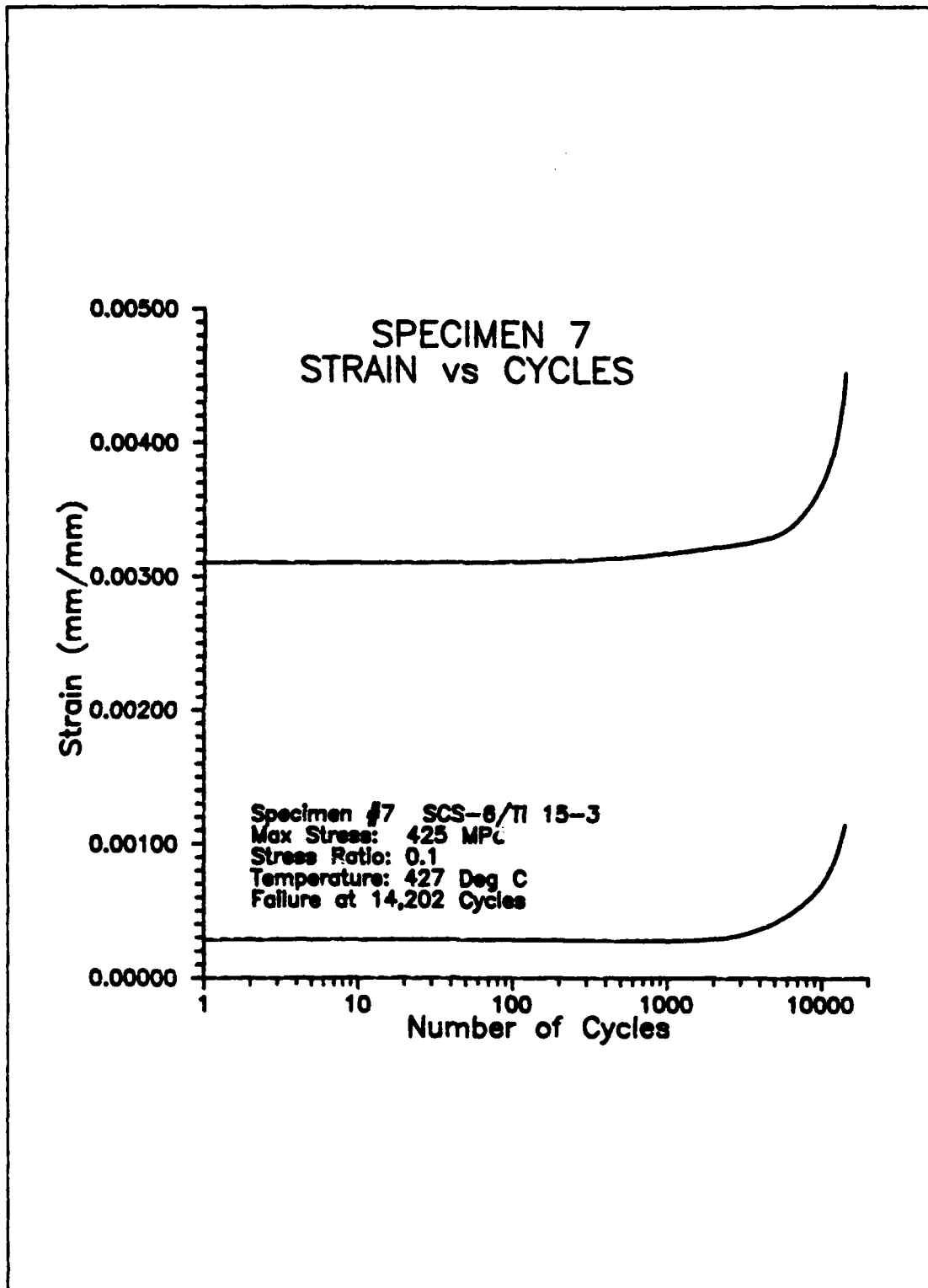


Figure 60: Specimen 7 (425 MPa) Strain vs. Log Cycles

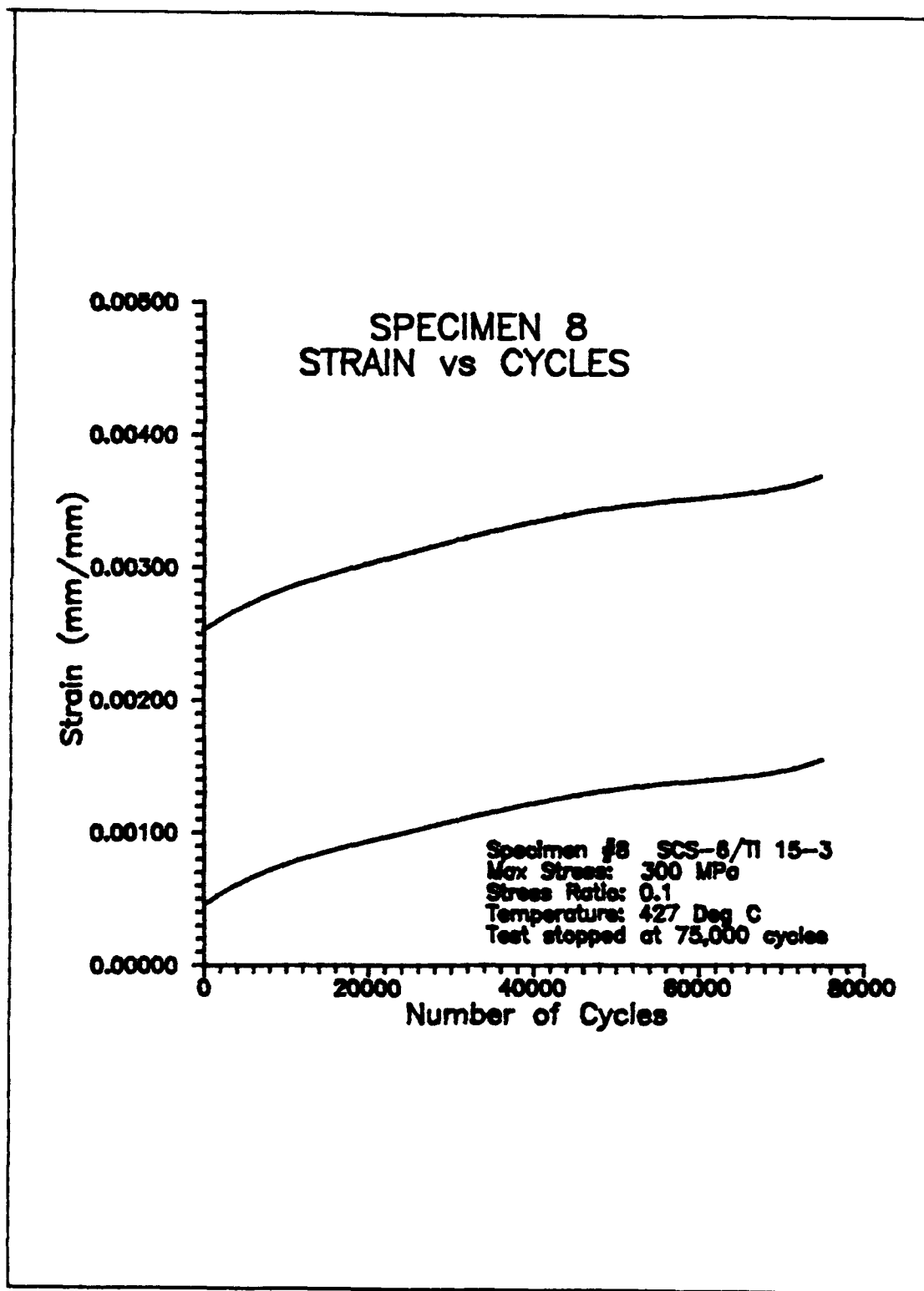


Figure 61: Specimen 8 (300 MPa) Strain vs. Cycles

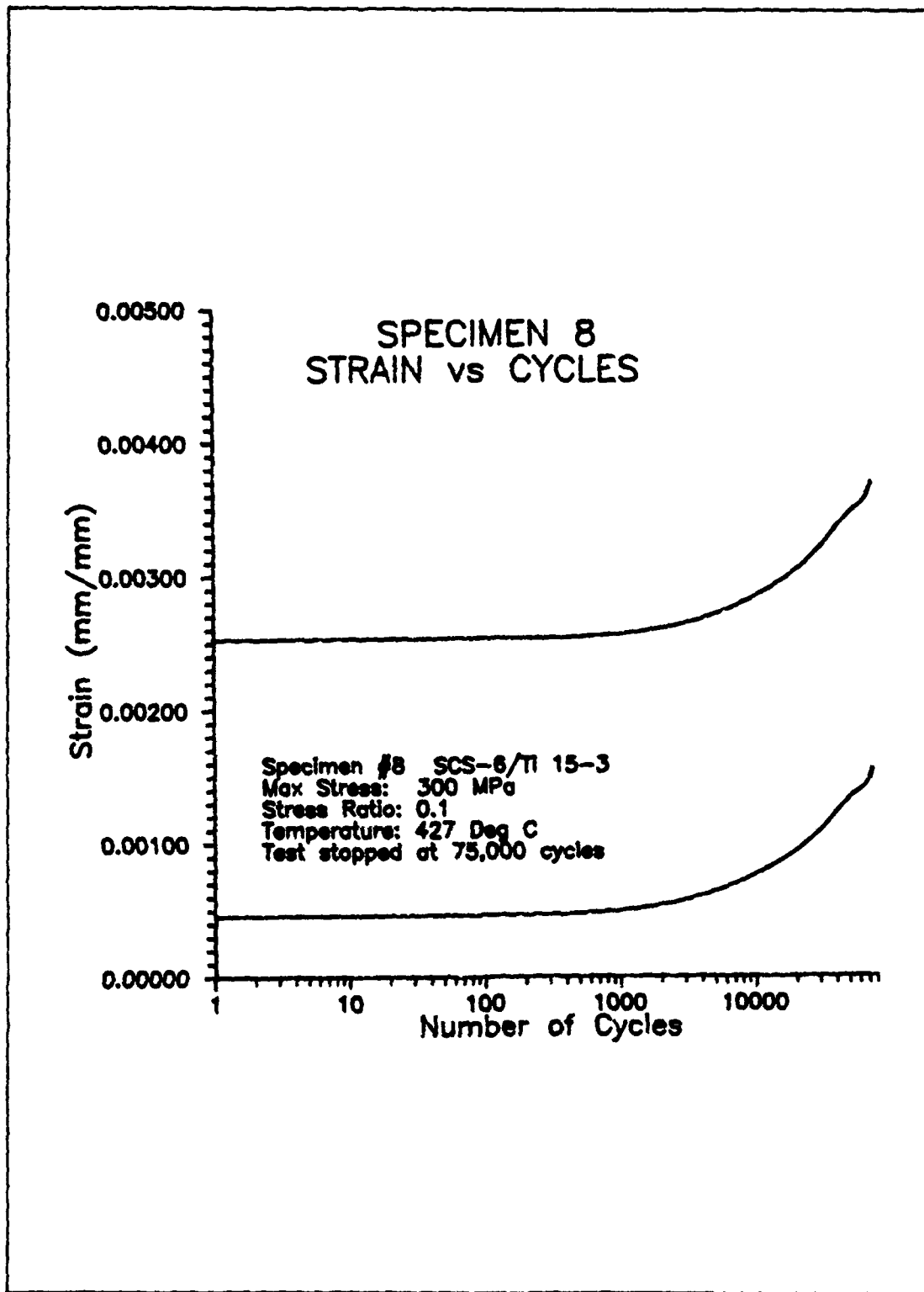


Figure 62: Specimen 8 (300 MPa) Strain vs. Log Cycles

Appendix 2

Modulus vs Cycle Curves

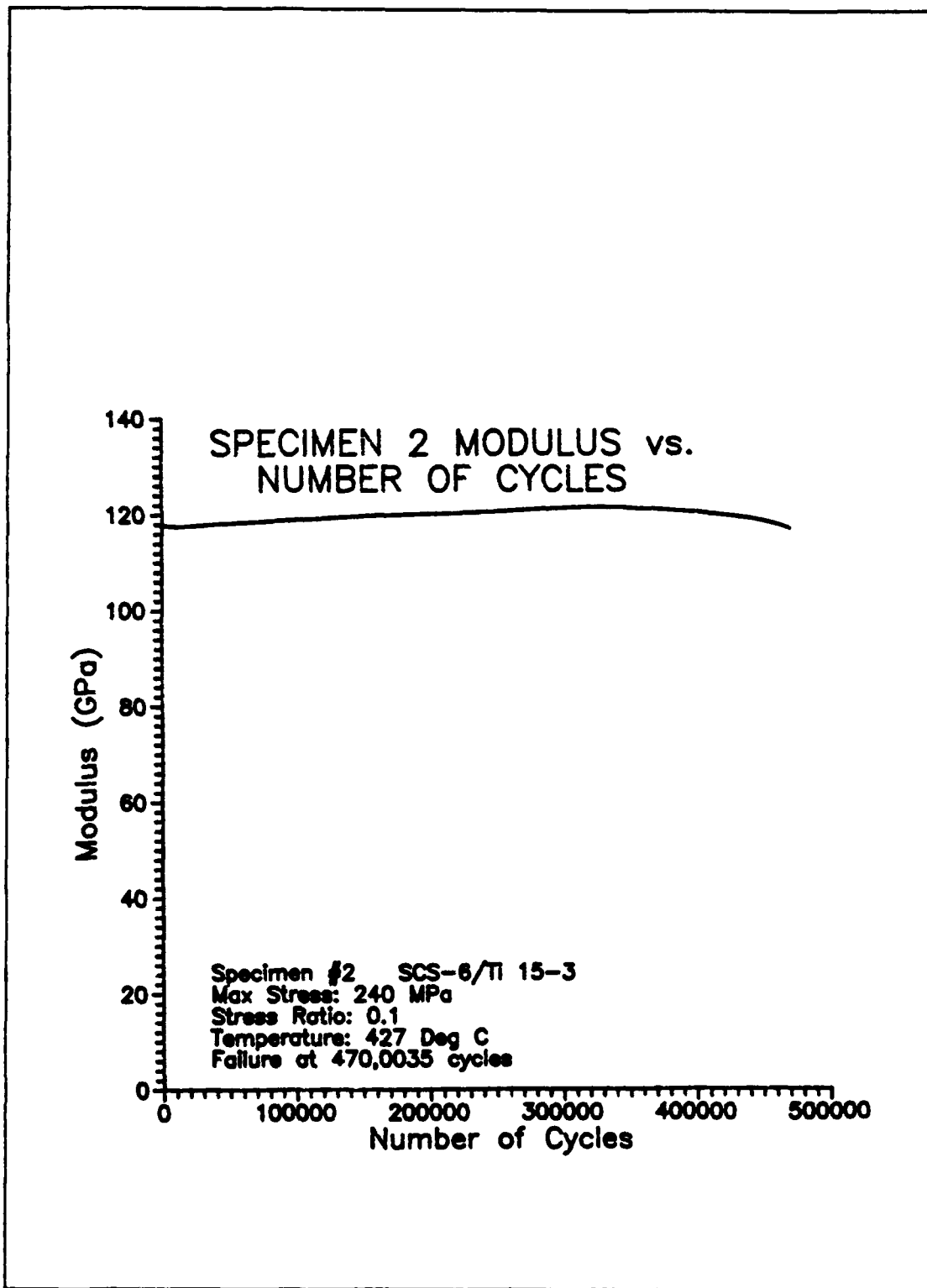


Figure 63: Specimen 2 (240 MPa) Modulus vs. Cycles

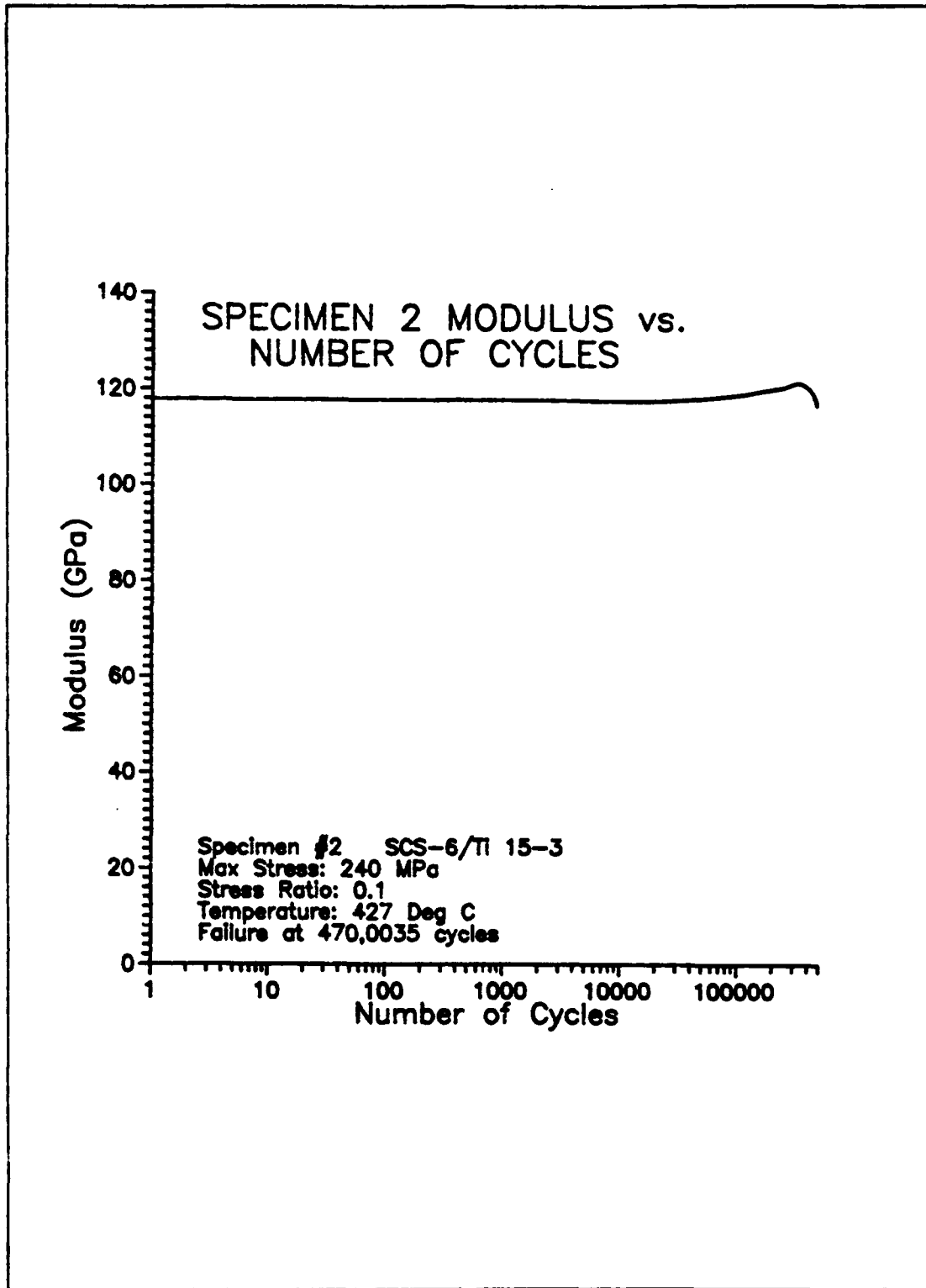


Figure 64: Specimen 2 (240 MPa) Modulus vs. Log Cycles

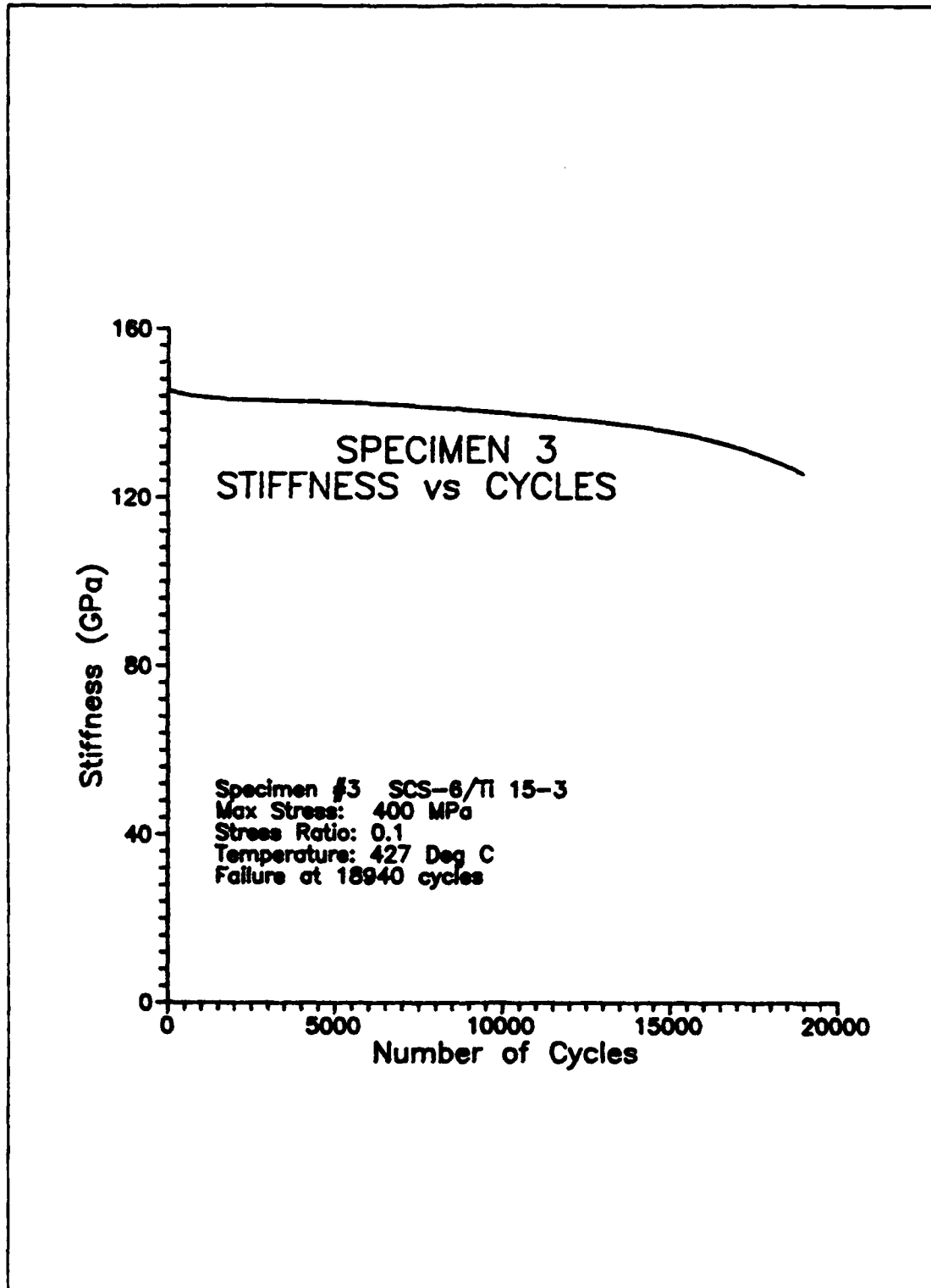


Figure 65: Specimen 3 (400 MPa) Modulus vs. Cycles

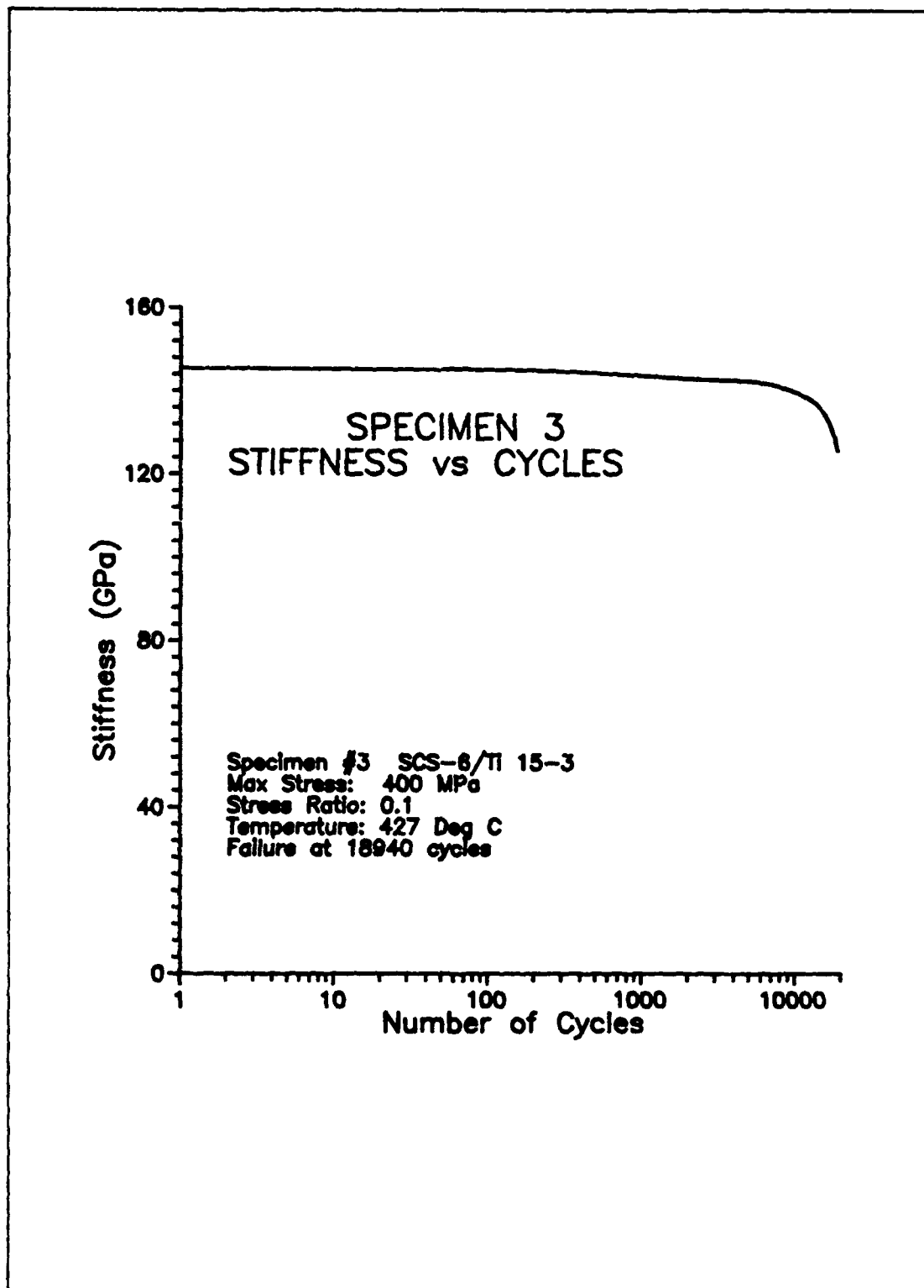


Figure 66: Specimen 3 (400 MPa) Modulus vs. Log Cycles

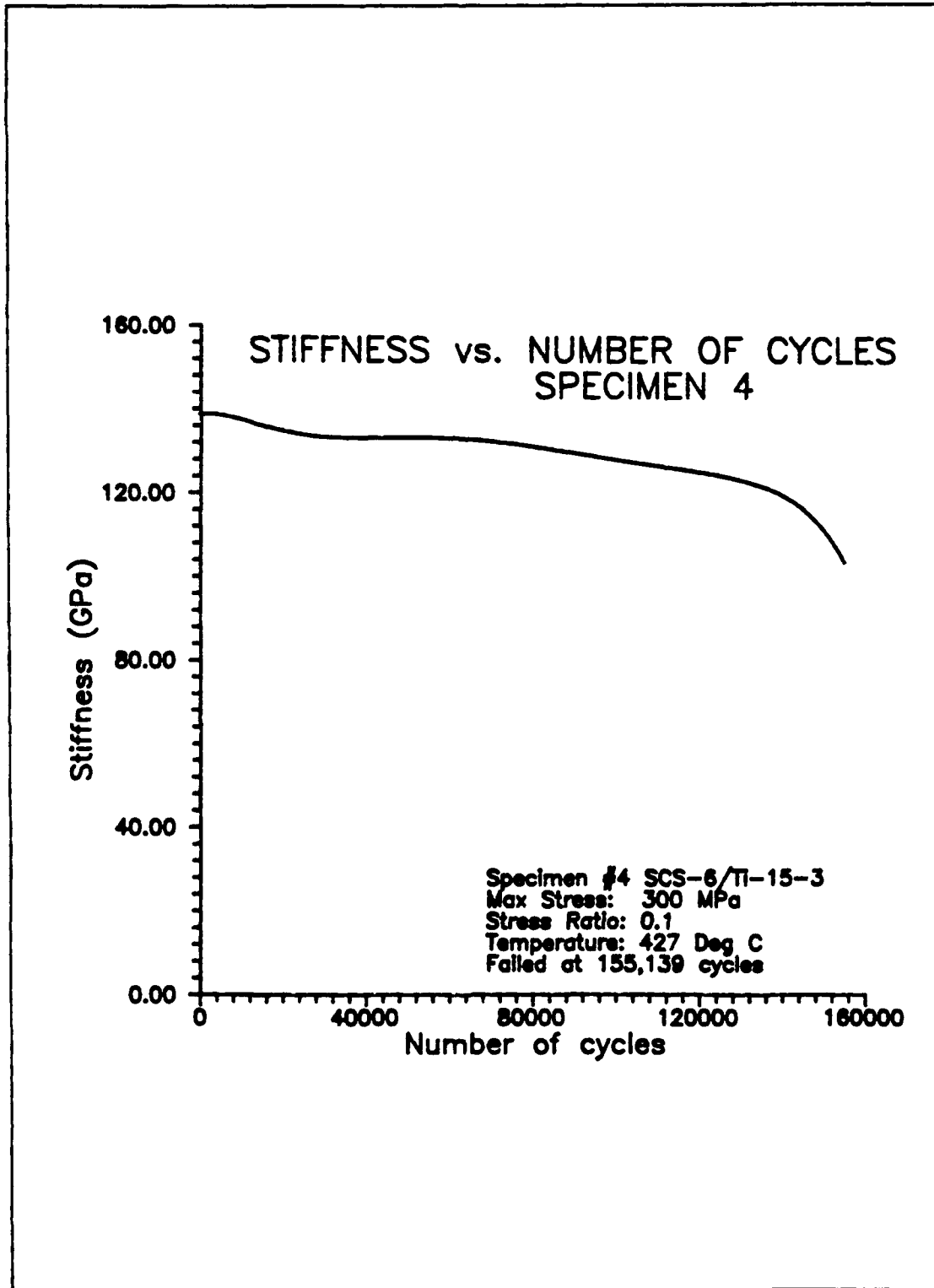


Figure 67: Specimen 4 (300 MPa) Modulus vs. Cycles

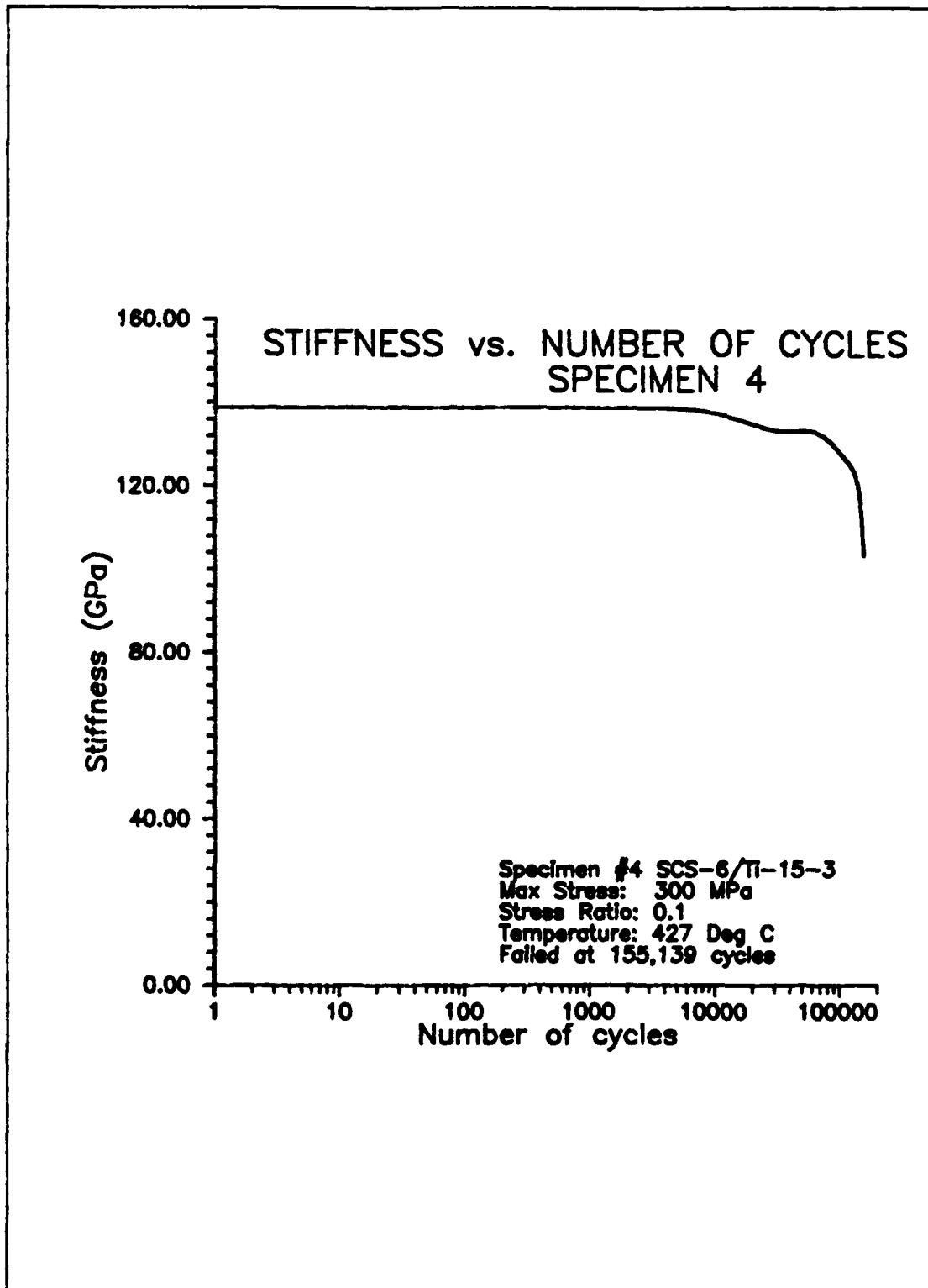


Figure 68: Specimen 4 (300 MPa) Modulus vs. Log Cycles

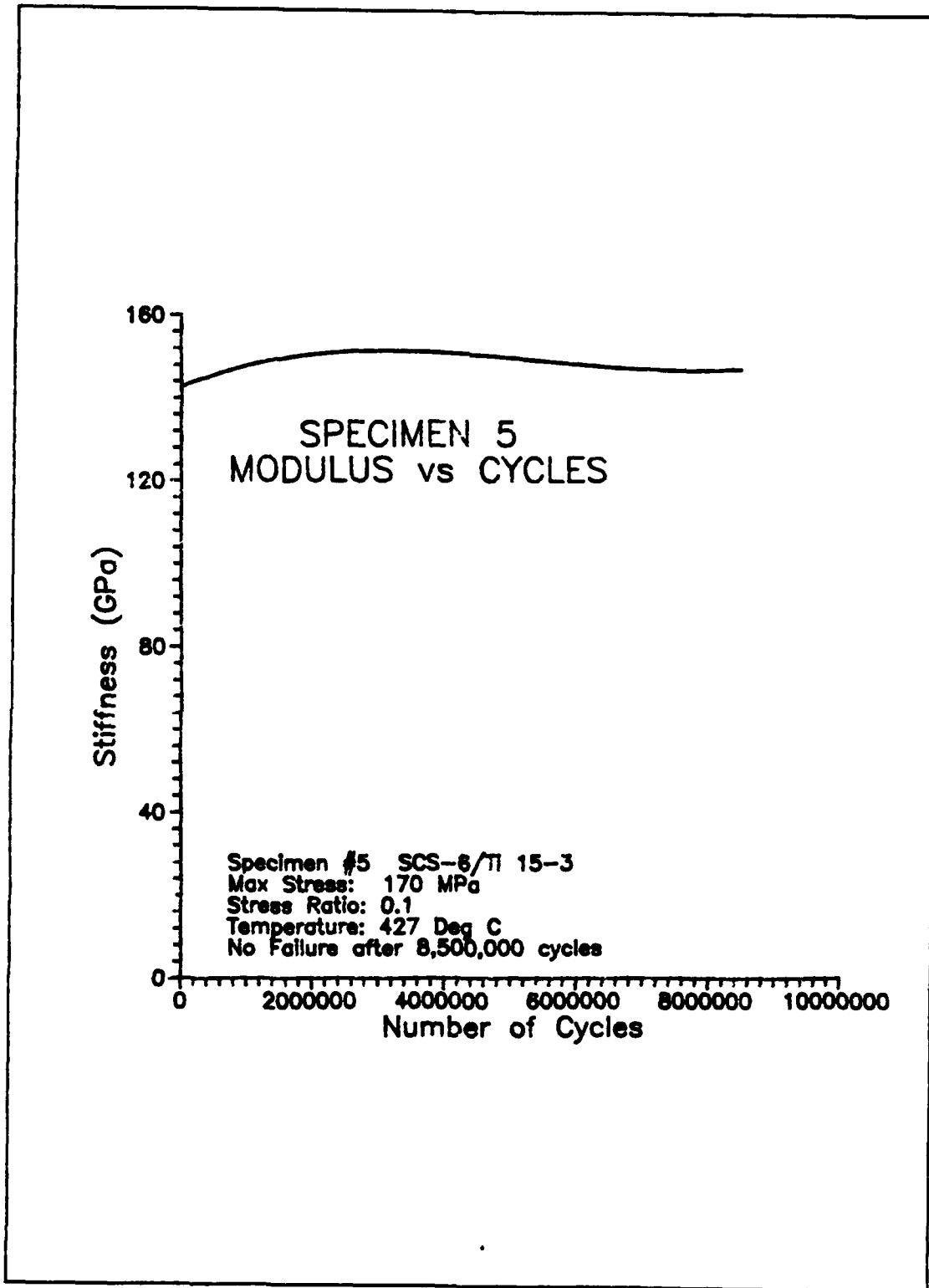


Figure 69: Specimen 5 (170 MPa) Modulus vs. Cycles

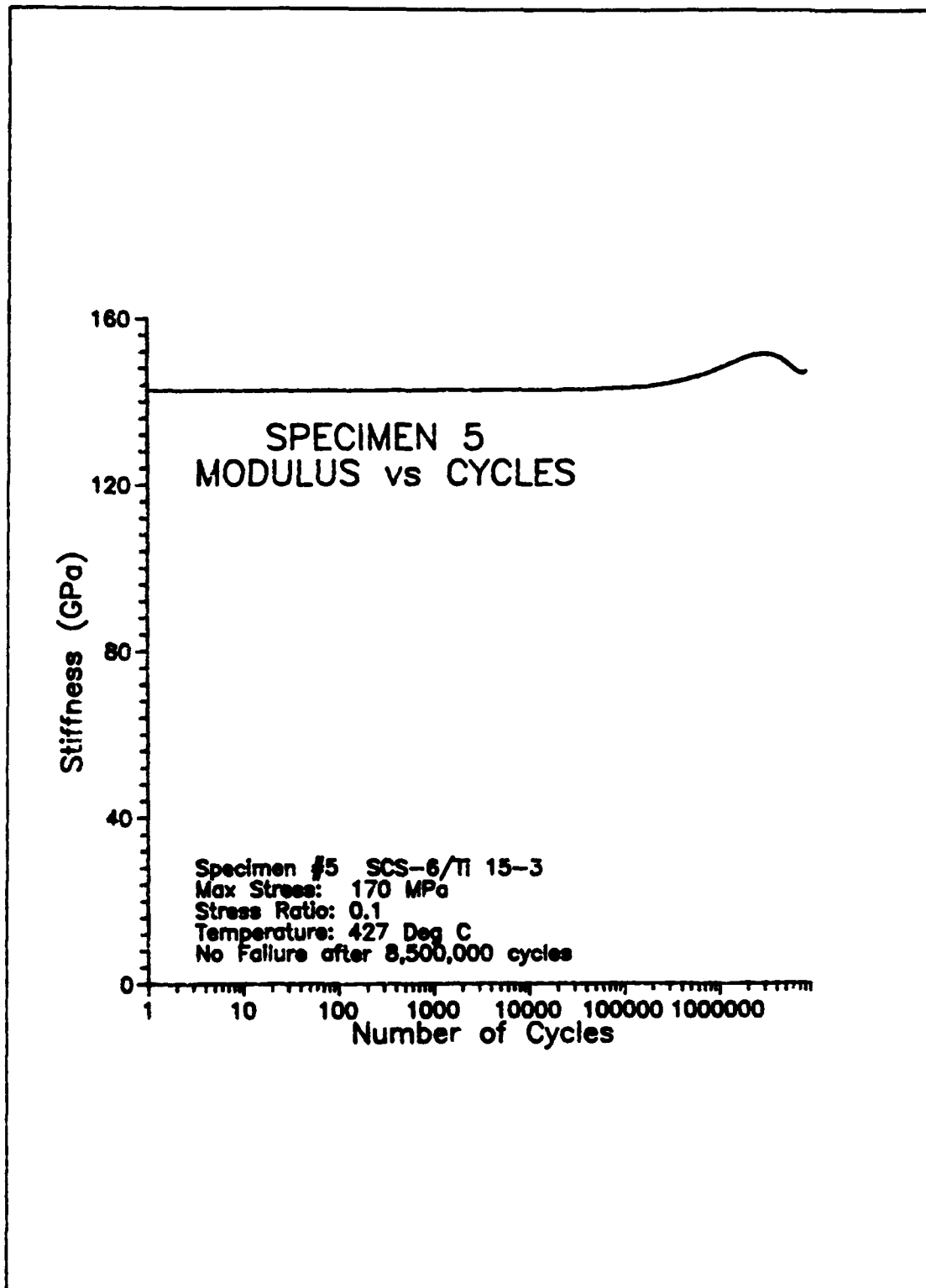


Figure 70: Specimen 5 (170 MPa) Modulus vs. Log Cycles

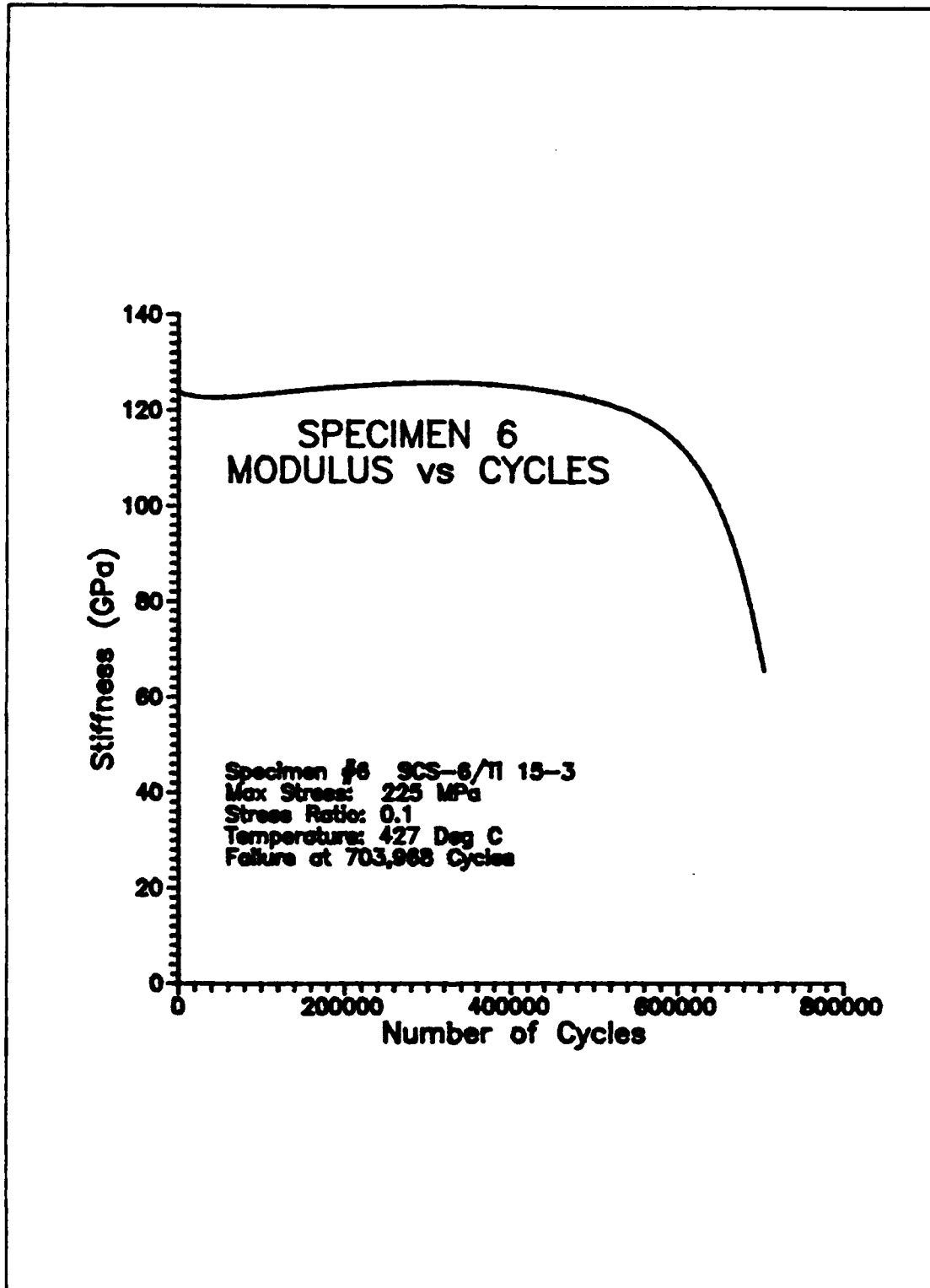


Figure 71: Specimen 6 (225 MPa) Modulus vs. Cycles

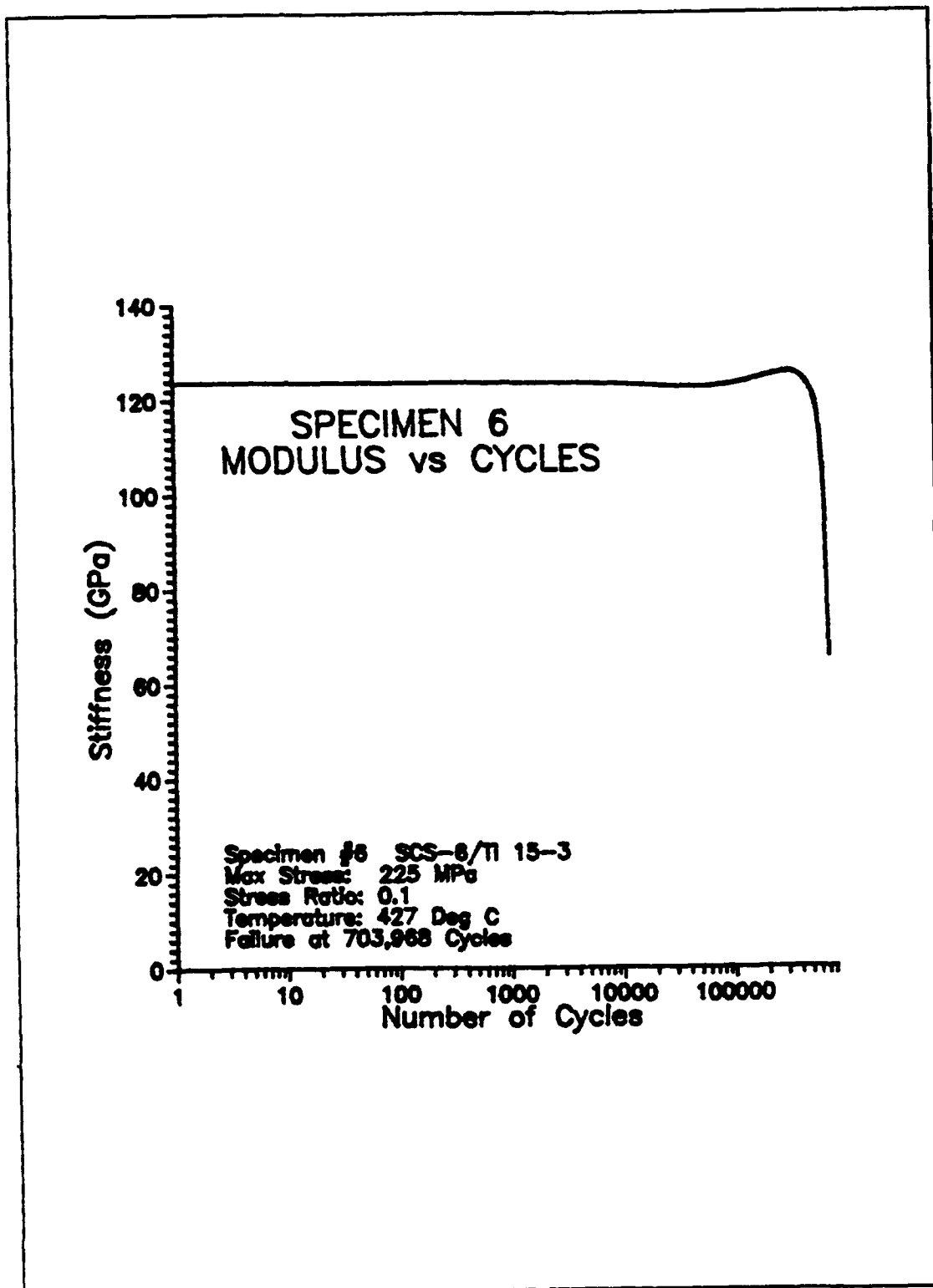


Figure 72: Specimen 6 (225 MPa) Modulus vs. Log Cycles

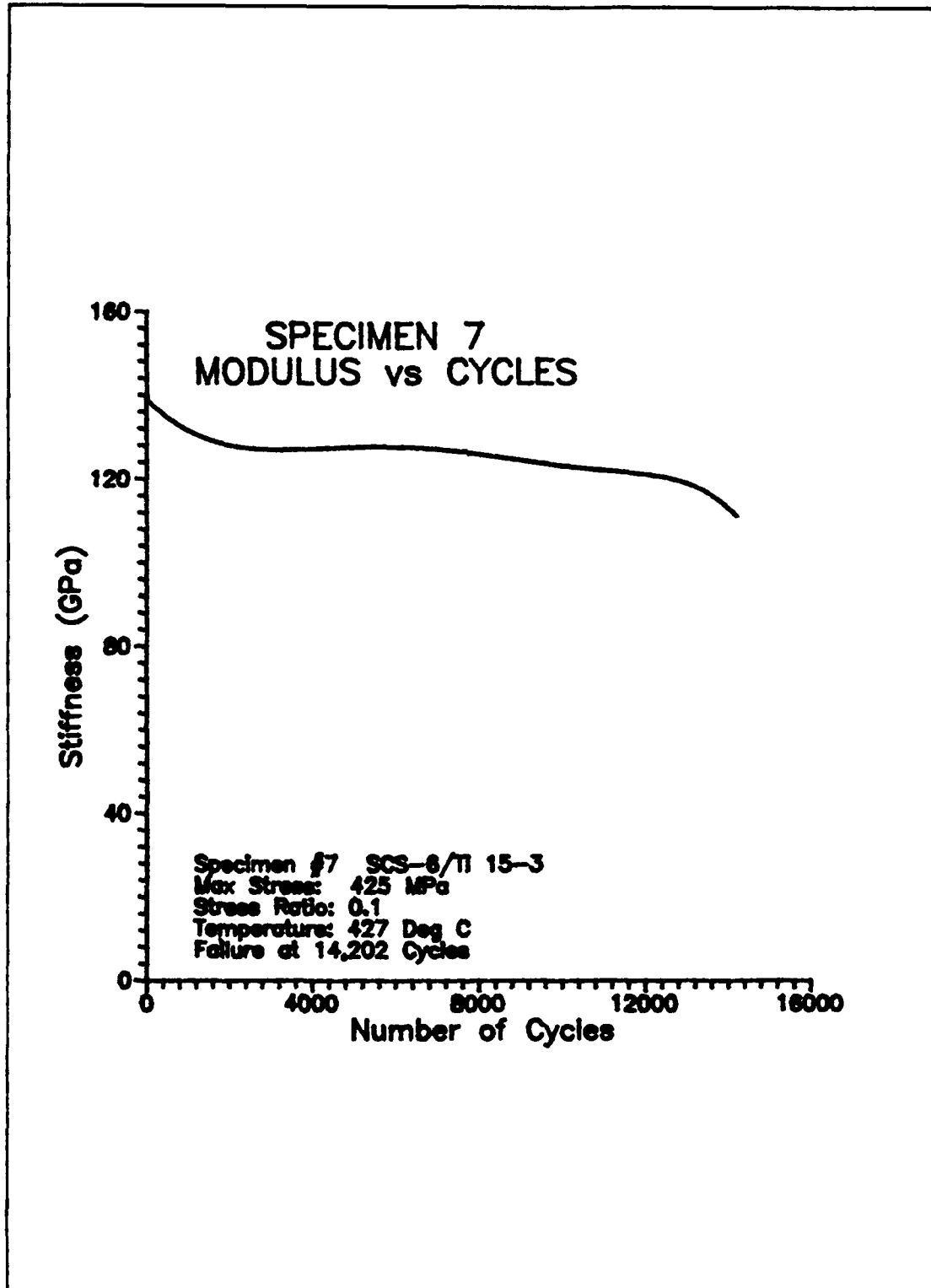


Figure 73: Specimen 7 (425 MPa) Modulus vs. Cycles

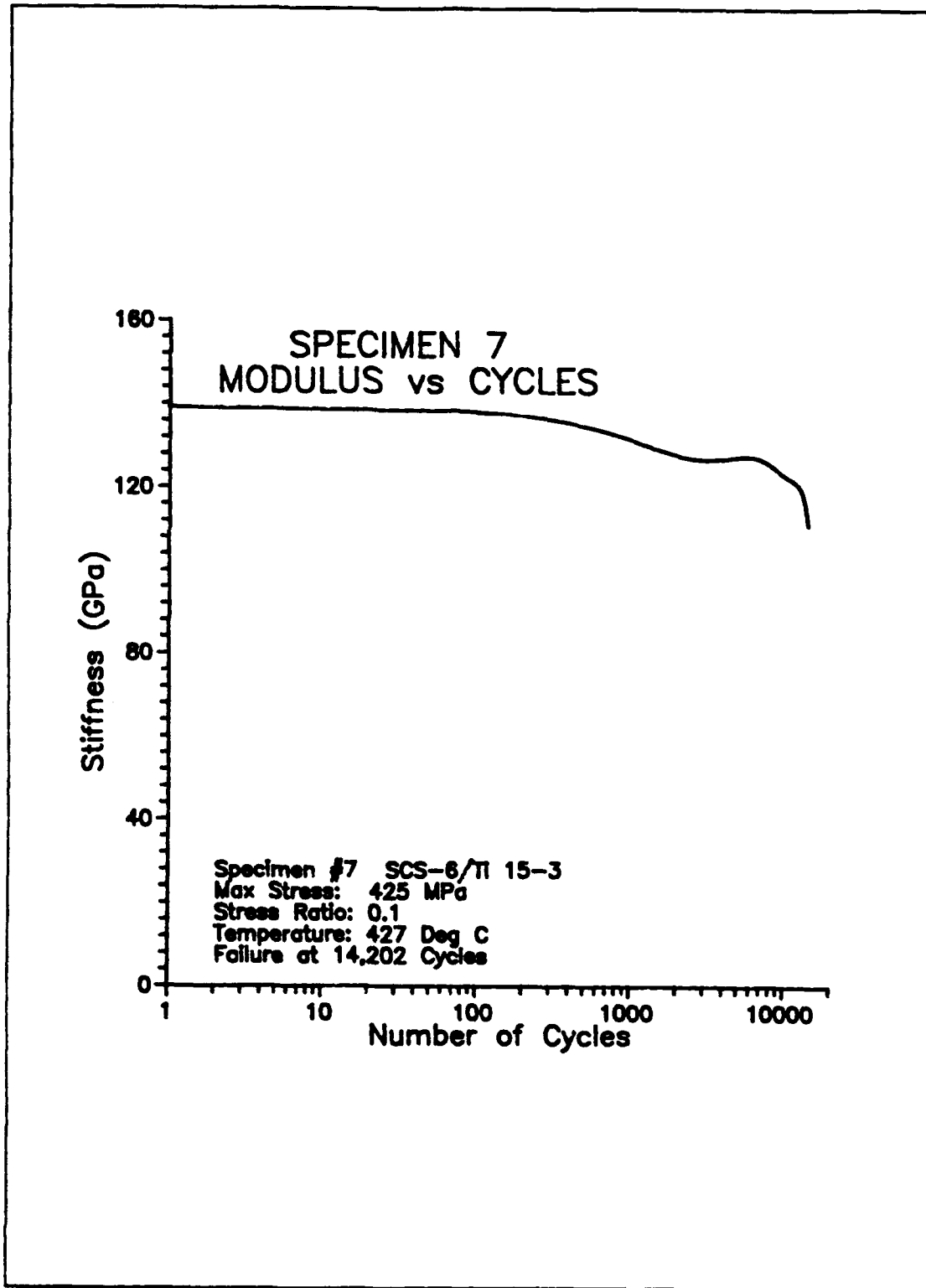


Figure 74: Specimen 7 (425 MPa) Modulus vs. Log Cycles

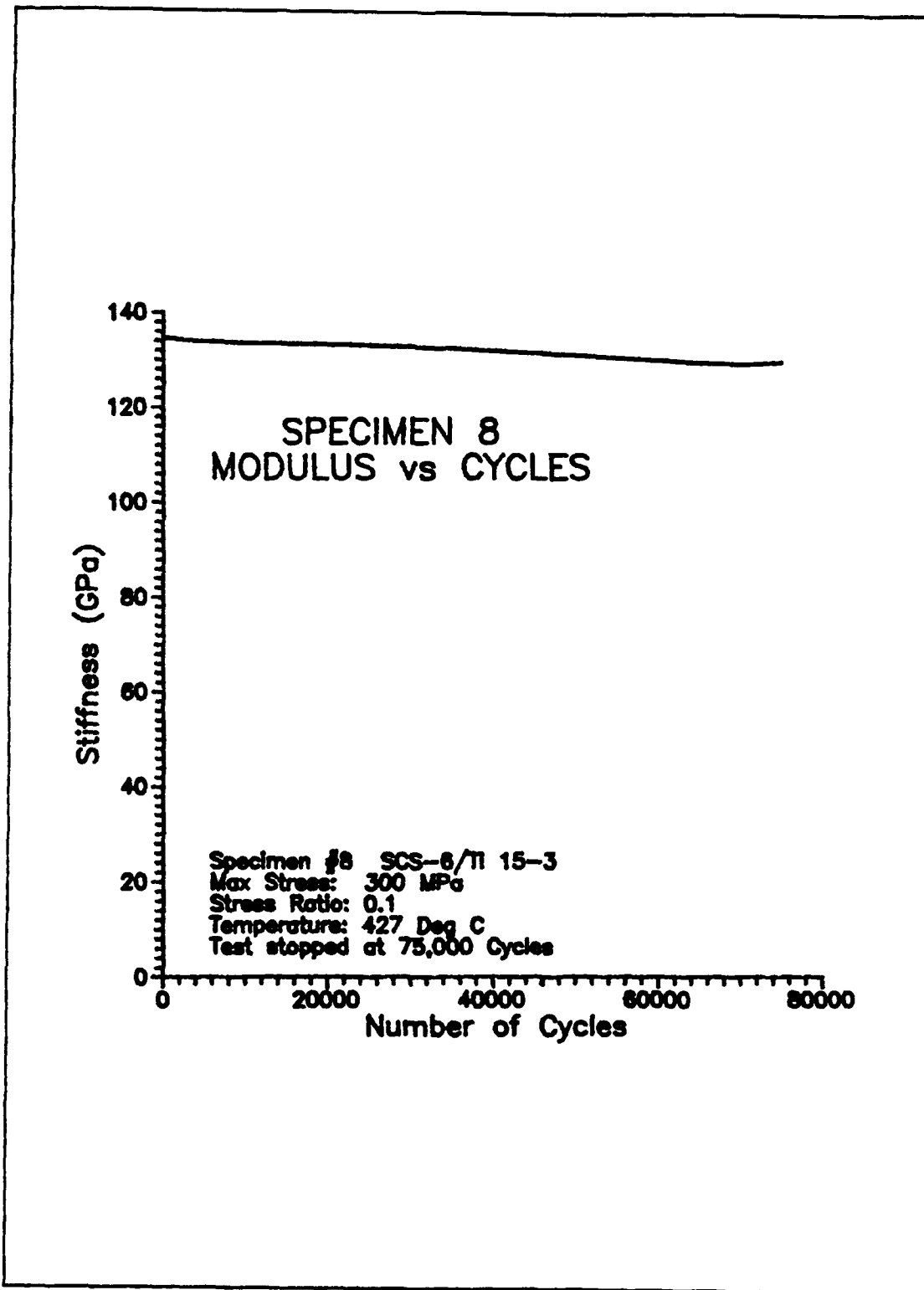


Figure 75: Specimen 8 (300 MPa) Modulus vs. Cycles

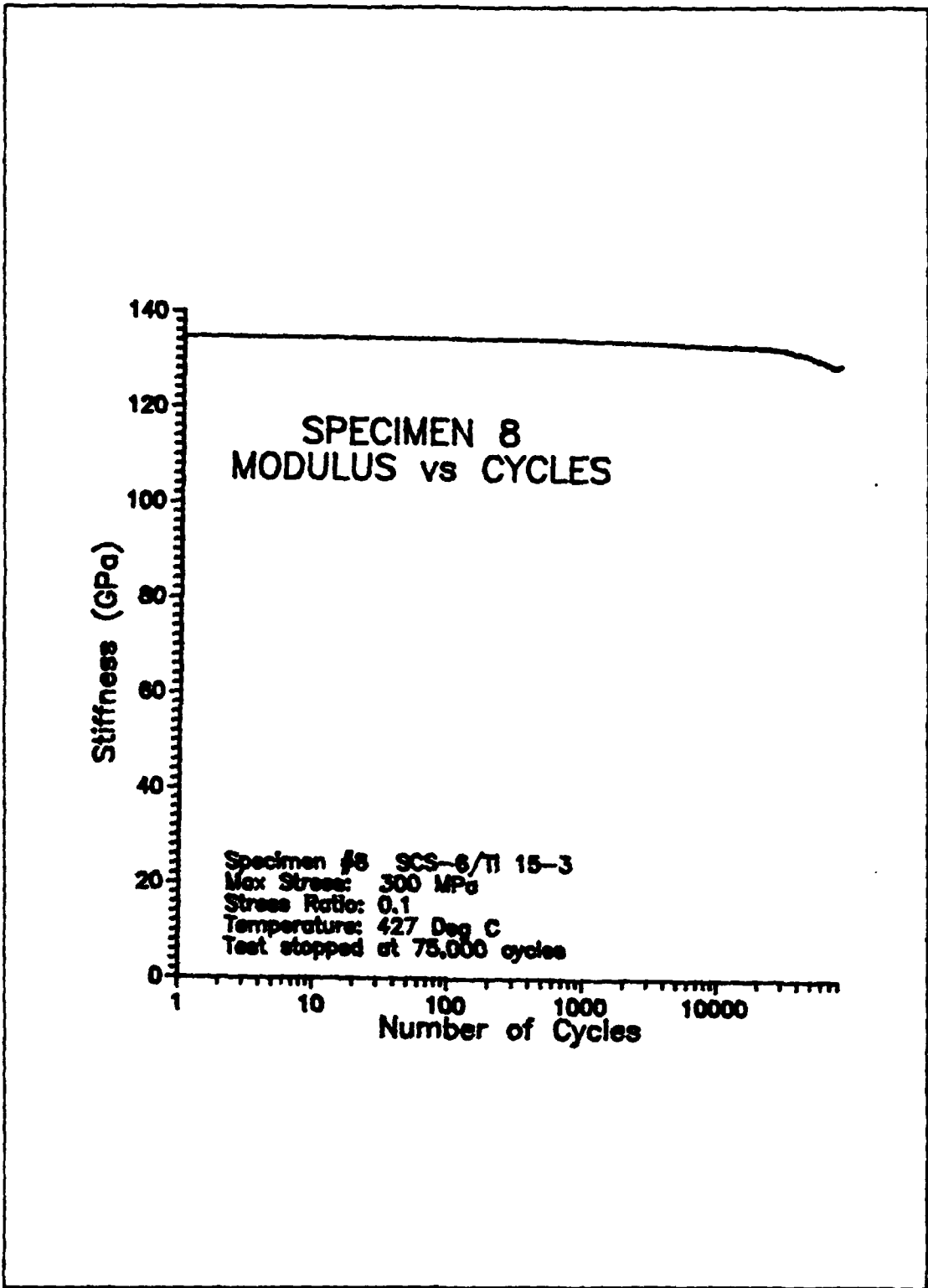


Figure 76: Specimen 8 (300 MPa) Modulus vs. Log Cycles

Appendix 3

METCAN Databank and Input file

Input file

```
DATAFILE FOR UNIT LOAD OF 100 MPa, ISOTHERMAL
$
$ Metcan Data File for Unit Load of 100 MPa
$ Isothermal Loading
$
$ No postprocessing file requested
  POST      F
LDDIST      F
$ Ply configuration details
  PLY       1       1       0.0       0.00868
  PLY       2       1       90.0       0.00868
  PLY       3       1       0.0       0.00868
  PLY       4       1       90.0       0.00868
  PLY       5       1       90.0       0.00868
  PLY       6       1       0.0       0.00868
  PLY       7       1       90.0       0.00868
  PLY       8       1       0.0       0.00868
$ Material Details
MATCRD      1      .370      .0      SCS6TI15
$ No cyclic degradation effects
CYCLES      .1E+01      1.
$ Output requests
$ PRINT FLINDEX Output request for failure index (Option 5)
$ PRINT STRSTRN Output request for stress/strain law (Option 6)
$ PRINT PROPCOM Output request for composite properties (Option 7)
  PRINT CONSTI Output request for constitutive relation (Option 8)
$ PRINT REDSTIF Output request for reduced d&a stiffness (Option 9)
$ PRINT FEMDATA Output request for f.e.a. data (Option 10)
$ PRINT DISPFOR Output request for Force/Disp relations (Option 11)
$ PRINT PLYRESP Output request for Ply Response/Prop (Option 12)
  PRINT PLYSTRS Output request for ply stresses/strains (Option 15)
  PRINT STRCON  Output request for stress conc. factors (Option 16)
  PRINT PROPREF Output request for reference properties (Option 26)
$ PRINT PROPCUR Output request for current properties (Option 27)
  PRINT MICRO   Output request for current microstresses (Option 28)
  PRINT LDSTEP  Output request for load step details (Option 29)
$ PRINT ALL     Output request for Complete Results (Option 0)
$ PRINT NONE    No Output is requested (Option 99)
$ Print output for every five time/load steps
$PRINTOPT    5
$ Print output for the last step
$PRINTOPT    LAST
$ Print output for all steps
$PRINTOPT    ALL
$ Note that "PRINTOPT" card is optional; Default is full print report
$-----
$-----
$ Interface details
INTRFACE    0      .05
$-----
$-----
$ Simplified Table Input; NSEG = 7
TMLOAD      -7
$-----
$-----
$ Start time, End time, No. of increments
$ (Manufacturing Cool Down, No Load)
  0.0 3600.      1
$ Temperature in each ply at the beginning of process
1832. 1832. 1832. 1832. 1832. 1832. 1832.
$ Temperature at the end; Cool down to Room Temperature
  70. 70. 70. 70. 70. 70. 70.
$ Mechanical Loads at the beginning
  0.0
$ Mechanical Loads at the end
  0.0
```

```

$-----
$-----
$ Process ends; Bring to constant elevated temperature
3600. 3660. 1
$ Temperature in each ply at 3600 sec
70. 70. 70. 70. 70. 70. 70. 70.
$ Temperature in each ply at 3660 sec
800. 800. 800. 800. 800. 800. 800. 800.
$ Mechanical Loads at 3600 sec
0. 0. 0. .0 0.0 0.0 0.0 0.0 00.
$ Mechanical Loads at 3660 sec
0. 0. 0. .00 0.0 0.0 0.0 0.0 00.
$-----
$-----
$ Increase load to minimum level
3660. 3684. 1
$ Temperature in each ply at 3660 sec
800. 800. 800. 800. 800. 800. 800. 800.
$ Temperature in each ply at 3684 sec
800. 800. 800. 800. 800. 800. 800. 800.
$ Mechanical Loads at 3660 sec
0. 0. 0. .00 0.0 0.0 0.0 0.0 00.
$ Mechanical Loads at 3684 sec
100.7 0. 0. .00 0.0 0.0 0.0 0.0 00.
$-----
$-----
$ Increase load to maximum level (R=0.1)
3684. 3785. 1
$ Temperature in each ply at 3684 sec
800. 800. 800. 800. 800. 800. 800. 800.
$ Temperature in each ply at 3785 sec
800. 800. 800. 800. 800. 800. 800. 800.
$ Mechanical Loads at 3684 sec
100.7 0. 0. .00 0.0 0.0 0.0 0.0 00.
$ Mechanical Loads at 3785 sec
1006.6 0. 0. .00 0.0 0.0 0.0 0.0 00.
$-----
$-----
$ Decrease Load to minimum level (R = 0.1)
3785. 3786. 1
$ Temperature in each ply at 3785 sec
800. 800. 800. 800. 800. 800. 800. 800.
$ Temperature in each ply at 3786 sec
800. 800. 800. 800. 800. 800. 800. 800.
$ Mechanical Loads at 3785 sec
1006.6 0. 0. .00 0.0 0.0 0.0 0.0 00.
$ Mechanical Loads at 3786 sec
100.7 0. 0. .00 0.0 0.0 0.0 0.0 00.
$-----
$-----
$ Second Cycle - Increase load to maximum level
3786. 3787. 1
$ Temperature in each ply at 3786 sec
800. 800. 800. 800. 800. 800. 800. 800.
$ Temperature in each ply at 3787 sec
800. 800. 800. 800. 800. 800. 800. 800.
$ Mechanical Loads at 3786 sec
100.7 0. 0. .00 0.0 0.0 0.0 0.0 00.
$ Mechanical Loads at 3787 sec
1006.6 0. 0. .00 0.0 0.0 0.0 0.0 00.
$-----
$-----
$ Decrease Load to minimum level (R = 0.1)
3787. 3788. 1
$ Temperature in each ply at 3787 sec
800. 800. 800. 800. 800. 800. 800. 800.

```

\$	Temperature in each ply at 3788 sec								
	800.	800.	800.	800.	800.	800.	800.	800.	
\$	Mechanical Loads at 3787 sec								
1006.6	0.	0.	.00	0.0	0.0	0.0	0.0	0.0	00.
\$	Mechanical Loads at 3788 sec								
100.7	0.	0.	.00	0.0	0.0	0.0	0.0	0.0	00.
\$-----									
\$-----									

End of data

Databank

P100 HIGH MODULUS GRAPHITE FIBER. DEC 16, 1987. (2)

FP 10000 0.390E-03 0.780E-01 0.660E+04
 FE 0.105E 09 0.900E 06 0.200E 00 0.250E 00 0.110E 07 0.700E 06
 FT -0.900E-06 0.560E-05 0.250E 02 0.174E 01 0.170E 00
 FS 0.325E 06 0.200E 06 0.250E 05 0.250E 05 0.250E 05 0.125E 05
 SIGF0 0.0 0.0 0.0 0.0 0.0 0.0 0.0 0.0 0.0
 DOTF0 0.0 0.0 0.0 0.0 0.0 0.0 0.0 0.0 0.0
 EXPONENTS +0.00 +0.00 +0.00 +0.00 +0.00 +0.00 +0.00 +0.00 +0.00
 EXPONENTS +0.00 +0.00 +0.00 +0.00 +0.00 -0.10 +0.00 +0.00 +0.00
 EXPONENTS +0.00 +0.00 +0.00 +0.00 +0.00 +0.00 +0.00 +0.00 +0.00
 EXPONENTS +0.00

SICA SILICON CARBIDE ON ALUMINUM. SEPT 7, 1987. (6)

FP 1 0.560E-02 0.110E+00 0.270E+04
 FE 0.580E+08 0.580E+08 0.250E+00 0.250E+00 0.238E+08 0.238E+08
 FT 0.270E-05 0.270E-05 0.750E+00 0.750E+00 0.290E+00
 FS 0.500E+06 0.650E+06 0.500E+06 0.650E+06 0.300E+06 0.300E+06
 SIGF0 0.0 0.0 0.0 0.0 0.0 0.0 0.0 0.0 0.0
 DOTF0 0.0 0.0 0.0 0.0 0.0 0.0 0.0 0.0 0.0
 EXPONENTS +0.00 +0.00 +0.00 +0.00 +0.00 +0.00 +0.00 +0.00 +0.00
 EXPONENTS +0.00 +0.00 +0.00 +0.00 +0.00 +0.00 +0.00 +0.00 +0.00
 EXPONENTS +0.00 +0.00 +0.00 +0.00 +0.00 +0.00 +0.00 +0.00 +0.00
 EXPONENTS +0.00

SCS9 SCS9 SILICON CARBIDE FIBER

FP 1 0.310E-02 0.110E+00 0.270E+04
 FE 0.480E 08 0.480E 08 0.260E 00 0.260E 00 0.242E 08 0.242E 08
 FT 0.208E-05 0.208E-05 0.750E 00 0.750E 00 0.290E 00
 FS 0.418E 06 0.418E 06 0.418E 06 0.418E 06 0.250E 06 0.250E 06
 SIGF0 0.0 0.0 0.0 0.0 0.0 0.0 0.0 0.0 0.0
 DOTF0 0.0 0.0 0.0 0.0 0.0 0.0 0.0 0.0 0.0
 EXPONENTS +0.00 +0.00 +0.00 +0.00 +0.00 +0.00 +0.00 +0.00 +0.00
 EXPONENTS +0.00 +0.00 +0.00 +0.00 +0.00 +0.00 +0.00 +0.00 +0.00
 EXPONENTS +0.00 +0.00 +0.00 +0.00 +0.00 +0.00 +0.00 +0.00 +0.00
 EXPONENTS +0.00

SCS6 SCS6 SILICON CARBIDE FIBER

FP 1 0.551E-02 0.110E+00 0.487E+04
 FE 0.573E+08 0.573E+08 0.250E+00 0.250E+00 0.238E+08 0.238E+08
 FT 0.290E-05 0.290E-05 0.750E+00 0.750E+00 0.290E+00
 FS 0.500E+06 0.650E+06 0.500E+06 0.650E+06 0.300E+06 0.300E+06
 SIGF0 0.0 0.0 0.0 0.0 0.0 0.0 0.0 0.0 0.0
 DOTF0 0.0 0.0 0.0 0.0 0.0 0.0 0.0 0.0 0.0
 EXPONENTS +0.00 +0.00 +0.00 +0.00 +0.00 +0.00 +0.00 +0.00 +0.00
 EXPONENTS +0.00 +0.00 +0.00 +0.00 +0.00 +0.00 +0.00 +0.00 +0.00
 EXPONENTS +0.00 +0.00 +0.00 +0.00 +0.00 +0.00 +0.00 +0.00 +0.00
 EXPONENTS +0.00 +0.00 +0.00 +0.00 +0.00 +0.00 +0.00 +0.00 +0.00

OVER END OF FIBER PROPERTIES

ALT6 ALUMINUM MATRIX. DEC 16, 1987. (1)

MP 0.980E-01
 ME 0.100E 08 0.300E 00 0.131E-04
 MT 0.866E 01 0.230E 00
 MS 0.180E 05 0.180E 05 0.120E 05 0.300E 00 0.300E 00 0.300E 00 0.300E 00
 MV 0.019E 00 0.108E 04
 SIGM0 0.0 0.0 0.0 0.0 0.0 0.0 0.0 0.0
 SIGM0 0.0 0.0 0.0 0.0 0.0 0.0 0.0 0.0
 SIGM0 0.0 0.0 0.0 0.0 0.0 0.0 0.0 0.0
 DOTM0 0.0 0.0 0.0 0.0 0.0 0.0 0.0 0.0
 DOTM0 0.0 0.0 0.0 0.0 0.0 0.0 0.0 0.0
 DOTM0 0.0 0.0 0.0 0.0 0.0 0.0 0.0 0.0
 EXPONENTS +0.00 +0.00 +0.00 +0.00 +0.00 +0.00 +0.00 +0.00 +0.00
 EXPONENTS +0.00 +0.00 +0.00 +0.00 +0.00 +0.00 +0.00 +0.00 +0.00
 EXPONENTS +0.00 +0.00 +0.00 +0.00 +0.00 +0.00 +0.00 +0.00 +0.00
 EXPONENTS +0.00

TI15 TITANIUM MATRIX. AUG 25, 1988. (3)

MP 0.172E 00
 ME 0.109E 08 0.360E 00 0.540E-05
 MT 0.390E 00 0.120E 00
 MS 0.130E 06 0.130E 06 0.910E 05 0.120E 00 0.120E 00 0.120E 00 0.120E 00

```

MV 0.019E 00 0.300E 04
SIGMO 0.0 0.0 0.0 0.0 0.0 0.0 0.0 0.0 0.0
SIGMO 0.0 0.0 0.0 0.0 0.0 0.0 0.0 0.0 0.0
SIGMO 0.0 0.0 0.0 0.0 0.0 0.0 0.0 0.0 0.0
DOTMO 0.0 0.0 0.0 0.0 0.0 0.0 0.0 0.0 0.0
DOTMO 0.0 0.0 0.0 0.0 0.0 0.0 0.0 0.0 0.0
DOTMO 0.0 0.0 0.0 0.0 0.0 0.0 0.0 0.0 0.0
EXPONENTS +0.00 +0.00 +0.00 +0.00 +0.00 +0.00 +0.00 +0.00 +0.00 +0.00
EXPONENTS +0.00 +0.00 +0.00 +0.00 +0.00 +0.00 +0.00 +0.00 +0.17 +0.00
EXPONENTS +0.00 +0.00 +0.00 +0.00 +0.00 +0.00 +0.00 +0.00 +0.00 +0.00
EXPONENTS +0.00
COPR COPPER MATRIX. DEC 16, 1987. (4)
MP 0.320E+00
ME 0.177E+08 0.300E 00 0.980E-05
MT 0.193E 02 0.090E 00
MS 0.320E 05 0.320E 05 0.190E 05 0.350E 00 0.350E 00 0.350E 00 0.350E 00
MV 0.019E 00 0.198E 04
SIGMO 0.0 0.0 0.0 0.0 0.0 0.0 0.0 0.0 0.0
SIGMO 0.0 0.0 0.0 0.0 0.0 0.0 0.0 0.0 0.0
SIGMO 0.0 0.0 0.0 0.0 0.0 0.0 0.0 0.0 0.0
DOTMO 0.0 0.0 0.0 0.0 0.0 0.0 0.0 0.0 0.0
DOTMO 0.0 0.0 0.0 0.0 0.0 0.0 0.0 0.0 0.0
DOTMO 0.0 0.0 0.0 0.0 0.0 0.0 0.0 0.0 0.0
EXPONENTS +0.00 +0.00 +4.00 +0.00 +0.00 +0.00 +0.00 +0.00 +0.00 +0.00
EXPONENTS +0.00 +0.00 +0.00 +0.00 +0.00 +0.00 -0.10 +0.00 +0.00 +0.00
EXPONENTS +0.00 +0.00 +0.00 +0.00 +0.00 +0.00 +0.00 +0.00 +0.00 +0.00
EXPONENTS +0.00
B21S BETA 21S METAL MATRIX
MP 0.178E+00
ME 0.162E+08 0.300E 00 0.528E-05
MT 0.814E 00 0.142E 00
MS 0.167E 06 0.190E 06 0.850E 05 0.070E 00 0.020E 00 0.050E 00 0.050E 00
MV 0.019E 00 0.165E 04
SIGMO 0.0 0.0 0.0 0.0 0.0 0.0 0.0 0.0 0.0
SIGMO 0.0 0.0 0.0 0.0 0.0 0.0 0.0 0.0 0.0
SIGMO 0.0 0.0 0.0 0.0 0.0 0.0 0.0 0.0 0.0
DOTMO 0.0 0.0 0.0 0.0 0.0 0.0 0.0 0.0 0.0
DOTMO 0.0 0.0 0.0 0.0 0.0 0.0 0.0 0.0 0.0
DOTMO 0.0 0.0 0.0 0.0 0.0 0.0 0.0 0.0 0.0
EXPONENTS +0.00 +0.00 +0.00 +0.00 +0.00 +0.00 +0.00 +0.00 +0.00 +0.00
EXPONENTS +0.00 +0.00 +0.00 +0.00 +0.00 +0.00 +0.00 +0.00 +0.00 +0.00
EXPONENTS +0.00 +0.00 +0.00 +0.00 +0.00 +0.00 +0.00 +0.00 +0.00 +0.00
EXPONENTS +0.00
OVER END OF MATRIX PROPERTIES.
INTERFACE WITH 5 % OF FIBER DIAMETER THICKNESS (1)
DP 0.190E+00 0.510E-01
DE 0.170E 07 0.300E 00 0.500E-05
DT 0.190E 01 0.010E 00
DS 0.300E 04 0.300E 04 0.180E 04 0.300E 00 0.300E 00 0.300E 00 0.300E 00
DV 0.019E 00 0.429E 04
SIGD0 0.0 0.0 0.0 0.0 0.0 0.0 0.0 0.0 0.0
SIGD0 0.0 0.0 0.0 0.0 0.0 0.0 0.0 0.0 0.0
DOTD0 0.0 0.0 0.0 0.0 0.0 0.0 0.0 0.0 0.0
DOTD0 0.0 0.0 0.0 0.0 0.0 0.0 0.0 0.0 0.0
EXPONENTS +0.00 +0.00 +0.00 +0.00 +0.00 +0.00 +0.00 +0.00 +0.00 +0.00
EXPONENTS +0.00 +0.00 +0.00 +0.00 +0.00 +0.00 +0.00 +0.00 +0.00 +0.00
EXPONENTS +0.00 +0.00 +0.00 +0.00 +0.00 +0.00 +0.00 +0.00 +0.00 +0.00
EXPONENTS +0.00
INTERFACE WITH 10 % OF FIBER DIAMETER THICKNESS (2)
DP 0.190E+00 0.100E 00
DE 0.400E 08 0.300E 00 0.500E-05
DT 0.100E 02 0.130E 00
DS 0.150E 05 0.150E 05 0.100E 05 0.300E 00 0.300E 00 0.300E 00 0.300E 00
DV 0.019E 00 0.350E 04
SIGD0 0.0 0.0 0.0 0.0 0.0 0.0 0.0 0.0 0.0
SIGD0 0.0 0.0 0.0 0.0 0.0 0.0 0.0 0.0 0.0

```

DOTDO	0.0		0.0		0.0		0.0		0.0		0.0	0.0
DOTDO	0.0		0.0		0.0		0.0		0.0		0.0	
EXPONENTS	+0.00	+0.00	+0.00	+0.00	+0.00	+0.00	+0.00	+0.00	+0.00	+0.00	+0.00	
EXPONENTS	+0.00	+0.00	+0.00	+0.00	+0.00	+0.00	+0.00	+0.00	+0.00	+0.00	+0.00	
EXPONENTS	+0.00	+0.00	+0.00	+0.00	+0.00	+0.00	+0.00	+0.00	+0.00	+0.00	+0.00	
EXPONENTS	+0.00											

Appendix 4

Derivation of Critical Crack Length Expression

The following derivation is based upon the geometry depicted in figure 28 and simple strength of materials principles. Pertinent dimensions used are the width, w ; hole diameter, d ; and the thickness, t . Material properties involved are the fiber volume fraction, V_f , and the ultimate strength of the composite (at test conditions), σ_{ult} . Only one test parameter is involved; it is the stress level of the current test, σ_{test} .

Stress in the reduced cross-section is given by:

$$\sigma_{test} = \frac{P}{t(w-d)} \quad (7)$$

Stress corresponding to the ultimate strength of the material (once cracks have formed) is given by:

$$\sigma_{ult} = \frac{P}{t(w-d-2L_c(1-V_f))} \quad (8)$$

Here all quantities are known except for L_c . Solve for L_c to get:

$$L_c = \frac{w-d - \frac{P}{t\sigma_{ult}}}{2(1-V_f)} \quad (9)$$

The load level, P , is not explicitly known but may be found by solving equation (7) for P as shown below.

$$P = (w-d) t \sigma_{test} \quad (10)$$

This result is then substituted in to equation (9) giving:

$$L_c = \frac{w-d - \frac{(w-d) t \sigma_{test}}{t \sigma_{ult}}}{2(1-V_f)} \quad (11)$$

Simplification leads to :

$$L_c = \frac{(w-d) \left(1 - \frac{\sigma_{test}}{\sigma_{ult}}\right)}{2(1-V_f)} \quad (12)$$

To account for the percentage of fibers intact behind the crack front, a coefficient, β , is introduced. This leads to:

$$L_c = \frac{(w-d) \left(1 - \frac{\sigma_{test}}{\sigma_{ult}}\right)}{2(1-\beta V_f)} \quad (13)$$

To find β experimentally, measure the critical crack length which is the distance from the edge of the hole to the brittle/ductile transition then use it in equation (14) below

$$\beta = \frac{1 - \frac{(w-d) \left(1 - \frac{\sigma_{test}}{\sigma_{ult}}\right)}{2L_c}}{V_f} \quad (14)$$

Appendix 5

First Cycle Stress vs. Strain Curves

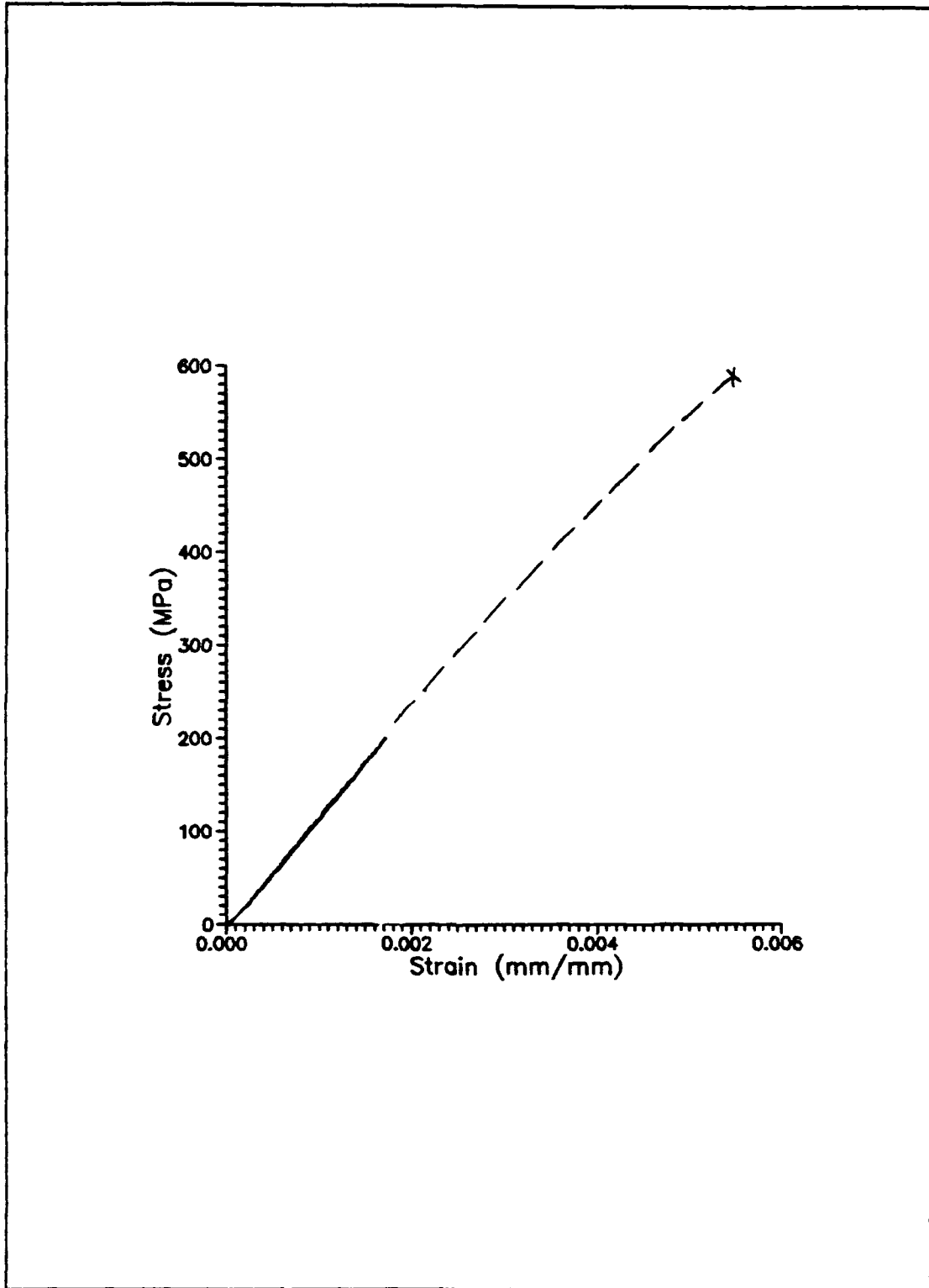


Figure 77: Specimen 2 (240 MPa) Stress vs. Strain

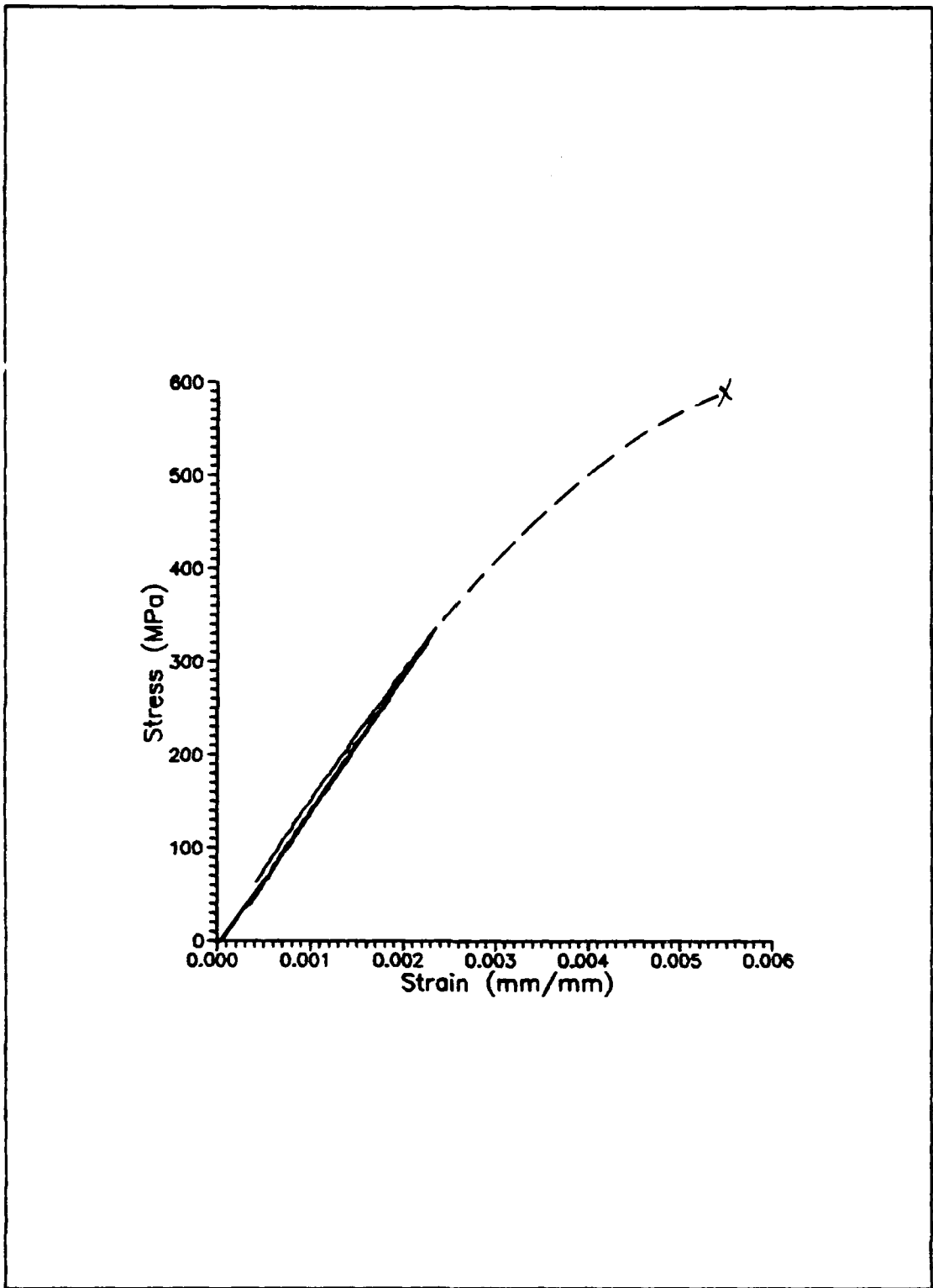


Figure 78: Specimen 3 (400 MPa) Stress vs. Strain

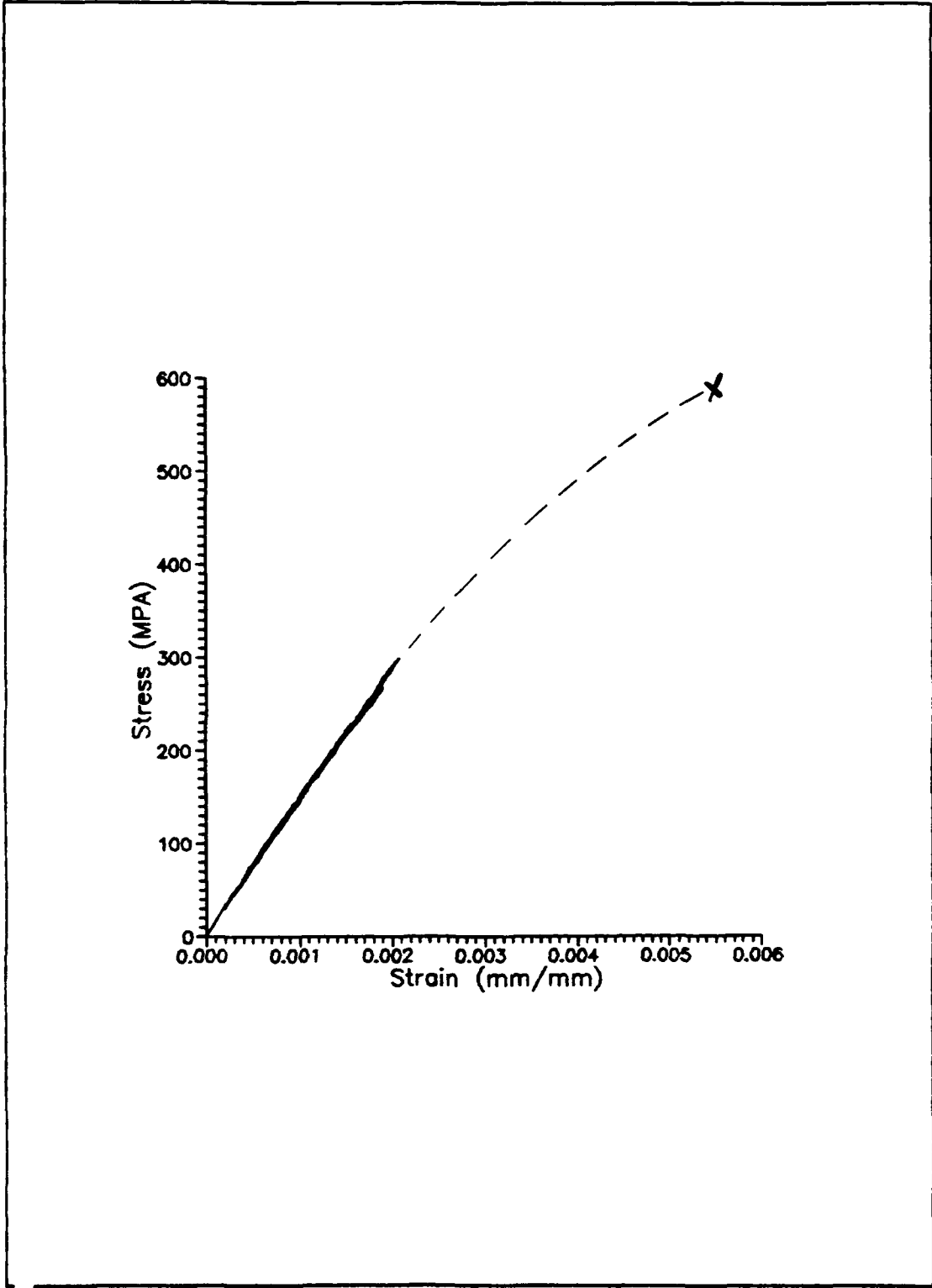


Figure 79: Specimen 4 (300 MPa) Stress vs. Strain

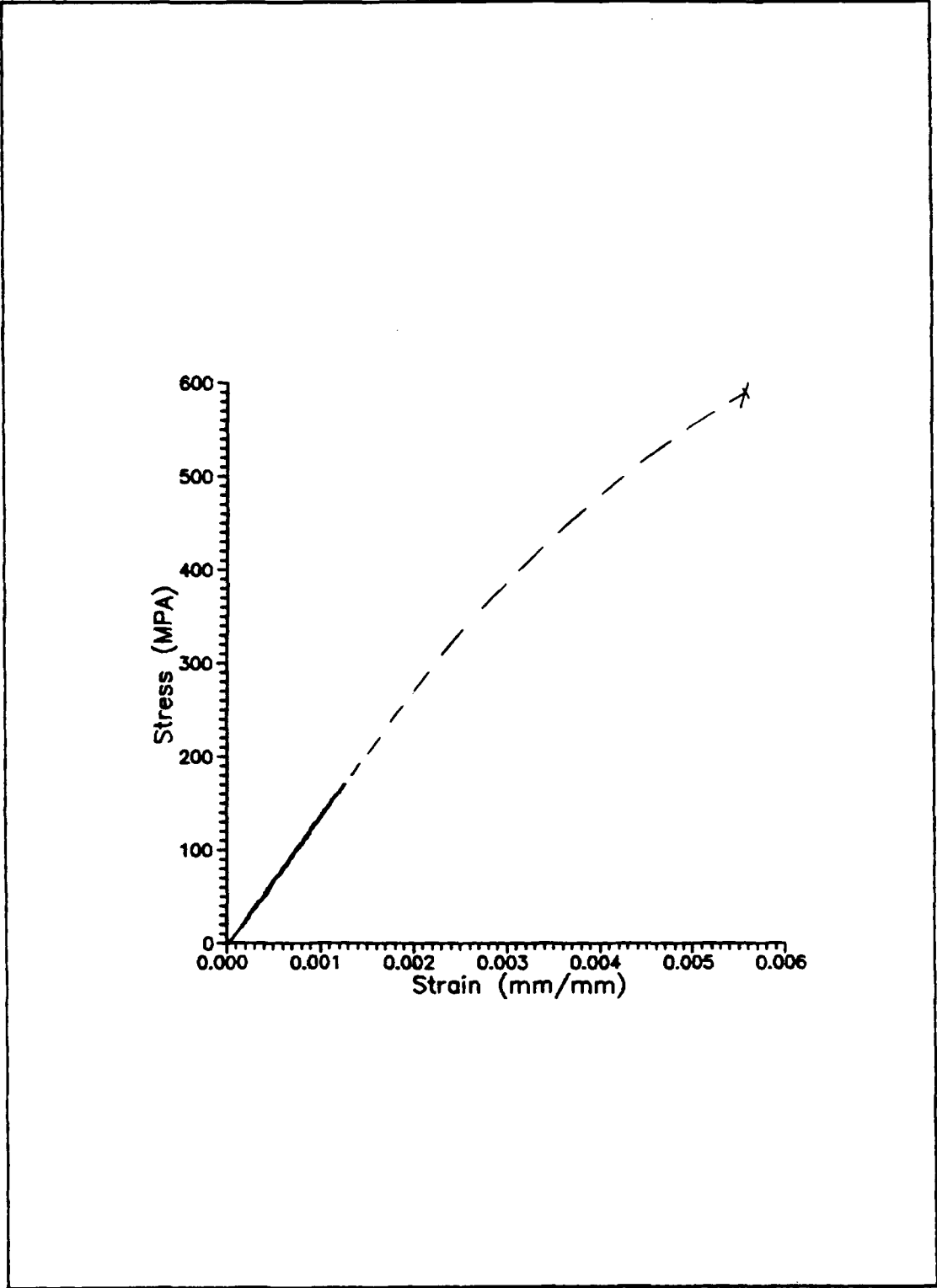


Figure 80: Specimen 5 (170 MPa) Stress vs. Strain

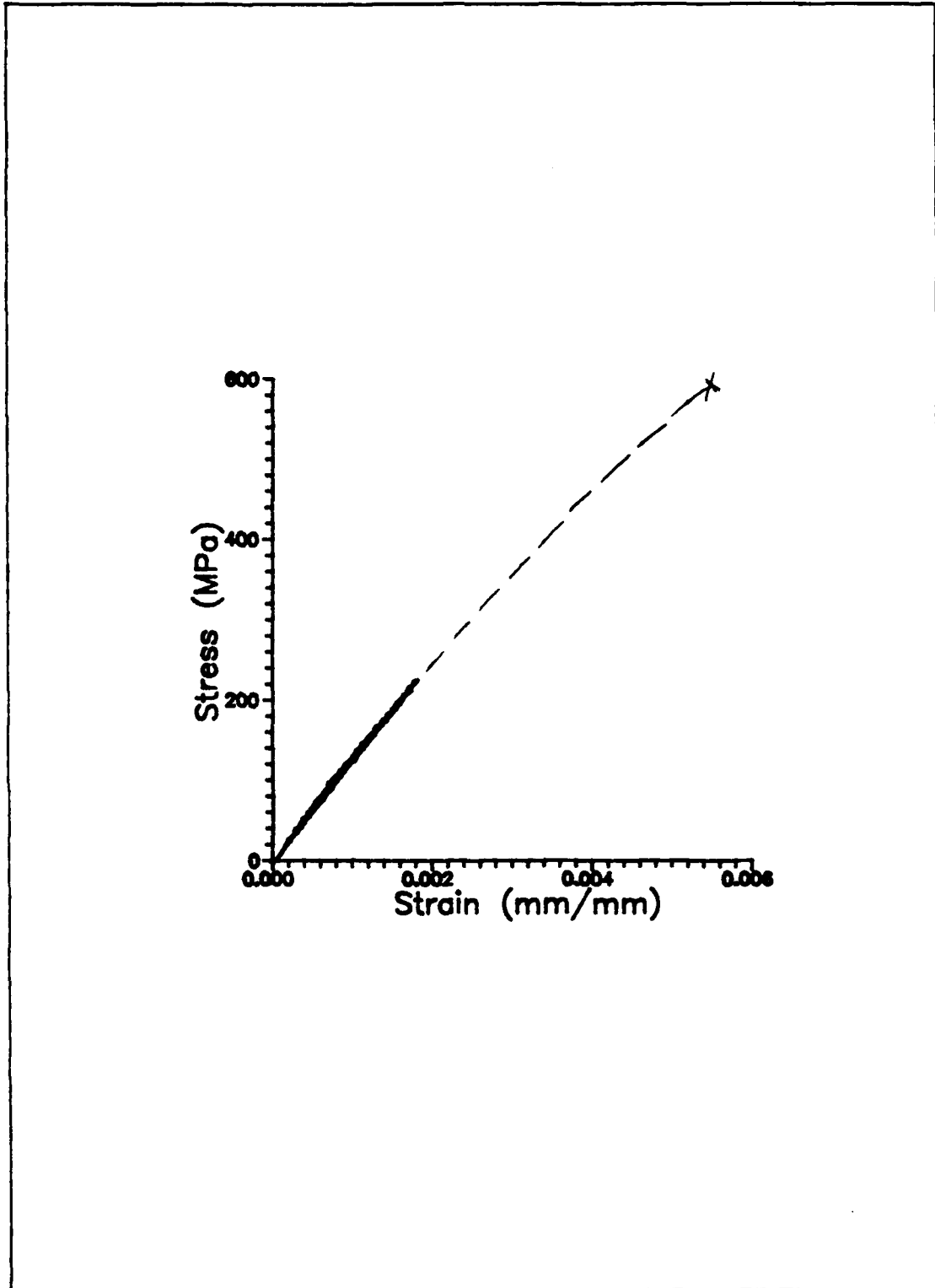


Figure 81: Specimen 6 (225 MPa) Stress vs. Strain

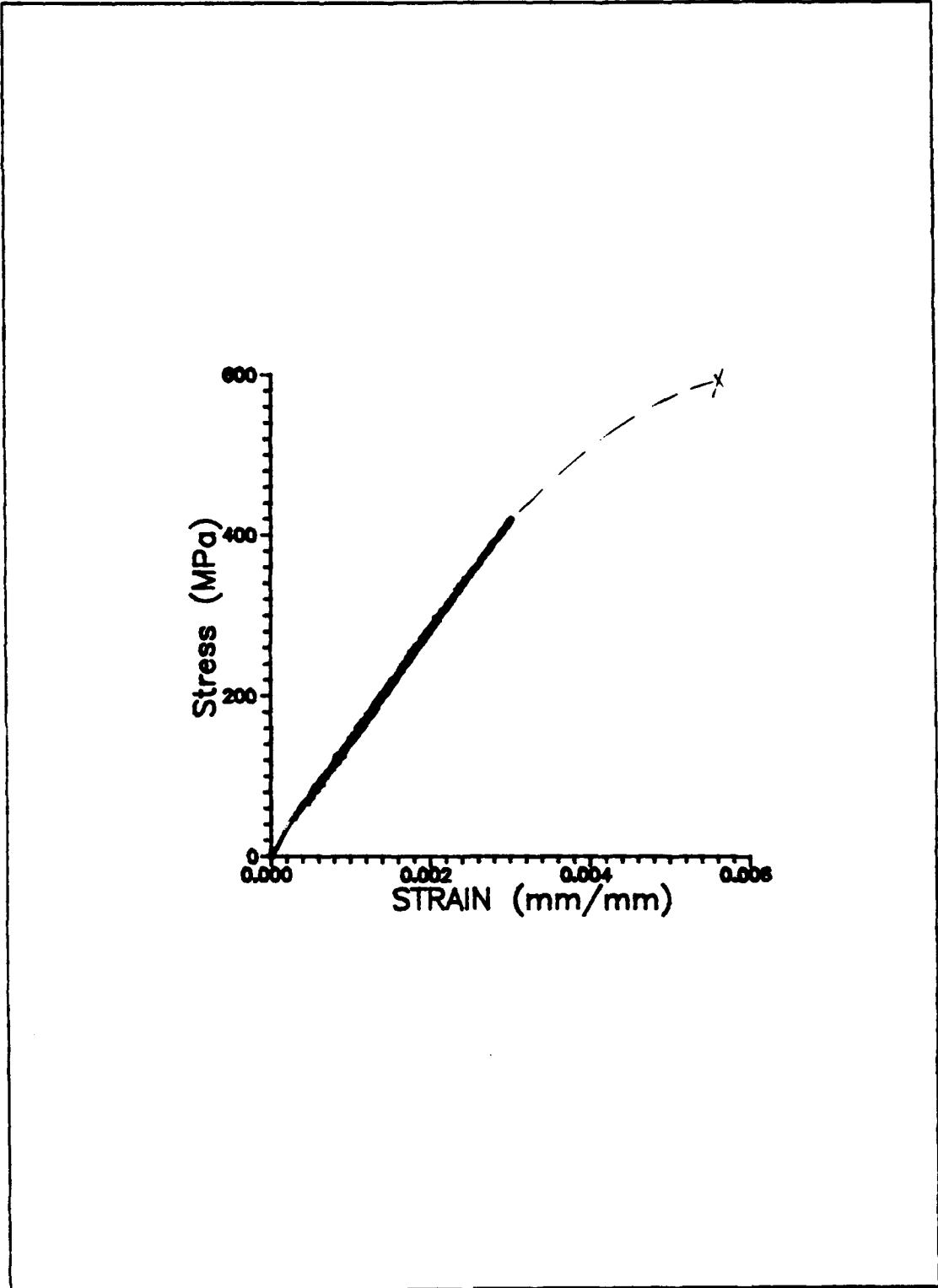


Figure 82: Specimen 7 (425 MPa) Stress vs. Strain

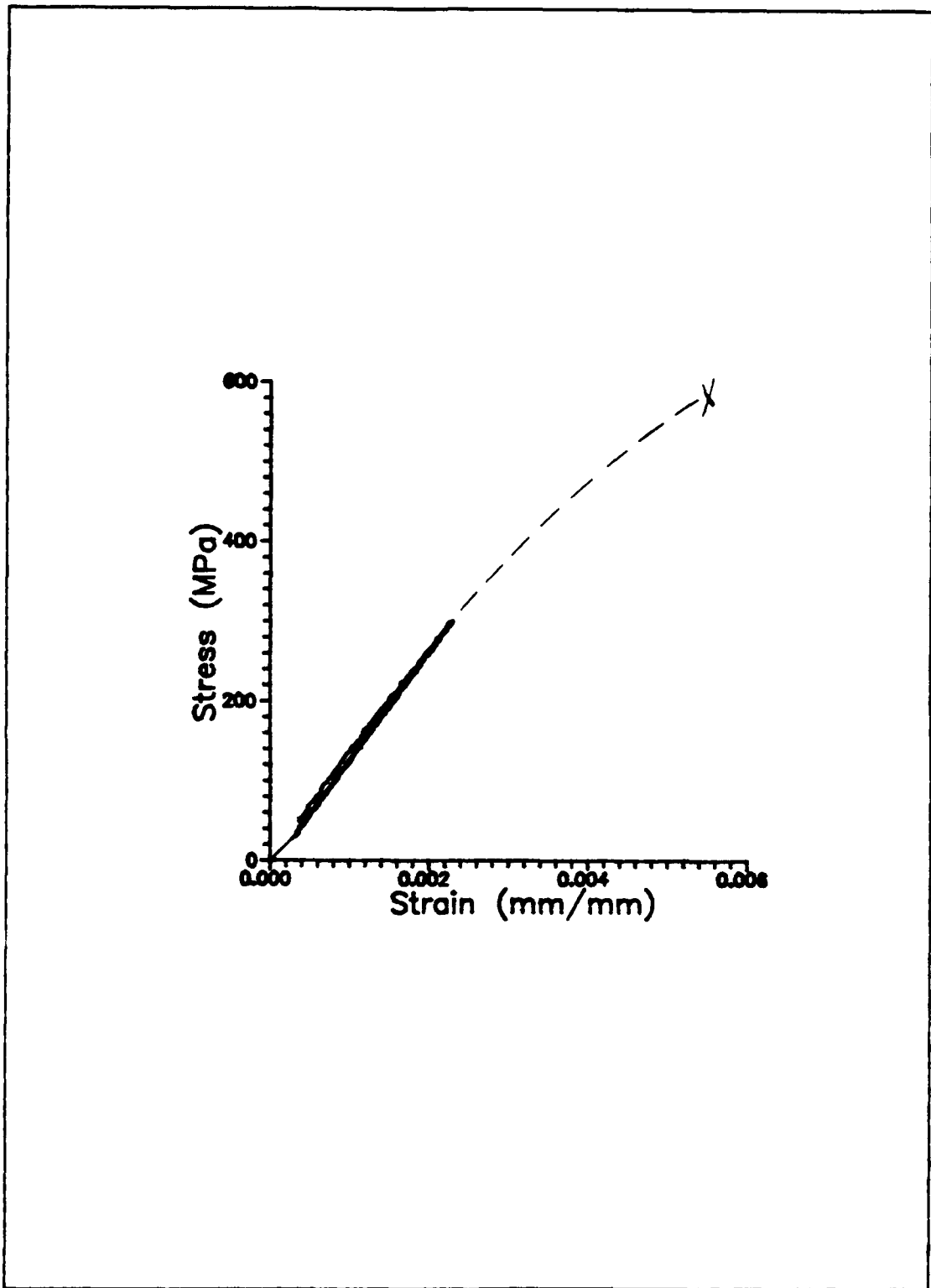


Figure 83: Specimen 8 (300 MPa) Stress vs. Strain

Bibliography

1. Agarwal, Bagwan D. and Broutman, Lawrence. *Analysis and Performance of Fiber Composites*. New York: Wiley-Interscience, 1990.
2. Bahei-El-Din, Y.A. and Dvorak, G.J., "Plasticity Analysis of Laminated Composite Plates," *Journal of Applied Mechanics*, 49:740-746 (December 1982).
3. Bakuckas Jr, J.G., Johnson, W.S., and Bigelow, C.A., "Fatigue Damage in Cross-Ply Titanium Metal Matrix Composites Containing Center Holes," Submitted to *Journal of Engineering Materials and Technology*. NASA Langley Research Center, Hampton VA, 1991.
4. Bigelow, C.S., and Johnson, W.S., *Effect of Fiber-Matrix Debonding on Notched Strength of Titanium Metal Matrix Composites*. NASA TM 104131. NASA Langley Research Center, 1991.
5. *Eshbach's Handbook of Engineering Fundamentals* (Fourth Edition). Byron D. Tapley, Ed., New York: Wiley-Interscience, 1990.
6. Flinn, R.A. and Trojan, P.K., *Engineering Materials and Their Application* (Second Edition). Hopewell, New Jersey: Houghton Mifflin, 1981.
7. Gabb, T.P., Gayda, J., Lerch, B.A., and Halford, G.R., "The Effect of Matrix Mechanical Properties on [0], Unidirectional SiC/Ti Composite Fatigue Resistance," *Scripta Metallurgica et Materialia*, 25:2879-2884 (December 1991).
8. Gayda, J., Gabb, T.P., and Freed A.D. "The Isothermal Fatigue Behavior of a Unidirectional SiC/Ti Composite and the Ti Alloy Matrix," *Fundamental Relationships Between Microstructure and Mechanical Properties of Metal Matrix Composites*, P.K. Liaw and M.N. Gungor, Eds., The Minerals, Metals, and Materials Society, 1990, pp 497-514.
9. Greszczuk, L.B., "Stress Concentrations and Failure Criteria for Orthotropic and Anisotropic Plates with Circular Openings," *Composite Materials: Testing and Design (Second Conference)*, ASTM STP 497, American Society for Testing and Materials, 1972, pp 363-381.

10. Hillberry, B.M. and Johnson, W.S. "Matrix Fatigue Crack Development in a Notched Continuous Fiber SCS-6/Ti 15-3 Composite," *Symposium on Microcracking Induced Damage in Composites*, ASME Winter Annual Meeting, Dallas TX, November 26-28 1990, pp 121-127.
11. Hillberry, B.M., and Johnson, W.S., *Prediction of Matrix Fatigue crack Initiation in Notched SCS-6/Ti 15-3 Metal Matrix Composites*. NASA TM 104141. NASA Langley Research Center, 1991.
12. Hong, C.S., and Crews Jr, J.H., *Stress Concentration Factors for Finite Orthotropic Laminates with a Circular Hole and Uniaxial Loading*. NASA TP 1469. NASA Langley Research Center, 1979.
13. Hopkins, D.A., and Chamis, C.C., *A Unique Set of Micromechanics Equations for High Temperature Metal Matrix Composites*, NASA TM 87154. NASA Lewis Research Center, 1985.
14. Jen, M.H.R. and Hsu, J.M. "Residual Strength in Notched Composite Materials," *International Journal of Fatigue*, 12:267-274 (July 1990).
15. Johnson, W.S., "Fatigue Testing and Damage Development in Continuous Fiber Reinforced Metal Matrix Composites," *Metal Matrix Composites: Testing, Analysis, and Failure Modes*, ASTM STP 1032, W.S. Johnson, Ed., American Society for Testing and Materials, Philadelphia, 1989, pp 194-221.
16. Johnson, W.S., Lubowinski, S.J., and Highsmith, A.L., "Mechanical Characterization of Unnotched SCS-6/Ti-15-3 Metal Matrix Composites at Room Temperature," *Thermal and Mechanical Behavior of Ceramic and Metal Matrix Composites*, ASTM STP 1080, Kennedy, Moeller, and Johnson, Eds., American Society for Testing and Materials, Philadelphia, 1990.
17. Kantzos, P. and Telesman J., "Fatigue Crack Growth Study of SCS-6/Ti 15-3 Composite," *International Journal of Fatigue*, 12:409-415 (September 1990).
18. Lerch, B.A., Gabb, T.P., and MacKay, R.A., *Heat Treatment Study of the SiC/Ti-15-3 Composite System*. NASA TP 2970. NASA Langley Research Center, 1990.
19. Lerch, B.A., and Saltzman, J.F., *Tensile Deformation of SiC/Ti-15-3 Laminates*. NASA TM 103620. NASA Lewis Research Center, Cleveland OH, 1991.

20. Majumdar, B.S. and Newaz, G.M., "Inelastic Deformation of Metal Matrix Composites: Compression and Fatigue," Submitted for publication. Battelle Memorial Institute, Columbus, Ohio 43201.
21. Mall, S. and Portner, B., "Characterization of Fatigue Behavior in Cross-Ply Laminate of SCS-6/Ti-15-3 Metal Matrix Composite at Elevated Temperature." Submitted for publication in Journal of Engineering Materials and Technology, Air Force Institute of Technology, Wright-Patterson AFB OH, 1991
22. Mall, S. and Schubbe, J.J., "Thermomechanical Fatigue Behavior of a Cross-Ply SCS-6/Ti-15-3 Metal Matrix Composite." Submitted for publication in Journal of Engineering Materials and Technology, Air Force Institute of Technology, Wright-Patterson AFB OH, 1991
23. Mirimadi, M., Johnson, W.S., Bahei-El-Din, Y.A., and Castelli, M.G., *Analysis of Thermomechanical Fatigue of Unidirectional Titanium Metal Matrix Composites*. NASA TM 104105. NASA Langley Research Center, 1991.
24. Naik, R.A. and Johnson, W.S., "Observations of Fatigue Crack Initiation and Damage Growth in Notched Titanium Matrix Composites." Paper presented at the ASTM Third Symposium on Composite Materials: Fatigue and Fracture. Orlando FL, November 6-9, 1989.
25. "NASP Funds Titanium Composite Plant," *Aerospace America*, 30: 66-67 August 1992
26. Newaz, G.M. and Majumdar, B.S., "A Comparison of Mechanical Response of MMC at Room and Elevated Temperatures," Submitted for publication. Battelle Memorial Institute, Columbus, Ohio 43201.
27. Newaz, G.M. and Majumdar, B.S., "Crack Initiation Around Holes in a Unidirectional MMC under Fatigue Loading," Accepted for publication in Engineering Fracture Mechanics. Battelle Memorial Institute, Columbus, Ohio 43201.
28. Pernot, Capt John J. *Crack Growth Rate Modeling of a Titanium-Aluminide Alloy Under Thermal-Mechanical Cycling*. PhD dissertation. School of Engineering, Air Force Institute of Technology (AU), Wright-Patterson AFB OH, December 1991 (AD-A244119).
29. Pollock, W.D., and Johnson, W.S., *Characterization of Unnotched SCS-6/Ti-15-3 Metal Matrix Composites at 650°C*. NASA TM 102699. NASA Langley Research Center, 1990.

30. Portner, Capt Barry D. *Investigation of Fatigue Damage Mechanisms in a Metal Matrix Composite Under Elevated Temperature*. MS Thesis, AFIT/GAE/ENY/90D-20. School of Engineering, Air Force Institute of Technology (AU), Wright-Patterson AFB OH, December 1990 (AD-A230388).
31. Rattray, Capt Jeffrey *Tensile Strength Characterization of a Metal Matrix Composite with Circular Holes*. MS Thesis, AFIT/GAE/ENY/91D-24. School of Engineering, Air Force Institute of Technology (AU), Wright-Patterson AFB OH, December 1990 (AD-A243894).
32. Schubbe, Capt Joel J. *Investigation of Damage Mechanisms in a Cross-Ply Metal Matrix Composite Under Thermo-Mechanical Loading*. MS Thesis, AFIT/GAE/ENY/90D-26. School of Engineering, Air Force Institute of Technology (A U) , Wright-Patterson AFB OH, December 1990 (AD-A230544).
33. Simonds, R.A., *Residual Strength of Five Boron/Aluminum Laminates with Crack-Like Notches After Fatigue Loading*. NASA CR 3815. NASA Langley Research Center, 1984.
34. Smith, K.N., Watson, P., and Topper, T.H., "A Stress-Strain Function for the Fatigue of Metals," *Journal of Materials*, JMLSA, 5: 767-778 (December 1970).
35. Weixing, Yao "On the Notched Strength of Composite Laminates," *Composite Science and Technology*, 45: 105-110 1992.

Vita

Captain Robert P. Baker was born 13 March 1963 in San Diego, California. He graduated from Summerville High School Summerville, South Carolina in 1981. That summer he attended the College of Charleston. Later that year, he transferred to the Ohio State University from which he graduated in 1986 with a Bachelor of Science in Aeronautical and Astronautical Engineering (specialties: astronautics and guidance, control, and flight dynamics). Upon graduation, he received a regular commission and was assigned to Falcon AFB, Colorado where he served as a Satellite Engineering Officer in the Third Satellite Control Squadron. He was involved in maintaining operational capabilities of the Navy's Fleet Satellite Communications (FLTSATCOM) satellites. Additionally, he was in charge of satellite contingency planning and execution. He was selected to serve as a Standardization/Evaluation (DOV) crew evaluator. He then served as a Satellite Operations Crew Commander until he entered the Air Force Institute of Technology School of Engineering in May 1991.

Permanent Address: 12050 Brookston Dr
Cincinnati, Ohio 45240

REPORT NUMBER

1. AGENCY USE ONLY

December 1992

Master's Thesis

4. TITLE AND SUBTITLE

**INVESTIGATION OF FATIGUE BEHAVIOR IN
NOTCHED CROSS-PLY TITANIUM METAL MATRIX
COMPOSITE AT ELEVATED TEMPERATURE**

5. AUTHOR

Robert P. Baker, Captain, USAF

7. PERFORMING ORGANIZATION NAME(S)

Air Force Institute of Technology, WPAFB, OH 45433

AFIT/GAE/ENY/92D-03

9. SPONSORING/MONITORING AGENCY NAME(S)

**Dr. Walter F. Jones
AFOSR/NA
Bolling AFB, DC 20322-6448**

11. SUPPLEMENTARY NOTES

12a. DISTRIBUTION AVAILABILITY STATEMENT

Approved for public release; distribution unlimited

13. ABSTRACT

The objective of this research was to investigate the initiation and progression of damage which develops in notched [0/90]_{2s} SCS-6/Ti-15-3 at elevated temperature. Testing consisted of a monotonic tensile test at 427°C followed by fatigue testing performed under load control with a stress ratio of 0.1 at a frequency of 10 Hz. A crack was defined to have initiated when it had attained a length greater than or equal to 0.124 mm. Crack initiation and progression was monitored by strain and modulus observations and visual inspection via telemicroscope. The cracks were recorded with edge and face replicas. Metallographic and fractographic analysis was performed after specimen failure. Fatigue cracks initiated in the matrix at four locations on the front and back faces of each specimen. Two of these cracks became through-cracks and eventually developed into major cracks which caused the fracture. The applied stress (S) and fatigue lives (N) curves for both initiation and fatigue life were established. Also, crack growth curves as the function of fatigue cycles were established. A detailed metallographic analysis was performed to understand the damage mechanisms and its implication on the observed notched fatigue behavior.

14. SUBJECT TERMS

**Metal Matrix Composite, Elevated Temperature, Fatigue Testing
Titanium, Silicon Carbide Fibers, Damage Initiation, Notched**

167

17. SECURITY CLASSIFICATION
OF REPORT

Unclassified

Unclassified

Unclassified

UL